Three Investigations of Low Mass Stars in the Milky Way Using New Technology Surveys

John C. Lurie

A dissertation
submitted in partial fulfillment of the
requirements for the degree of

Doctor of Philosophy

University of Washington

2018

Reading Committee:

Mario Jurić, Chair

Kevin Covey

Suzanne Hawley

Program Authorized to Offer Degree:
Astronomy

University of Washington

Abstract

Three Investigations of Low Mass Stars in the Milky Way Using New Technology Surveys

John C. Lurie

Chair of the Supervisory Committee:
Associate Professor Mario Jurić
Astronomy

At least 80% of stars in the Milky Way have masses less than or equal to the Sun. These long lived stars are the most likely hosts of planets where complex life can develop. Although relatively stable on the timescale of billions of years, many low mass stars possess strong magnetic fields that are manifested in energetic surface activity, which may pose a hazard to both life and technology. Magnetic activity also influences the evolution of a low mass star through a feedback process that slows the rotation rate, which in turn tends to decrease the amount of activity. In this way, the rotation rate and activity level of a low mass star may provide an estimate of its age. Beyond their rotation-activity evolution as isolated objects, a small but important fraction of low mass stars have a close binary companion that influences the rotational and orbital properties of the system. Binary interaction can lead to phenomena such as supernovae, cataclysmic variables, and degenerate object mergers. From a larger perspective, low mass stars trace Galactic structure, and through their longevity serve as archives of the dynamical and chemical history of the Milky Way.

Thus a full picture of low mass stars, and by extension the Milky Way, requires understanding their rotation and activity; their interaction in close binaries; and their spatial and kinematic distribution throughout the Galaxy. Historically, these topics have been approached from two separate but complementary modes of observation. Time series photometric surveys measure the stellar variability caused by rotation, activity, and binary interaction,

while wide field surveys measure the brightnesses and colors of millions of stars to map their distribution in the Galaxy. The first generation of digital detectors and computing technology limited intensive time series surveys to a small number of stars, and limited wide field surveys to little if any variability information. Today those limitations are falling away.

This thesis is composed of three investigations of low mass stars using two recent surveys at the cutting edge of detector technology. The *Kepler* space telescope carried the largest camera ever launched into space, and continuously monitored the brightnesses of hundreds of thousands of stars with unprecedented precision and cadence. The Pan-STARRS survey was equipped with the largest camera ever constructed, and imaged 75% percent of the sky to greater depth than any previous optical survey.

The first investigation in this thesis used *Kepler* observations of a binary system containing two stars that are about one third the mass of the Sun. The convective motions in these stars extend to their centers, and so there is no interface with a radiative core to drive a solar-like dynamo that powers the magnetic activity of stars like the Sun. By virtue of being in a binary, the stars have the same age, providing a control for the interdependent effects of activity and rotation. The investigation found that the stars have nearly the same level of activity, despite one star rotating almost three times faster than the other. This suggests that in fully convective stars, there is a threshold rotation rate above which activity is no longer correlated with rotation.

The second investigation also used *Kepler* observations, but in this case focused on low mass stars in close binaries, where tidal interactions are expected to circularize the orbit and synchronize the rotation rates to the orbital period. Prior to this investigation, there were few observational constraints on the tidal synchronization of stars with convective envelopes, and this investigation resulted in rotation period measurements for over 800 such stars. At orbital periods below approximately ten days, nearly all binaries are synchronized, while beyond ten days most binaries have eccentric orbits and rotation rates that are synchronized to the angular velocity at periastron. An unexpected result was that 15% of binaries with orbital periods below ten days are rotating about 13% slower than the synchronized rate. It was suggested that the equators of the stars are in fact synchronized, and that the subsynchronous signal originates from slower rotating high latitudes. The subsynchronous population presents a new test for theories of activity and differential rotation in tidally interacting binaries.

The final investigation used Pan-STARRS observations to search for asymmetries in the disk of the Milky Way. In this case, low mass stars served as tracers of Galactic structure. Previous deep optical surveys avoided the Galactic plane, but Pan-STARRS enabled a comprehensive search. In particular, asymmetries in the stellar density distribution may be the result of interactions with satellite galaxies, and the frequency and nature of the interactions provide an observational test case for theories of galaxy formation. The investigation revealed four asymmetries that extend over much of the visible disk. The observations are qualitatively consistent with mock observations of a Milky Way-like galaxy with a radial wave in its midplane. Although the origin of these asymmetries continues to be debated, the results support a new view of the Milky Way disk that is asymmetric at the 10-30% level in terms of the mean number of star counts.

As a whole, the three investigations in this thesis bring together two different observational approaches to take a holistic view of low mass stars in the Milky Way. In the near future, new surveys will provide even higher quality data for billions of stars. Therefore, it will be more important than ever to understand low mass stars both as complex astrophysical objects and as a major constituent of the Galaxy.

TABLE OF CONTENTS

LIST OF FIGURES

LIST OF TABLES

Table Number Page

ACKNOWLEDGMENTS

I am deeply grateful to the many people who supported, guided, and comforted me on this journey, and without whom this thesis would not exist. My parents provided reassurance at every turn, and my sister reminded me not to take things so seriously. My extended family is an endless source of good humor and inspiration, especially my centenarian great uncle Paul with his gentle injunction to “get it done!” Honorary aunt Margaret Mills prepared hand-caught crab during summer retreats to her island home.

My advisors, Suzanne Hawley and Mario Jurić have been generous, patient, and an absolute pleasure to work with. My committee members, Rory Barnes and Kevin Covey have provided valuable insights. The GSRs for my General and Final Exams, Charlie Eriksen and Geoff Boynton, generously offered their time. The faculty of the UW Astronomy Department have taught so much to an occasionally flippant pupil. I wouldn’t be here without the GSU Physics and Astronomy Department, especially Todd Henry and the RECONS team.

The UW astronomy graduate students have been like my second family, and shared many cathartic karaoke songs and foosball games. Jim Davenport is my role model as a scientist, citizen, and father.

The enthusiasm of the UW astronomy undergraduates reminds me why I took up astronomy. It was my great privilege to work with Karl Vyhmeister, Andrea Chen, Michael Puig-Holzman, and Jamel Adilia, as well as five teams of Astronomy 481 students at MRO, a scientific sanctuary with a much treasured collection of vinyl records.

Last but not least my cats Beethoven, Haydn, and Mozart have patiently awaited my return (or so I like to imagine) under the caring eyes of my parents.

DEDICATION

For my family.

Chapter 1

INTRODUCTION

1.1 Low Mass Stars in the Milky Way

This thesis is an observation-based investigation of how stars behave and how they are distributed in our Galaxy[1]. In particular, it is focused on low mass stars that are on the main sequence, meaning that they fuse hydrogen into helium in their cores. This section describes the important role that low mass stars play in the Galaxy.

Mass is the most fundamental property of a star, and to first order determines its evolution. The lowest mass stars are approximately 8% the mass of the Sun ($M_\odot$). Objects below this mass can't fuse hydrogen in their cores, and are known as brown dwarfs. The highest mass stars are about 100 $M_\odot$. Above this mass, the energy produced by fusion is so great that stars can no longer be held together by gravity.

High and low mass stars play very different roles in the Galaxy, due to the lifetimes of stars, and to the initial mass function (IMF) which determines the distribution of stellar masses in the Galaxy. The top panel of Figure 1.1 plots the main sequence lifetimes of stars as a function of mass, using a simple approximation, which assumes that the luminosity across the entire main sequence goes as $L \propto M^{3.5}$. It further assumes that the main sequence lifetime of the Sun is 10 billion years, and that stars of all masses fuse the same fraction of their mass on the main sequence as the Sun. In fact, the mass-luminosity relation has a shallower slope at both the low and high mass ends, so that Figure 1.1 underestimates the lifetimes at either end. However, the conclusion is unchanged that the main sequence lifetime varies by over six orders of magnitude across the main sequence. The highest mass

---

[1] I follow the convention of referring to the Milky Way Galaxy with a capital G, to distinguish it from galaxies in general.

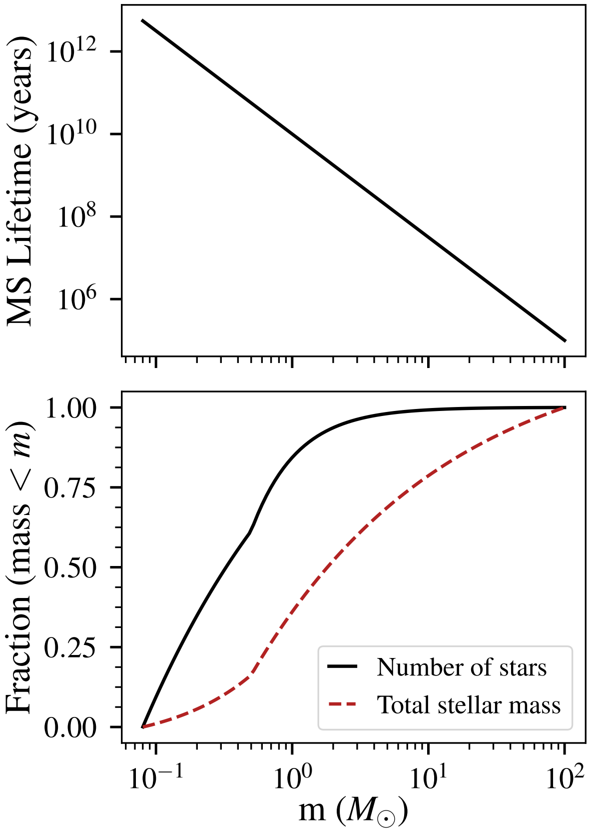

Figure 1.1: Top: Approximate main sequence lifetimes. Bottom: Number of stars (black line), and total stellar mass fractions (dashed red line) as a function of mass, based on the Kroupa (2001) IMF.

stars are only on the main sequence for a few hundred thousand years, compared to trillions of years for the lowest mass stars, much longer than the age of the Universe.

The classical IMF of Salpeter (1955) states that the number of stars per unit mass declines as $M^{-2.35}$, meaning that star formation produces many more low mass stars than high mass stars. There is general agreement that the slope of the IMF above 1 $M_\odot$ is close to the Salpeter value. More recent studies have found a turnover at lower masses. Kroupa (2001) modeled this as breaks in the power law at 0.5 and 0.08 $M_\odot$(for brown dwarfs), while

Chabrier (2003) models a log-normal distribution below 1 $M_\odot$. There is much research on whether and how the IMF varies in different conditions and at different times in the history of the Universe. This thesis is not concerned with variations in the shape of the IMF, only that the IMF produces many more low mass stars than high mass stars.

The abundance of low mass stars is visualized in the bottom panel of Figure 1.1. The black curve plots the fraction of stars below a given mass. Based on the Kroupa IMF integrated to 100 $M_\odot$, 84% of stars have masses less than 1 $M_\odot$, and 98% have masses less than 5 $M_\odot$. Although they are numerous, only 36% of the total mass produced by star formation goes into stars below 1 $M_\odot$, while 21% of the mass goes into stars above $10 M_\odot$.

The role of high mass stars is to dominate the star-gas-star cycle. Stars will eventually return some or all of their material to the interstellar medium, which will in turn produce more stars. The elements produced by fusion in high mass stars are the building blocks for terrestrial planets and life. High mass stars are very efficient at returning their material through strong winds and supernova explosions. Furthermore, their short lifetimes mean that they participate in many more rounds of chemical enrichment compared to low mass stars. High mass stars can disrupt star formation through their ionizing radiation, winds, and supernovae, although supernovae shocks can also trigger star formation.

In contrast, low mass stars play the role of "sinks" in the cycle. Once mass goes into a low mass star, it isn't returned for billions or even trillions of years. The abundance and long lifetimes of low mass stars mean that they provide the habitable real estate of the Galaxy[2].

In this thesis, low mass stars are defined as those below 1.3 $M_\odot$. This division is based on internal processes and structure, but it conveniently divides the stellar mass produced by the IMF roughly in half: 42% of the mass lies in stars below 1.3 $M_\odot$ compared to 58% in stars above 1.3 $M_\odot$. Given that the number of low mass stars has built up over the history of the Galaxy, the present day mass fraction is closer to 50% in each component.

Below 1.3 $M_\odot$, the dominant hydrogen fusion process is a set of reactions known as the

---

[2] Credit is due to Tiffany Clements for this excellent analogy.

proton-proton chain, while above this mass the dominant process is known as the CNO cycle, because it uses carbon, nitrogen, and oxygen as catalysts to produce helium (Arnett, 1996). The CNO cycle has a much stronger temperature dependence (T^{16}, Prialnik 2000) than the proton-proton chain (T^4), so it fuses hydrogen faster, resulting in the short lifetimes of high mass stars. The strong temperature dependence also means that in the cores of massive stars undergoing CNO fusion, there is a strong outward energy gradient. The gradient is too steep for radiative energy transport, so the cores are convective, while the outer layers transport energy by radiation. In low mass stars, the core is radiative until the neutral hydrogen opacity becomes too high in the outer layers, which are convective. Below about 0.3 $M_\odot$, the entire star is convective (Chabrier, 2003).

For isolated low mass stars, magnetic activity is an essential process to understand, because otherwise they change very little over their main sequence lifetimes. Magnetic activity in the form of flares and coronal mass ejections (CMEs) produces X-ray and particle radiation that can impact life and climate on planets. Mass loss from these events, amplified by the magnetic field, can slow the star's rotation in a process known as magnetic braking. The rotation rate itself can be measured from brightness variations caused by starspots, another manifestation of the magnetic field. Models of magnetic braking processes and measurements of rotation rates can be combined to estimate stellar ages. Known as gyrochronology, this technique is particularly important for low mass stars, whose ages are often poorly constrained.

Another important aspect of understanding low mass star evolution is whether the star has a close binary companion. If the star does not have a companion, or if the companion is sufficiently far away, then its evolution is determined solely by intrinsic properties. A close companion can influence the star's evolution, but how it does so depends on the separation between the stars. In the most extreme cases, the stars will be in contact, and capable of exchanging mass and energy, such that the structure of the stars may be different than isolated stars of the same mass (Eggleton, 2006). At slightly larger separations, tidal effects remain very strong. Tides will tend to make the orbit circular, and to lock the rotation period to the orbital period, for the same reason that the Moon always keeps the same face towards the Earth. As the stars evolve off the main sequence, mass transfer can result in phenomena that include cataclysmic variables, supernovae, and mergers.

Beyond their evolution as isolated stars or interacting binaries, low mass stars are tracers of the structure of the Galaxy. Due to their abundance, the distribution of low mass stars is synonymous with Galactic structure. Due to their longevity, low mass stars hold clues about the formation and history of the Galaxy. They are also sufficiently bright to be seen across most of the Galaxy: a $1 M_\odot$ star at a distance of 17 kpc has a visual magnitude of 21, which is easily detectable by the wide field surveys described below.

Thus, the three investigations of this thesis focus on understanding magnetic activity in low mass stars, tidal interaction in close binaries, and using low mass stars to understand Galactic structure. These studies were enabled by new imaging surveys, as described in the next section.

1.2 A New Era in the Observation of Stars

The distances to stars are enormous, so observing them is limited to measuring their positions on the sky and collecting their light with a telescope. There are many methods to process and analyze starlight, but the most efficient way to do so for a large number of stars is simply to take an image.

Imaging surveys can be used to study both the behavior of stars and their spatial distribution. Time domain surveys monitor stellar variability to study astrophysical processes including rotation, magnetic activity, binary interaction, and pulsations. Wide field surveys take images of the entire sky (or at least large portions) to study the distribution of stars across the Galaxy.

The time domain and wide field approaches are complementary. Using stars as tracers of Galactic structure requires understanding their behavior. In particular, the distances to most stars in the Galaxy can only be inferred from their colors using an empirical relation. Because stars evolve over billions of years, much longer than a human lifetime, understanding how their behavior changes over time requires building up a picture from many stars at different stages of their evolution. Wide field surveys also put stellar evolution in the context of the formation history of the Galaxy.

A limitation of imaging surveys is that telescopes have a finite field of view. How continuously stars can be monitored is inversely proportional to the area that can be imaged, and hence the number of stars. Advancements in detector and computer technology have made it possible to image increasingly large areas of sky. This thesis uses two surveys with very large fields of view: *Kepler* and the Panoramic Survey Telescope and Rapid Response System (Pan-STARRS). The surveys were optimized for different purposes: *Kepler* for time domain continuity, and Pan-STARRS for wide field coverage.

This thesis brings together the time domain and wide field approaches, in the form of three case studies. The first two use *Kepler* observations to study rotation, activity, and binary interaction in low mass stars. *Kepler* only observed a small volume of the Milky Way, and so doesn't sample a very diverse population of stars. The third case study takes a much wider view of the Galaxy with Pan-STARRS, using low mass stars to investigate the structure of the Galactic disk, which also provides some clues about its formation.

1.2.1 Kepler : A Groundbreaking Time Domain Survey

Although this thesis uses *Kepler* data to study stars, the mission was conceived and executed as a search for planets around other stars, known as exoplanets. In 1984, Borucki & Summers first outlined the mission that would become *Kepler*. They realized that if exoplanets existed, then some would happen to transit their stars as observed from the Earth. Even if exoplanets were common, transits would be rare, so discovering transiting exoplanets would require a survey to monitor thousands of stars continuously. Borucki, Summers, and their collaborators also realized that such a survey - while designed to discover planets - would be revolutionary for the study of the stars themselves.

However, the technical challenges in constructing the survey were enormous. At the time, detectors were not precise or stable enough to detect transits of Earth-like planets.

Making matters even more complicated, the telescope would need to be in space. Weather and the Earth's rotation prevent continuous observations, and the atmosphere introduces noise that make the small transit signals all but impossible to detect. Borucki spent the next decade and a half helping develop the detector technology and demonstrating that it could be successfully mounted on a space telescope. The *Kepler* mission was selected by NASA in 2001, and launched in 2009.

The spacecraft is in a heliocentric orbit that is 372.5 days long, slightly longer than the Earth's orbit, so that *Kepler* is slowly drifting away from the Earth. Kepler had to keep its solar panels pointed at the Sun, but also keep its telescope pointed at the same part of the sky. To do this, it executed a 90 degree roll every quarter of a *Kepler* year, approximately 90 days. This means that stars fell on four different parts of the focal plane every year. The detector was designed to be symmetric, but differences between quarters make it difficult to study variability on timescales longer than 90 days. That is not important for this thesis, which is focused on variability on timescales of minutes up to tens of days.

The telescope has a 10 × 10 degree field of view. To cover this enormous area required the largest camera ever launched into space. It consisted of 42 separate 2200 × 1024 pixel charge coupled device (CCD) arrays placed together, totaling nearly 95 million pixels. It wasn't possible to send back data from every pixel in every exposure due to bandwidth issues. Instead, *Kepler* only downlinked the pixels immediately surrounding stars of interest, and so could measure at most 170,000 stars at a time. While this is a small number of stars compared to some surveys (see below), the data were unprecedented in their quality.

All targets were observed in low cadence mode, with measurements taken every 30 minutes. These data can be used to study phenomena including stellar rotation, flare rates, and low frequency pulsations. A subset of about 500 stars every quarter were observed in short cadence mode, with measurements taken every minute. These data reveal flaring behavior and energy distributions in great detail, and allow detection of high frequency pulsations and other variability.

Devices known as reaction wheels kept *Kepler* pointed in the correct direction, ensuring that stars remained on the same pixels. This was necessary to achieve high photometric precision. When the second of four wheels failed in 2013, *Kepler* could no longer maintain this level of pointing precision. The spacecraft was then repurposed as the K2 mission, described in Chapter 5.

1.2.2 Pan-STARRS: A Groundbreaking Wide Field Survey

The history of star catalogs dates to ancient times, when they had navigational and time-keeping applications. In the photographic age, one of the most important wide field surveys was the Palomar Observatory Sky Survey conducted in the 1950s. At the time there was no way to measure the brightnesses of all the stars. The photographic plates were later scanned and digitized, and are still important as baselines for proper motion and long term variability studies.

The two most important optical, digital photometric sky surveys prior to Pan-STARRS were the *Hipparcos* space mission launched in 1989, and the Sloan Digital Sky Survey (SDSS), begun in 2000. The primary mission of *Hipparcos* was to measure parallaxes, but it also produced the Tycho photometric catalog that was complete to 11th magnitude in the V filter, containing 2.5 million stars. SDSS went to much fainter magnitudes, but was primarily an extragalactic survey, and largely avoided the Galactic plane. It cataloged more than 200 million stars over 25% of the sky.

Pan-STARRS fills in the gap left by *Hipparcos* and SDSS, because it looked at the Galactic plane to a depth of about 23rd magnitude. The survey operated on a 1.8 meter telescope on Haleakala, Hawaii. At the time of its construction in 2008, it had the largest camera in the world: 1.4 billion pixels, covering a seven square degree field of view.

The general strategy for wide field surveys is to cover as much of the sky as possible in a given night. As the Earth orbits the Sun, new parts of the sky become visible, so over the course of a year the entire sky visible from that site can be imaged. In total, Pan-STARRS surveyed 75% of the sky.

Calibrating the data collected by wide field surveys is a major challenge. In order to map the distribution of stars in the Galaxy, one must be confident that a given magnitude in the catalog corresponds to the same apparent brightness anywhere on the sky. Padmanabhan et al. (2008) developed a technique known as "ubercalibration" for SDSS, which was adapted for Pan-STARRS (Schlafly et al., 2012). Ubercalibration relies on images covering overlapping areas of sky. Requiring that stars in the overlapping area have the same apparent magnitude in all images provides the photometric offsets for each image. Having many stars in the sample cancels out the effects of stellar variability. The calibrated catalog can then be put on an absolute scale by comparison to a small number of standard stars.

It is worth noting that Pan-STARRS was also a time domain survey, and has produced important results in areas such as asteroids and transients. However, the data are of limited use in the study of stellar activity or rotation, because the time sampling was too irregular and infrequent, and the photometric precision too low. Chapter 5 discusses the applications of future ground based, hybrid time domain-wide field surveys, such as the Large Synoptic Survey Telescope (LSST).

1.3 Stellar Rotation and Magnetic Activity

During a low mass star's life, there is a complex feedback process wherein rotation generates a magnetic field, which is manifested by energetic surface phenomena, which in turn drain angular momentum, thereby slowing the star's rotation. As a civilization, it is important to understand solar activity because of its effects on communications satellites, astronaut health, electrical grids, and the Earth's climate. From a broader astrobiological perspective, there is much interest in how stellar activity affects planetary atmospheres and habitability (e.g., Segura et al., 2010; Tilley et al., 2017), particularly as many M dwarfs are highly active and have close-in habitable zones. From a Galactic perspective, an improved understanding of rotation and activity may provide better estimates for the ages of field stars that are otherwise very difficult to determine.

1.3.1 Magnetic Activity on the Sun

Rotation and activity are best understood on the Sun, where fine surface details can be resolved, and accurate historical records extend back over several centuries. The Sun is also a critical anchor for age-rotation-activity relations, because it is a relatively old star (4.6 Gyr), and because its age is known so accurately. Solar activity can be taken as representative of other stars of similar type, but some caution should be taken when extrapolating from a single datapoint.

The Sun rotates differentially, so that the rotation period increases from approximately 26 days at the equator to 36 days at the poles (Beck, 2000). As discussed later in this section, differential rotation is a crucial element in generating the Sun's magnetic field.

Sunspots, flares, and CMEs originate from active regions on the Sun. Active regions are where twisted loops in the Sun's magnetic field lines emerge from and return into the surface, as depicted in the left panel of Figure 1.2. The magnetic field inhibits convection and decreases the density of the photosphere, both of which have the effect of decreasing the temperature. Dark spots, like those in the right panel of Figure 1.2, result because the lower temperature makes the area fainter than the surrounding photosphere. On the Sun, the largest spots have diameters several times that of the Earth, and dissipate within about a month, comparable to one mean solar rotation period.

Flares and CMEs occur when the field lines in coronal loops reconnect (Giovanelli, 1946; Yamada et al., 2010). In coronal loops like those in Figure 1.2, field lines at one end of the loop are directed away from the Sun's surface, while lines at the other end are directed towards the surface. If the loop becomes pinched, field lines directed in opposite directions can connect, and the field is reconfigured. Some of the reconfigured field may form a closed ring that is forced away from the Sun, carrying away material in a CME. The energy released by the reconnection accelerates electrons which hit the lower atmosphere, resulting in X-ray and ultraviolet emission, as well as white light seen by *Kepler*.

Magnetic activity is also manifested by emission lines in the chromosphere and corona of

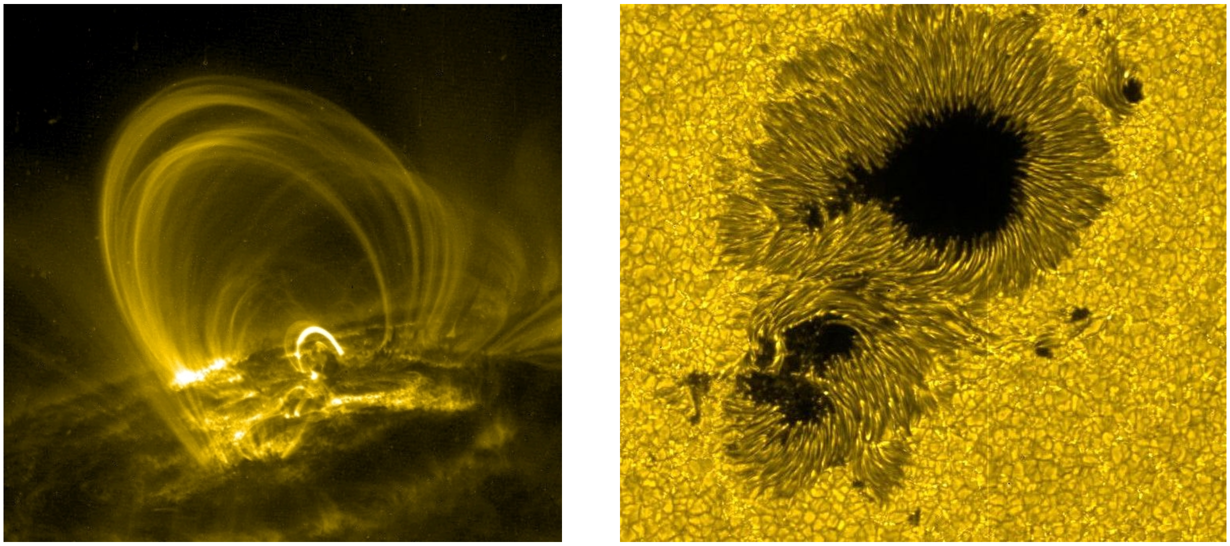

Figure 1.2: Left: Coronal loops emerging from the stellar surface seen in the ultraviolet by the Transition Region and Coronal Explorer. Right: A sunspot group seen in visible light by the Hinode spacecraft. NASA images in the public domain.

the Sun. Of particular importance to astronomers are the Ca II H and K lines. Spatially resolved observations of the Sun demonstrate that Ca II emission is closely correlated with active regions (Skumanich et al., 1975), so that the integrated emission may be taken as a proxy for the overall activity level. Because they are easily observable in the spectra of sun-like stars, the H and K lines are one of the main diagnostics for magnetic activity on other stars (see below).

In the solar activity cycle, the number and latitude distribution of sunspots varies with an approximately eleven year period. At the beginning of the solar cycle, spots are concentrated near latitudes of ±30°. During the cycle, the spots at higher latitudes are replaced by spots closer to the equator. Near the end of the cycle, there are virtually no spots until the cycle repeats and spots begin reappearing at higher latitudes. There are also longer term variations in the total number of spots at solar maximum, including a near total lack of spots between

1645 and 1715 known as the Maunder minimum. As would be expected, fewer spots means fewer active regions, which correlates with fewer flares and CMEs (Goswami et al., 1988).

1.3.2 The Age-Rotation-Activity Relation

It is more difficult to characterize activity on stars other than the Sun, because they are much fainter and typically spatially unresolved, although spatially resolved measurements can be made in some cases. These include interferometry of nearby giants (Parks et al., 2015), Doppler imaging of bright, rapidly rotating stars (Vogt & Penrod, 1983), and occultations of starspots by exoplanets (Silva, 2003; Morris et al., 2017). However for the vast majority of stars, the best means of characterizing rotation and activity are rotation periods, flare rates, and chromospheric emission observed in unresolved light from the star.

Wilson (1963) first noted that the intensity of Ca H and K emission decreases with increasing stellar age, based on a pioneering survey of cluster and field stars. Using these data, Skumanich (1972) found that the rotation rate also decreases with age, and developed the classical age-rotation-activity relation, wherein rotation and activity both decline with the inverse square root of age. It is important to note that Ca II-based age estimates for binary stars can differ by up to 1 Gyr (Donahue, 1998), even though the stars are the same age. These discrepancies are likely due to independent activity cycles on each star, leading to variability in the Ca II measurements.

The mechanism by which stars slow their rotation is known as magnetic braking (Schatzman, 1962). Charged particles in the stellar wind follow the radial (poloidal) magnetic field lines which corotate with the star out to large radii. This increased lever-arm greatly increases the angular momentum loss rate. Even though the Sun has a relatively weak magnetic field and low mass loss rate, magnetic braking amplifies the angular momentum loss by three orders of magnitude compared to the absence of a field (Tassoul, 2000). The rate of magnetic braking depends on both the strength of the magnetic field, and the mass loss rate, with the latter also depending on the magnetic field.

Due to magnetic braking, the age of a low mass star can in principle be determined from its rotation rate, in a technique known as gyrochronology. To be effective, gyrochronology requires calibration against stars of known ages, and further assumes that magnetic braking is a deterministic process, such that stars with identical initial conditions will follow the same rotational evolution.

Barnes (2003, 2007b) conducted a detailed analysis of cluster and field stars, concluding that low mass stars in young clusters are divided into slow and fast rotating populations, and that the fast population converges onto the slow population with increasing age. However, this analysis was based on relatively small samples. With the launch of *Kepler*, it became possible to measure rotation periods for tens of thousands of field stars (e.g. McQuillan et al., 2014). While gyrochronology is promising for younger stars, *Kepler* results suggest that the technique may be problematic for stars with ages comparable to or older than the Sun (Angus et al., 2015), due to changes in magnetic braking as stars age (van Saders et al., 2016).

As with rotation periods, knowledge of flare statistics and behavior was until recently based on intensive ground-based monitoring campaigns. In their seminal work, Lacy et al. (1976) conducted a survey of eight M dwarfs, and found that higher mass M dwarfs flare less frequently but with higher energies than low mass M dwarfs. With the launch of *Kepler*, it became possible to study white light flare morphology in unprecedented detail (Davenport et al., 2014), and to create a flare catalog for over 4000 stars (Davenport, 2016).

Although old low mass stars are generally much less active than their young counterparts, old stars are still capable of generating highly energetic flares. Superflare stars have comparable masses and rotation rates as the Sun, but have produced flares thousands of times more energetic than any known solar flare (Schaefer et al., 2000; Maehara et al., 2012). Given the relatively short timespan of solar records, it is reasonable to assume that the Sun has produced superflares in the past and will do so again in the future. This threat provides perhaps the most pressing case for continued investigation of the age-rotation-activity relation.

1.3.3 Stellar Dynamos

In principle, the Sun's magnetic field could simply be a relic from its formation. However, the existence of the solar activity cycle strongly suggests that the Sun's field is being actively generated and modified (Tobias, 2002). The mechanism that generates the Sun's magnetic field is known as the solar dynamo. By extension, the solar dynamo can be applied to other stars with radiative cores and convective envelopes.

In the simplest terms, the solar dynamo is driven by the rotation of a large mass of conducting fluid. The challenge of dynamo theory is to explain how the magnetic field is maintained, and how the field creates the observed activity on the Sun.

Babcock (1961) and Leighton (1969) introduced a qualitative model to explain the solar cycle. The Sun's magnetic field has both a toroidal and poloidal component. The toroidal component is responsible for active regions, while the poloidal component is important in magnetic braking. Poloidal field lines that are initially orientated north-south will be stretched east-west by differential rotation, eventually converting the poloidal field into a toroidal field. Over time, active regions drift towards the poles and dissipate, so that the toroidal field is converted back into a poloidal field, thus completing the cycle.

At the time of Babcock and Leighton, there was very little data available about the internal structure of the Sun. Decades later, the technique of helioseismology was able to probe the solar interior, analogous to how earthquakes are used to study the Earth's composition. Helioseismology revealed the existence of a thin interface between the Sun's radiative core and convective envelope, known as the tachocline (Spiegel & Zahn, 1992). The tachocline is a crucial element in modern solar dynamo theory, because the strong shear at the interface converts the poloidal field into a toroidal field. The toroidal-to-poloidal conversion may also take place near the tachocline, due to turbulence at the base of the convection zone (Mason et al., 2002).

Fully convective stars have no tachocline, yet clearly have strong magnetic fields and high levels of activity. Magnetic field generation in fully convective stars is an active area of theoretical research (Dobler et al., 2006; Browning, 2008, e.g.). Observations indicate that there is a threshold rotation rate for fully convective stars, above which activity no longer correlates with activity (Delfosse et al., 1998; Mohanty & Basri, 2003; Browning et al., 2010). In that case, the magnetic braking relation for fully convective stars is likely to be different than in stars with solar-type dynamos.

Chapter 2 investigates a wide binary system containing two fully convective stars whose masses are nearly equal, but whose rotation rates differ by almost a factor of three. The system provides a control for age and mass, and so any differences in activity should be due to rotation alone. Furthermore, as a *Kepler* target, the flares and rotationally-induced starspot modulations can be studied in unprecedented detail.

1.4 Binary Interaction

About half of low mass stars are in binary or higher order systems (Duchêne & Kraus, 2013). Binaries are important to astronomy, because they provide measurements of stellar masses and radii, and because their components are the same age. Yet for most binaries, the fact that they have a companion is of little importance to the stars themselves. Table 1.1 categorizes the interaction outcomes at different semimajor axes for a binary containing two 1 $M_{\odot}$ stars, as well the corresponding orbital periods. The details of each category are discussed below, but an important conclusion is that at separations larger than about 1 AU, the stars will not interact at any point in their evolution. This comprises at least 80% of binaries containing low mass stars (Raghavan et al., 2010).

1.4.1 Binaries as Benchmarks

As astrophysical laboratories, binaries provide the most accurate and precise determinations for fundamental stellar parameters including mass, radius, and luminosity. These measurements are inputs for stellar atmosphere and evolution models, which in turn have wide ranging exoplanetary, extragalactic, and cosmological applications. Therefore our understanding of the universe on many scales depends in large part on our understanding of binary stars.

Table 1.1: Interaction of a 1 $M_\odot$+ 1 $M_\odot$ binary

Semimajor Axis (AU)	Orbital Period	Interaction Outcome
< 0.01	6 hours	Contact binary on main sequence (MS)
0.01 - 0.16	6 hours - 16 days	Reaches tidal equilibrium on MS
0.16 - 0.3	16 - 40 days	Reaches pseudosynchronization* on MS
0.3 - 1	40 - 260 days	Tidal interaction post-MS, eventual common envelope
1 - 3×10^4	260 days to 4 Myr	Independent evolution
3×10^4 - 5×10^5	4 Myr to 250 Myr	> 50% disruption probability on MS
$> 5 \times 10^5$	> 250 Myr	Unbound at 8 kpc in disk

Note. — *Pseudosynchronization occurs in eccentric binaries, when the stellar rotation synchronizes to the orbital angular velocity at periastron.

Binaries can be classified based on how they are observed. In an eclipsing binary (EB), the stars periodically pass in front of one another from the point of view of an observer on Earth, causing a decrease in apparent brightness. The primary eclipse is the larger decrease, and occurs when the star with the higher effective temperature is occulted. The secondary eclipse occurs when the cooler star is occulted. The same surface area is occulted in both primary and secondary eclipse, so the hotter star has the greater surface brightness, and hence the larger dip, assuming a circular orbit and an inclination such that both stars are fully occulted.

The time between eclipses provides the orbital period. The effective temperature ratios of the stars can be determined from relative depths of eclipses, while the duration of the eclipse provides the radii of the stars relative to the semimajor axis of the orbit. Determining the radii of the stars in absolute units requires knowing how fast the stars are moving, which requires radial velocities.

In a spectroscopic binary, the spectra of the stars are Doppler shifted due to the orbital motion. In a double lined spectroscopic binary, absorption lines of both stars are detected. This only occurs when the stars have comparable luminosities. More often, only the lines of the more luminous star are detected, resulting in a single line spectroscopic binary.

In a visual binary, both stars are resolved. This favors nearby binaries with large semimajor axes, meaning most orbital periods are a few hundred years or longer, and so complete orbits have yet to be mapped. Using high angular resolution techniques such as interferometry, it is possible to map orbits for binaries with smaller separations and shorter periods.

The categories are not mutually exclusive. An EB can typically be observed as a spectroscopic binary, and in rare cases as a visual binary as well. Double lined spectroscopic eclipsing binaries are the gold standard, because they provide measurements of masses, radii, and temperatures.

1.4.2 Mass Transfer

Whether or not close binaries can exchange mass is determined by the Roche potential (Eggleton, 2006). The Roche potential combines the gravitational attraction of the two stars with the centrifugal acceleration due to the orbital motion. There exists a critical equipotential surface surrounding both stars and intersecting between the stars at the first Lagrange point (L1). The two teardrop-shaped sections of the surface are known as the Roche lobes. Material within each lobe is gravitationally bound to the respective star, while material outside the lobes can be transferred.

Close binaries are typically classified under the scheme of Kopal (1955). In detached binaries, both stars are inside their Roche lobes. The stars may interact via tides or magnetic braking, but no mass transfer takes place. In semi-detached binaries, one star fills its Roche lobe, while the other is inside. Mass transfer is possible from the lobe-filling star to its companion in a process known as Roche lobe overflow. In contact binaries, both stars fill, or overfill, their Roche lobes. Mass and energy can be transferred between both stars (Eggleton, 2006). A contact binary containing two 1 $M_\odot$main sequence stars has an orbital period of about 6 hours.

There is a wide variety of potential outcomes of mass transfer, including dwarf novae (Osaki, 1996), supernovae (Langer, 2012), and possibly degenerate object mergers that produce gravitational radiation (Postnov & Yungelson, 2014). The specific outcome depends on the initial stellar masses, the mass ratio, and the orbital separation. The orbital separation determines the size of the Roche lobes, and the mass determines how quickly the star expands, and whether the envelope is convective or radiative, which determines the rate of mass transfer (Eggleton, 2006). The particular evolutionary stage at which the stars fill their Roche lobes leads in part to the observed diversity of interacting binaries (Kippenhahn & Weigert, 1967; Hilditch, 2001). This thesis will focus on the tidal synchronization of detached binaries, although the above effects must be born in mind.

1.4.3 Tidal Interaction

Tides occur because the gravitational attraction from a companion is not uniform across an extended object, which distorts the object. Unless the binary is in an equilibrium state defined as a circular orbit with coplanar and synchronized rotation, the tidal potential will vary with time. The internal structure of stars cannot respond immediately to the time-varying tidal force, due to dissipation. As a result, the tidal bulges lead or trail the orbiting companion. This lag causes a torque that exchanges angular momentum between the stellar spins and the orbit. Ultimately, the binary will either spiral inward and collide, or reach the equilibrium state described above. The theoretical challenge is to find dissipation mechanisms that provide sufficient tidal torque to explain observations.

In the equilibrium tide model, it is assumed that the tidally distorted star maintains a fixed shape in hydrostatic equilibrium, even though the tidal potential is changing with time. Any forced oscillations (the dynamical tide) are assumed to be rapidly damped and are ignored (Tassoul, 2000). Tidal evolution has historically been discussed in two regimes (Zahn, 1977). In low mass stars with convective envelopes (approximately F-type and later), the equilibrium tide is dissipated by convective turbulence. In high mass stars with radiative envelopes (O-, B-, and A-types), the dynamical tide is dissipated by radiative diffusion.

In the weak friction model for equilibrium tides introduced by George[3] Darwin (1879), there is a lag angle ϕ between the tidal bulge and the orbiting companion.

$$\phi = (\Omega_\star - \omega)\frac{t_{dyn}}{t_{diss}} \tag{1.1}$$

where $\Omega_\star$ and ω are the stellar and instantaneous orbital angular velocities. The dynamical timescale t_{dyn} is the time it takes the star to readjust under hydrostatic equilibrium, and is proportional to the sound speed in the star. The characteristic timescale for dissipation t_{diss} is set by the most efficient dissipation mechanism, which is different in convective and radiative regions, as discussed above. The lag angle will be large if t_{diss} is small compared to t_{dyn}.

---

[3] son of Charles

Using the weak friction model, Hut (1981) calculated analytic solutions to the tidal evolution. The rate of change of the stellar angular velocity $\Omega_\star$ goes as

$$\frac{d\Omega_\star}{dt} \propto \frac{Sq^2}{t_{diss}} \left(\frac{R}{a}\right)^6 \overline{\omega} \left(f_1(e) - \frac{\Omega_\star}{\overline{\omega}}\right) \tag{1.2}$$

where $\overline{\omega}$ is mean orbital angular velocity, q is the stellar mass ratio, a is the orbital semi-major axis, and R is the stellar radius. S is a factor that depends on the structure of the star, and $f_1(e)$ is a lengthy polynomial function of e that has been abbreviated in order to focus on the other terms in the equation. A rapid dissipation of energy (small t_{diss}) leads to a rapid change in $\Omega_\star$.

The change in rotational velocity is also a strong function of a, so only the shortest (perhaps tens of days) period binaries are expected to synchronize over a stellar evolutionary timescale. Additionally, the sign of the derivative depends on the eccentricity and the ratio $\Omega_\star/\overline{\omega}$. Tidal interaction can increase or decrease the amount of asynchronism depending on the physical parameters of the system.

Similarly, rate of change of the eccentricity e goes as

$$\frac{de}{dt} \propto \frac{Sq(1+q)}{t_{diss}} \left(\frac{R}{a}\right)^8 \left(f_2(e) - \frac{\Omega_\star}{\overline{\omega}}\right) \tag{1.3}$$

where $f_2(e)$ is also polynomial function of e. In equation 1.3, the rate of change of e is an even stronger function of a than for $\Omega_\star$. Under this simple approximation, the timescale for circularization will be two orders of magnitude longer than synchronization. Comparing equations 1.2 and 1.3 also highlights that the rates of change of $\Omega_\star$ and e may not have the same sign at any given time. In binaries where the rotation period is much less than the orbital period, the eccentricity will increase even as $\Omega_\star$ decreases (Zahn, 2013).

Hut (1981) divided binaries into four[4] categories based on α, the ratio of orbital to rotational angular momentum at the equilibrium configuration. (1) $\alpha < 3$: The binary cannot reach a stable equilibrium (Hut, 1980). This applies to close orbits with large mass

---

[4] I have added $\alpha < 3$ as an implied fourth category to Hut's original three, and modified the limits on α slightly so that they are continuous and do not overlap.

ratios, e.g. exoplanets. In those cases, the planet may spiral inward. (2) $3 \leq \alpha < 4$: The equilibrium is marginally stable. Circularization and alignment occur relatively quickly, but synchronization takes much longer. (3) $4 \leq \alpha < 10$: Circularization, alignment, and synchronization proceed at roughly the same rate. (4) $\alpha \geq 10$: Alignment occurs relatively quickly, but circularization and synchronization take much longer. Because the orbit remains eccentric, the binary becomes "pseudosynchronized", so that the stars synchronize to the orbital angular velocity at periastron, where the tidal force is the strongest.

Tidal interaction during the pre-main sequence phase must also be considered, because the stars have larger radii and are therefore more susceptible to tidal interaction. In their seminal work, Zahn & Bouchet (1989) found that low mass binaries with orbital periods less than about eight days will circularize during the pre-main sequence phase, while binaries at longer periods will circularize much more slowly during the main sequence phase, up to a maximum period of about 16 days ($a \approx 0.16$ AU) (Latham et al., 2002; Meibom & Mathieu, 2005). Between about 16 and 40 days ($a \approx 0.3$ AU), the binaries may become pseudosynchronized on the main sequence if they are significantly eccentric.

For binaries with semimajor axes between 0.3 and 1 AU, the stars will only interact when they leave the main sequence and their radii increase. Eventually the stars may form a common envelope, leading either to their merger or a cataclysmic variable (Warner, 2003). Beyond about 1 AU, the stars will not interact at any point in their evolution, because this is the maximum radius of a 1 $M_{\odot}$ giant. At much larger separations (3×10^4 AU, Bahcall et al. 1985), there is a greater than 50% probability that the orbit will be disrupted by the Galactic tide and chance stellar encounters during the main sequence lifetime. Beyond 5×10^5 AU, binaries are unbound at the Sun's location in the Galaxy (Jiang & Tremaine, 2010).

Chapter 3 focuses on binaries with periods less 40 days that have undergone significant tidal interaction during the main sequence. The investigation resulted in rotation measurements for over 800 binaries containing low mass stars with convective envelopes. By far the largest such homogeneous sample, it enables an investigation of the dependence of tidal synchronization on orbital period, eccentricity, and stellar mass.

1.5 Galactic Structure and Formation

So far, this introduction has focused on the behavior of isolated stars and the interaction of binary stars. This section considers the collection of stars as a whole, that is the Milky Way. Beyond a star's individual evolution or interaction in a close binary, it is important to consider the Galactic context. For example, long ice age cycles on Earth may be tied to higher cosmic ray fluxes during passages through spiral arms (e.g., Gies & Helsel, 2005), while the Galactic tide and chance stellar encounters may perturb Oort cloud bodies onto Earth-crossing orbits (e.g., Morbidelli, 2005; Fouchard et al., 2006).

In the context of galaxy formation, our Galaxy is unique in that detailed measurements of individual low mass stars can be made over a large volume, providing a wealth of positional, kinematic, and chemical data that is unavailable for other galaxies. The longevity of low mass stars means that the Galaxy contains stars with a wide range of ages. Some are as old as the Galaxy (or perhaps even older), while others are actively forming today. Thus low mass stars serve as an archive of the formation and evolution of the Galaxy.

1.5.1 The Structure of the Milky Way Disk

The Milky Way has three main structural components. The disk contains most of the stars, as well as the gas and dust from which stars are actively forming today. Stars in the disk orbit in nearly circular, coplanar orbits. The Sun is located near the midplane of the disk, approximately 8 kiloparsecs (kpc) from the Galactic center. The central region, known as the bulge, has a spheroidal shape and contains both young and old stars. The halo is a lower density spherical distribution of stars surrounding the disk and bulge. The halo contains the oldest stars in the Galaxy, which have radial orbits, meaning they plunge through the center of the Galaxy. This thesis is concerned primarily with the structure of the disk.

In the most basic approximation, the number density of stars in the disk declines exponentially both with distance from the midplane and distance from the Galactic center. The distance from the Galactic plane (or center) over which the density declines by one factor of

e is known as the scale height (or length).

A more complicated picture of the disk began to emerge when Gilmore & Reid (1983) found that the vertical density beyond 1 kpc from the plane was not well fit by a single exponential profile. They suggested instead that the disk is composed of two superimposed components: a “thin” disk with a scale height of about 300 pc, and a “thick” disk with a scale height of about 1300 pc. In this scenario, most stars near the plane belong to the thin disk, most stars more than a few hundred pc above the plane belong to the thick disk, and most stars beyond a few kpc belong to the halo.

SDSS was a major advancement in the study of Galactic structure, because it had precise and deep photometric coverage over a wide area, whereas previous deep surveys (such as that of Gilmore and Reid) were limited to small areas, and wide area surveys (such as Hipparcos) only probed a small volume. In addition, SDSS collected spectra for hundreds of thousands of stars, providing radial velocities and chemical abundances. Ivezić et al. (2008) developed a method to measure stellar metallicities using near-UV SDSS photometry, and found a clear difference between the high metallicity halo with large rotation velocities and the low metallicity halo with nearly no net rotation. Meanwhile, Jurić et al. (2008) analyzed the vertical density distribution with high precision, confirming that it was not well fit by a single exponential, and revised the thick disk scale height to 900 pc.

On its own, a change in slope of the vertical density profile need not be described by a two component disk. Instead, the density profile could be fit by a more complicated function for a single component. To justify a thin-thick disk decomposition, there must also be an age and/or chemical difference between the components (Binney & Merrifield, 1998). Such differences do exist, and to understand why requires a brief digression into stellar nucleosynthesis.

As a high mass star ($\gtrsim 8\ M_\odot$ for the present discussion) nears the end of its life, the only remaining energy source is the fusion of helium nuclei (alpha particles) with successively heavier nuclei from carbon to oxygen to neon and so on up to iron and nickel. However, fusion beyond nickel requires more energy than it produces, so the star collapses and is destroyed in a Type II supernova (SN II). For stars below 8 $M_{\odot}$, the end product is a white dwarf composed primarily of carbon and oxygen, which will remain inert unless there is mass transfer or a merger with a close binary companion. In the latter case, the white dwarf can explode as a Type Ia supernova (SN Ia), which are thought to produce iron but not alpha elements (Arnett, 1996).

These two mass-dependent supernovae outcomes mean that the relative abundances of heavy elements have changed over the history of the Galaxy. The Big Bang produced effectively only hydrogen and helium (Steigman, 2007). Early in the Galaxy's history, the interstellar medium was enriched by SN II with alpha elements such as magnesium and silicon, as well as iron. Over billions of years, the relative rate of SN Ia to SN II increased as more low mass stars reached the ends of their lives. Thus older stars have little iron overall (parameterized as [Fe/H]), but relatively more alpha elements relative to iron (parameterized as [α/Fe]), In contrast, younger stars have higher [Fe/H], but lower [α/Fe] as Fe from SN Ia has built up at the expense of alpha elements.

Returning to the thin and thick disk, evidence for a decomposition is seen as a bimodality in the [α/Fe] versus [Fe/H] distribution for 17,000 F and G dwarfs measured by Lee et al. (2011). Further analysis of these data by Ivezić et al. (2012) confirmed that [α/H], [Fe/H], and rotational velocities in a 400-600 pc bin can be decomposed into thin and thick disk components using the same weights for all three metrics that are consistent with the density distribution in Jurić et al. (2008). Thick disks are also observed in other galaxies (Yoachim & Dalcanton, 2006), so this phenomenon not unique to the Milky Way.

Some authors have argued that the disk is composed of a continuous distribution of scale heights, rather than only two distinct components (Norris, 1987; Schönrich & Binney, 2009; Bovy et al., 2012). In particular, Bovy et al. (2012) concluded that the underlying [α/H] versus [Fe/H] distribution is smooth, and that the above referenced bimodality occurs because SDSS target selection favored more distant, metal poor stars. It is important to note that this alternative hypothesis does not dispute that the disk of the Milky Way (and other galaxies) has a thick tail, only that the tail is not a separate population from the thin disk. As discussed below, the two-component versus continuous distribution debate implies different causes of disk thickening.

1.5.2 Disk Formation and Substructure

Eggen, Lynden-Bell, & Sandage (ELS, 1962) proposed an early model for the formation of the Milky Way in which the Galaxy began as a collapsing, spherical cloud of gas. The stellar halo formed first, and thus contains the oldest stars with radial orbits and no ordered motion. The cloud was initially rotating very slowly, but the rotation rate increased as the cloud collapsed due to conservation of angular momentum. The disk formed because rotation inhibited the collapse in the direction perpendicular to the rotation axis.

The ELS model provides a useful conceptual picture of the Galaxy's formation, but a more detailed model must also fit within a cosmological context. The existence of dark matter was suggested as early as the 1920s, but Rubin & Ford (1970) and others demonstrated conclusively that galaxies are imbedded in dark matter halos that extend far beyond their stellar halos. Meanwhile, Penzias & Wilson (1965) detected the cosmic microwave background, confirming that the Universe originated in the Big Bang.

Along with these observational advances, White & Rees (1978) presented a model for the Milky Way's formation in an expanding Universe with dark matter. After the Big Bang, initially small overdensities grew into the first dark matter halos. The gas in these halos formed the first stars and became small dwarf galaxies. The Milky Way then formed from the merger of dwarf galaxies, as well as additional infalling gas.

Early evidence for this hierarchical growth process came from Searle & Zinn (1978), who analyzed a sample of globular clusters at large distances from the Galactic center, and found that the metal abundances of the clusters were independent of galactocentric distance. This was interpreted as evidence that the clusters originated from protogalactic fragments, although they could plausibly be explained as fragmentation within the ELS model. Even stronger evidence for the hierarchical growth of the Galaxy comes from the tidal debris of dwarf galaxies, discovered by 2MASS[5] and SDSS (e.g. Majewski et al., 2003; Belokurov et al., 2006; Jurić et al., 2008). A particularly dramatic example is the Sagittarius Stream, which extends in arcs tens of kpc above and below the Galactic plane. The Sagittarius Dwarf Elliptical Galaxy (Ibata et al., 1994) has been identified as the progenitor of the stream (Majewski et al., 2003), demonstrating that the consolidation of galaxies is an ongoing process.

Hierarchical growth may also be responsible for the thick disk. If the thick disk is a distinct population from the thin disk, then hypotheses for its formation favor a single interaction with a satellite. But in that case, it is debated whether the thick disk is composed of tidally stripped stars from a satellite (Abadi et al., 2003), a pre-existing thin disk that was heated by a satellite collison (Quinn et al., 1993; Wyse et al., 2006), or stars that formed in the disk from gas accreted from a satellite (Brook et al., 2004). Alternatively, if the thick disk is the tail of a continuous distribution of components with increasing scale heights, then it is more likely to have formed through internal processes such as radial migration (Schönrich & Binney, 2009).

In addition to having a thickened, metal-poor alpha element-enhanced population, the disk is also asymmetric with respect to its midplane. This was first observed as a large scale warp in the gas disk (Burke, 1957; Kerr et al., 1957; Westerhout, 1957), which was later seen in the stellar component as well (e.g., Djorgovski & Sosin 1989). Near the outer edge of the disk, their are multiple stellar overdensities including the Monoceros Ring (Newberg et al., 2002; Yanny et al., 2003) and the Triangulum Andromeda Cloud (Majewski et al., 2004; Rocha-Pinto et al., 2004). Closer to the Sun's location in the disk, asymmetries have been identified in the stellar density distribution (e.g., Widrow et al. 2012; Yanny & Gardner 2013; Xu et al. 2015), as well as the velocity distribution (Widrow et al., 2012; Carlin et al., 2013; Williams et al., 2013). As in the case of the thick disk, both internal and external origins have been suggested for these disk substructures.

---

[5] Two Micron All-Sky Survey

Ideally, there is a holistic model that can explain the properties of the disk while also remaining consistent with cosmological predictions. Developing such a model has been limited in part by the lack of deep optical photometry of the disk, and so it is unclear if and how different substructures are related. The Pan-STARRS survey provides such coverage, and is the focus of Chapter 4.

1.6 Outline of this Thesis

This introduction has described the critical role that low mass stars play in the Galaxy. Advances in detector and computing technology have enabled imaging surveys to measure the positions and brightness of millions of stars with unprecedented precision. This thesis uses two of those surveys, *Kepler* and Pan-STARRS, in three case studies of stellar rotation and magnetic activity (flares and starspots), binary interaction, and Galactic structure.

Chapter 2 presents an in-depth study of two active, fully convective low mass stars, GJ 1245 A and B. There is much that is unknown about the dynamos in fully convective stars, and how they differ from solar-type dynamos. GJ 1245 AB is a test case for fully convective dynamos, because the stars are in a wide binary and are presumably the same age, and nearly the same mass, but their rotation periods differ by a factor of three. Thus any differences between the activity of the two stars will reveal something about their dynamos. As *Kepler* targets, they can be studied in more detail than other stars.

Chapter 3 also uses *Kepler* to study the rotation of low mass stars in binaries, but in this case the stars in the binary are very close together and their tidal interaction tends to synchronize the stellar rotation periods to the orbital period of the binary. Few previous measurements exist of the tidal synchronization of stars with convective envelopes, and *Kepler* is unique in that it can measure rotation periods for hundreds of such stars with high precision.

Chapter 4 takes a much wider view of the Milky Way, using low mass stars as tracers of Galactic structure. In this case, the variability of the stars is not the focus, but rather their mean colors and brightnesses, which can be used to infer their distances. The recently completed Pan-STARRS survey covered the entire Galactic plane, which no previous deep optical survey had done before. This expanded coverage provides a comprehensive view of asymmetries in the Galactic disk, which is important for understanding the formation history of the Galaxy.

Chapter 2

GJ 1245: A BENCHMARK WIDE BINARY

This chapter is an in-depth investigation of the GJ 1245 system, which as discussed in the Introduction provides a unique benchmark for rotation and activity in fully convective stars. However, GJ 1245 is also a challenging system to study with *Kepler*, because the two stars were not resolved by the standard mission data processing. The first part of this chapter describes the novel technique that was used to generate separate light curves for each star, at which point the analysis of rotation and activity were relatively straightforward.

Material from this chapter was previously published in collaboration with James R. A. Davenport, Suzanne L. Hawley, Tessa D. Wilkinson, John P. Wisniewski, Adam F. Kowalski, and Leslie Hebb in the February 2015 edition of the Astrophysical Journal (Lurie et al., 2015), and has been reproduced here with permission of the American Astronomical Society.

2.1 Introduction

The magnetic fields of M dwarfs manifest themselves in several observable ways. These include flares (e.g, Lacy et al. 1976; Hawley & Pettersen 1991), starspots (e.g., Contadakis 1995; McQuillan et al. 2014), chromospheric Hα emission (e.g., Hawley et al. 1996), and X-ray emission (e.g., Güdel 2004). There has been a longstanding effort to tie such observables to the internal magnetic dynamo, and to disentangle the interdependent effects of stellar mass, age, and rotation rate. In the age-rotation-activity paradigm (e.g., Skumanich 1972), activity depends on rotation rate, which in turn depends on age. Complicating matters, M dwarfs become fully convective at approximately type M4 (Chabrier & Baraffe, 1997), and thus do not have a Solar-like dynamo. While models indicate that activity in fully convective stars depends on rotation rate (Dobler et al., 2006; Browning, 2008), there is observational evidence for a rotation threshold (Delfosse et al., 1998; Mohanty & Basri, 2003; Browning et al., 2010), above which activity no longer correlates with rotation rate.

Because they are coeval, stars in multiple systems provide a control for age, and are test cases for the age-rotation-activity paradigm. Among the nearest (4.5 pc; van Altena et al. 1995) and brightest M dwarfs in the Kepler dataset, the GJ 1245 system is comprised of two active M5 components (A and B), and an M8 companion (C) to A. The spectral types reported here are those in Hawley et al. (2014), hereafter referred to as Paper 1. At ∼3 magnitudes fainter (94% less bright) than component A, component C does not contribute significantly to the total quiescent flux in the Kepler bandpass. Kepler has observed flares on stars as late as L1 (Gizis et al., 2013), and it is possible that a flare on component C could be detected and mistakenly assigned to component A. We discuss the contribution of the C component to our flare sample uncertainties in §2.4. For simplicity, we refer to the properties of the A component individually unless otherwise noted, but the Kepler observations presented here are of the combined flux from the A and C components.

The A and C components are separated by $\sim 0\farcs6$ (2.7 AU) (Dieterich et al., 2012) with an orbital period of ∼15 years (Harrington, 1990), while the AC and B components are separated by $\sim 7''$ (32 AU), with an estimated orbital period of 330 years assuming a circular orbit and a total system mass of 0.3 $M_\odot$ (Harrington, 1990). As discussed in §2.2.3, we see the separation between the photocenters of the AC and B components decrease during the 4 years of Kepler observations in a manner that is consistent with the orbit of the AC system. Due to Kepler's large plate scale of $4''$/pixel, separate light curves for components A and B cannot be generated by aperture photometry. That limitation motivated this work, which aims to generate separate light curves for components A and B from the pixel-level data.

This chapter is the third investigation in a series studying flares with Kepler. Paper 1 examined the stellar activity of 5 early-to-mid type M dwarf systems, including GJ 1245. Paper 1 reported the rotation periods for components A and B of 0.2632 ± 0.0001 and 0.709 ± 0.001 days, respectively, based on light curve modulations due to starspots. We confirm those periods within the uncertainties, which are likely due to the effects of differential rotation discussed in §2.3. Paper 1 also reported a flare sample for the AB system, based on their combined light curve. Davenport et al. (2014), hereafter referred to as Paper 2, focused on the active M dwarf GJ 1243, with a detailed analysis of the temporal morphology of its flares based on a sample of over 6,100 flare events. In this chapter, we analyze the flare properties and starspot evolution of the two stars individually based on their separated light curves.

Containing two nearly identical and fully convective M dwarfs, the GJ 1245 system provides a unique test case to break some of the degeneracies in stellar age-rotation-activity models. Given that stars A and B are coeval and of nearly equal mass, but have rotation periods that differ by almost a factor of 3, we aim to answer several simple yet fundamental questions. Namely, which star flares more often, and how do the energy distributions of their flares differ? We introduce a new metric, L_{fl}/L_{bol}, to compare the energy emitted in flares relative to the bolometric luminosity, and discuss the caveats of this metric in the context of GJ 1245 A and B. As both stars exhibit periodic brightness variations due to starspots, we also aim to determine if their starspot properties differ, and look for evidence of differential rotation. Here we are interested in the bulk activity properties of the two stars, and their dependence on rotation rate.

The outline of the chapter is as follows. In section §2.2 we describe the Kepler data, demonstrate that they contain a clear signal from both components A and B, and describe the process used to generate separate light curves for each component. In §2.3 we compare the nature and evolution of their starspots, and in §2.4 we identify and compare the flares on each component. We conclude in §2.5 by comparing these results to those for GJ 1243, and discuss the results in the broader context of stellar age-rotation-activity models.

2.2 Observations and Analysis

The analysis presented here involves Kepler target pixel files, which contain the raw data transmitted from the spacecraft. A full description of Kepler data processing is given in Fanelli et al. (2011), but we give a brief overview. The Kepler detector consists of 42 CCDs, each of which is divided in half to create 84 output channels. Due to onboard storage and transmission limitations, Kepler was unable to transmit the full image of its field of view with every exposure. Instead, only the pixels immediately surrounding targets, referred to as target pixel masks, or “postage stamps”, were transmitted. A target pixel file contains all of the images of a mask taken during an observing quarter. For each mask, an aperture around the target was chosen. The pixels within this aperture were used in the Kepler Science Operations Center processing to produce the calibrated, detrended Pre-search Data Conditioning - Simple Aperture Photometry (PDC-SAP) light curve (Smith et al., 2012). The PDC-SAP light curves were used for the bulk of the Kepler exoplanet investigations, as well as the stellar activity analyses in Papers 1 and 2. In this section we present our justification for performing our own reduction using PyKE pixel response function (PRF) fitting models, as well as the validation of those models.

2.2.1 Kepler Target Pixel Files

The GJ 1245 system was observed with two different pixel masks. Component A (KIC 008451868) was targeted in long cadence mode (30 minute sampling) during quarters 1 – 17 under Guest Observer programs 10000 and 20028. Component B (KIC 008451881) was targeted in long cadence mode during quarters 0 – 17, and in short cadence mode (1 minute sampling) during quarters 8, 10, and 11 under Guest Observer programs 20016, 20028, 20031, and 30002. Each quarter corresponds to approximately three months of observations, with the exception of quarters 0, 1, and 17, which are shorter. While observed as separate objects, the target pixel files are similar and contain both components within the masks. However, the PDC-SAP light curves are very different because in each case the apertures were chosen to minimize the flux from the other component. The analysis in Paper 1 used the B component data, as the short cadence observations were taken with that mask.

The PDC-SAP light curves exhibit flares and periodic modulation due to starspots. As reported in Figure 4 of Paper 1, a periodogram of the light curve from the B component mask reveals two strong signals at 0.26 and 0.71 days corresponding to the rotation periods of components A and B, respectively. The light curve from the A component pixel mask does not contain any significant signal at the rotation period of the B component, likely because the aperture and data reduction removed most of the B component flux. The PDC-SAP light curve for the B component presents a challenge, as it was taken in the short cadence mode most sensitive to flares, but contains significant signal from star A. Using these data, it is impossible to determine which component is flaring, and to compare the starspot evolution of each component individually.

This limitation motivated us to examine the target pixel files with the hope of generating separate, uncontaminated light curves for each component. We focused our analysis on the B component pixel mask data, as it included short cadence observations that are necessary to detect all but the largest energy flares. The data are stored as FITS files containing the observation time, the raw counts in each pixel, and the calibrated flux in each pixel. While this calibration includes corrections such as bias subtraction and flat fielding, it does not remove systematic instrumental trends, unlike the PDC-SAP processing. The target pixel files also contain information such as the aperture boundaries, the World Coordinate System (WCS) transformations, and the instrument configuration. In the case of GJ 1245, the size of the mask region ranged in size from 7 × 8 pixels to 13 × 11 pixels. The Kepler detector has a large plate scale of $4''$/pixel, undersampling its PSF and producing images that can initially be challenging to interpret. Given the relatively small number of pixels involved, we found it most effective to plot the fluxes contained in each pixel as individual light curves.

An example plot of 1.5 days of Quarter 8 short cadence data is shown in Figure 2.1. The plot contains spatial, temporal, and frequency information. The 11 × 10 grid represents the spatial extent of the pixel mask, with each cell corresponding to one pixel. The field of view is shown by the arrow labeled $44''$ at the top of the plot. Arrows labeled “N” and “E” in the bottom left corner show the on-sky orientation of the mask. Within each pixel, flux is on the y-axis with a range of 2,000 e^{-} s^{-1}, and time is on the x-axis with a range of 2.0 days, as noted in the lower left corner. Only 1.5 days of data are shown for visual clarity. For reference, the boundary of the PDC-SAP aperture is outlined in green. As discussed in §2.2.2, the locations of the PRF model sources for the A and B components are shown as a yellow circle and X, respectively. The expected positions of the stars based on their R.A. and decl. are plotted as a yellow open square and plus symbol, respectively. The R.A. and decl. are obtained from the targets' 2MASS coordinates (Cutri et al., 2003) precessed to epoch J2000.0, taking into account the proper motions in Harrington (1990). The resulting coordinates were converted to pixel locations using the WCS transformations contained in the target pixel files.

The pixel-level data contain two clear periodic signals corresponding to the two rotation periods. Pixels have been colored based on the strength of the signal from each component, i.e., the power of the peaks in the periodogram for that pixel. Red pixels contain a 0.26 day signal from the A component, while blue pixels contain a lower amplitude 0.71 day signal from the B component. Purple pixels in the center contain signal from both components, as evidenced by the beat pattern. White pixels are sky pixels and do not contain a significant signal from either component. During this time period there is a flare on the B component pixels that does not appear on the A component pixels. This plot demonstrates both the wealth of information contained in the target pixel files, and the feasibility of generating separate light curves to recover individual information on starspot modulation and flares for each component.

While the two stellar components are clearly evident in the pixel-level data, they are not separated enough in the images to generate uncontaminated light curves via aperture photometry. We note that the aperture used for the B component PDC-SAP reduction, outlined in green in Figure 2.1, largely excludes pixels of the A component. This was done consistently for all quarters across the entire observation period, thus eliminating a large fraction of the total flux from the system. This explains the observation made in Paper 1 that the PDC-SAP light curve was unexpectedly noisy given the total brightness of the GJ 1245 system. However, as the B component PDC-SAP light curve still contains a significant signal from the A component, it is of limited utility in studying the flare and starspot properties of the B component individually.

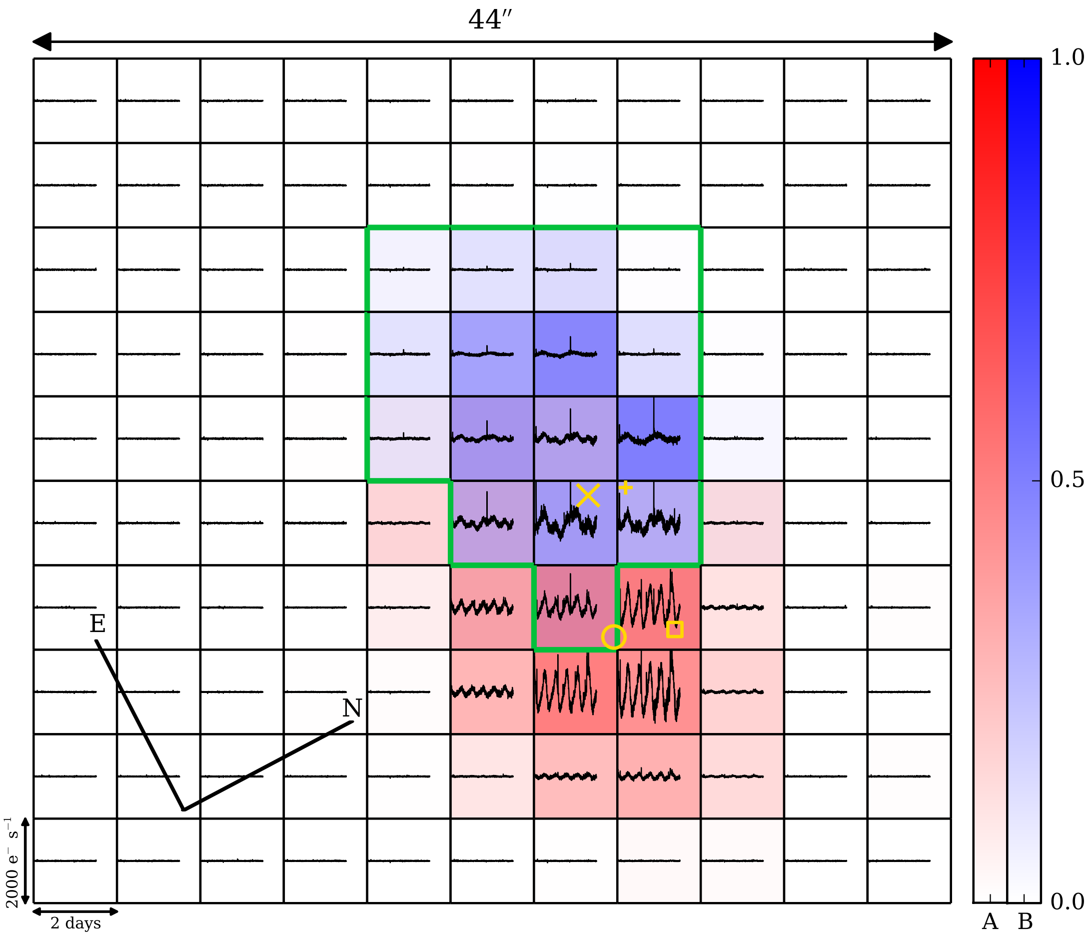

Figure 2.1: The 11 × 10 grid represents the spatial extent of the target pixel mask. The field of view is shown by the 44″ arrow at the top, and the on-sky orientation of the mask is shown by the arrows labeled "E" and "N". Within each cell, the pixel-level light curve is plotted. The y-axis range in each pixel is 2000 e^{-} s^{-1}, and the timespan is 2 days, as denoted in the lower left corner. The color of each pixel corresponds to the strength of the starspot signals in each pixel, indicated by the color bars on the right. The locations of the PRF model sources for the A and B components are shown as a yellow circle and X, respectively. The expected positions of the stars based on their R.A. and decl. are plotted as a yellow open square and plus symbol, respectively.

2.2.2 PRF Model Light Curves with PyKE

To generate separate light curves for each component, we used the *kepprf* and *kepprfphot* routines in the PyKE software package (Still & Barclay, 2012). Full documentation of PyKE is available on the Kepler Guest Observer website[1]. The *kepprf* routine fits one or more sources to a target pixel image, using a PRF model derived during spacecraft commissioning. The *kepprfphot* routine performs the same functions as *kepprf*, but generates light curves by fitting the observations within a given time window, or an entire quarter. Here we make a distinction between the point spread function (PSF), which is how light falls onto the detector, and the PRF, which is how the detector sees the PSF. The PRF can differ from the PSF due to pointing jitter during an exposure and systematics within the detector.

The Kepler PRF model was derived during spacecraft commissioning by observing approximately 19,000 calibration stars in a dither pattern (Bryson et al., 2010). This dithering allowed the PRF to be sampled at the sub-pixel level. The PRF model was then computed as a polynomial fit to the dithered observations. The publicly available PRF model used by PyKE is in the form of a lookup table. For each CCD output channel, there are five PRF models, one defined at each corner and one in the center. The PyKE routines linearly interpolate between the five PRF models to generate a single model used for the fit. The model is defined on a 50×50 grid within each pixel. Given three user-specified free parameters for the sources: flux and the column and row positions on the detector, the routines use the PRF model to compute the total flux within the mask that would result from sources with the given locations and fluxes. They then find the parameters that minimize the residual flux across the pixel mask.

As the locations of the components on the detector vary from quarter to quarter due to spacecraft roll and pointing changes, we first ran *kepprf* to determine their initial locations at the start of each quarter. Knowing the on-sky separation of the two components, and using the rotation period information seen in Figure 2.1, we were able to make a reasonable

---

[1] *keplergo.arc.nasa.gov/PyKE.shtml*

guess of the source locations. As stated in the PyKE documentation, the model convergence is not very dependent on the initial guesses for location, as long as they are within one pixel of the true position. Because the components are of roughly equal luminosity, we set the initial fluxes to equal. Convergence of the model is also not very dependent on the initial flux values.

A typical output of the *kepprf* routine is shown in Figure 2.2. The top left panel shows an image from the same quarter and pixel mask as Figure 2.1. Unlike Figure 2.1, the greyscale color bar signifies the flux for a single exposure. The top right panel shows the PRF model with sources at the A and B component locations. The locations of the A and B components in the model are shown as the yellow circle and X, respectively, in Figure 2.1. The model flux is defined on a 50 × 50 sub-pixel grid, which must be summed within each pixel to generate the pixel-level fluxes labeled "Fit" in the lower left panel. The residuals between the observation and the fit are shown the lower right panel. Note that the color bar for this residual panel contains both negative and positive values, and has a factor of 10 smaller range in order to show the residuals in greater contrast. We analyze the residuals and validate the PRF model in §2.2.3.

In our reduction, we chose to include exposures flagged with quality issues, as described in the Kepler Archive Manual (Thompson & Fraquelli, 2014). Generally representing $\lesssim 10\%$ of the data in a given quarter, some of these flagged observations are not in fact exposures, but instead placeholders for when the spacecraft was in safe mode, and thus contain no data. In this case *kepprfphot* does not attempt a fit. Some exposures were flagged as containing a cosmic ray. If a genuine cosmic ray were detected, it would be limited to a single exposure and therefore not identified as a flare by the procedure described in §2.4. It is also possible that a genuine flare event could be mistaken for an anomaly and removed in the calibration of the target pixel files, but the data flags indicate this is not the case for the short cadence data used for the flare analysis in §2.4.

The majority of the remaining flagged exposures were taken during events that have the potential to degrade the photometric precision, such as thermal equilibration after a

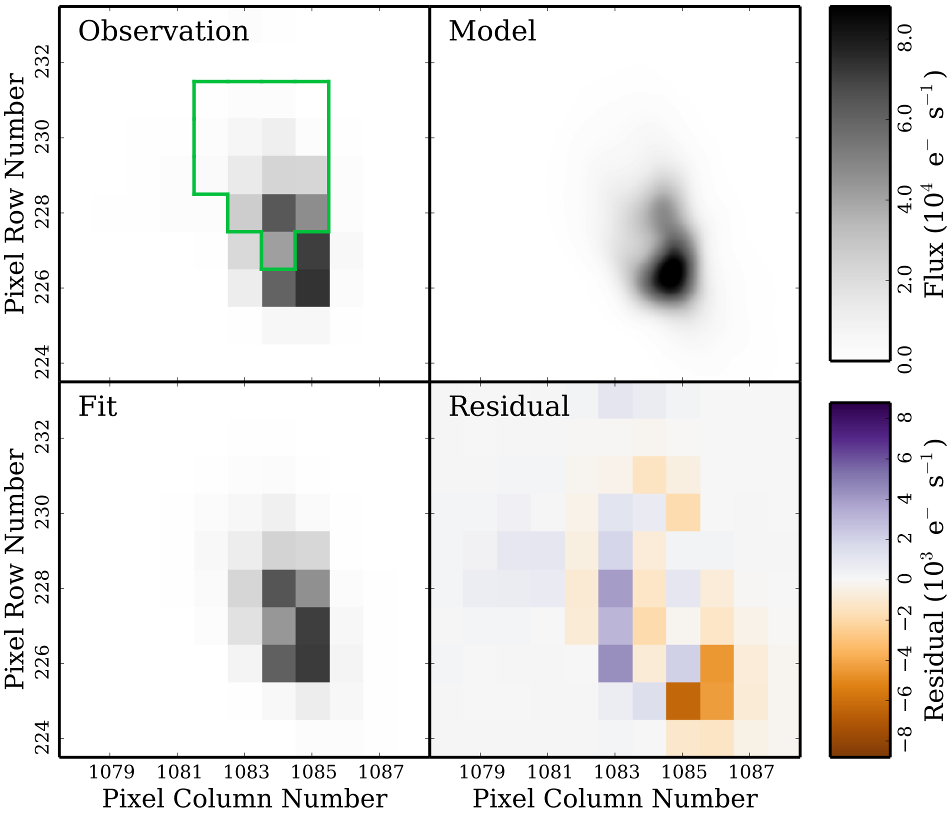

Figure 2.2: The top left panel corresponds to a single observation of the target pixel mask, with the flux in each pixel indicated by the greyscale colorbar. The green border demarcates the PDC-SAP aperture. The PyKE PRF model is in the top right panel, which is summed within each pixel to produce the fit in the lower left panel. The lower right panel shows the residual between the observation and fit. Note that the residual color bar has both negative and positive values, and has a factor of 10 smaller range than the other panels.

spacecraft Earth pointing, or scattered light falling onto the mask. These flagged exposures were generally included in the PDC-SAP reduction, and we chose to include them in our reduction as well. The model fits to the flagged exposures are consistent with the unflagged exposures, although at times they appear noisier. We concluded that the risk of degraded photometric precision is outweighed by the benefit of increased time sampling when searching for flares. The effect that this noise source (and others) have on our ability to detect low amplitude flares is discussed in §2.4.

We ran *kepprfphot* to generate separate light curves for all 18 quarters of long cadence data and all 3 quarters of short cadence data taken with the B component pixel mask. The calibrated fluxes in the target pixel files are already background subtracted, so as recommended in the documentation, we did not include a background source. Nor did we include parameters for pixel scale variation and focus rotation, in keeping with the documentation's recommendation. Conservatively, we set the convergence tolerances for the residual minimization to 10^{-7}. Smaller values correspond to a smaller error tolerance. We saw no change in the model output below 10^{-6}, so further decreasing the tolerance would not have changed the results. The separated light curves produced by *kepprfphot* represent the source fluxes from the best-fit models to each exposure. With the separated light curves, we are able to analyze the flare and starspot properties of each star individually. However before proceeding to do so, we next validate our model light curves to ensure that we have correctly deconvolved the two components.

2.2.3 Model Validation

To validate our PRF models, we compare our results to several well-constrained astrophysical properties of the GJ 1245 system. These include the on-sky location and angular separation of the stars, their rotation periods, and their flux ratio.

Astrometry

The positions of the A and B components in the model for Quarter 8 are plotted in Figure 2.1 as a yellow circle and X, respectively. These positions correlate well with the strength of the starspot signals shown by the red and blue color bars. The expected R.A. and decl. of the A and B components have been transformed into detector coordinates using the WCS data contained in the pixel file header, and are plotted in Figure 2.1 as a yellow plus and unfilled square, respectively. The predicted locations agree well with the models, and differ by less than a pixel, below the level at which the model convergence is dependent. The small discrepancy could be due to a combination of uncertainties in spacecraft pointing, the WCS transformations, the 2MASS coordinates and proper motions used to calculate the R.A. and decl., as well as uncertainties in the PRF model.

Computing the angular separation of components A and B as function of time over the four years of observations provides both a means to verify our models, and a test of Kepler's astrometric capabilities. The mean angular separation during the four years is 6.7±0.″2, consistent with the value of 6.″96 in Dieterich et al. (2012). We find that the measured separation can vary significantly within a quarter, by up to a few tenths of an arcsecond. These intra-quarter variations repeat on an annual cycle, likely due to the stars being on different parts of the focal plane as the spacecraft executed four seasonal rolls to keep its solar panels pointed towards the Sun. This suggests that the intra-quarter variations are due to systematic effects within the spacecraft optics and detector, such as differential velocity aberration or intra-pixel sensitivity variations (Christiansen et al., 2013). It is also possible that the true PRF evolved as a function of time, and therefore differed from the model derived during commissioning. The PyKE PRF models can include parameters for pixel scale changes and PRF rotation in the fit. A test reduction including these parameters did not improve the fit and caused no change in the separation trends. The PyKE documentation does not recommend including these parameters, and we did not include them in our reductions.

In addition to the intra-quarter variations, we observe a long term trend of decreasing separation between components A and B, indicative of a shift in the AC photocenter caused by the unseen C component. Plotted in Figure 2.3 is the angular separation of components A and B in each quarter of Kepler data, as determined by our PRF models. The vertical lines represent the range of values within each quarter due to the intra-quarter variations discussed above. Data points have been color-coded based on the observing season, i.e., spacecraft orientation, in which they were taken. Quarter 0 was a commissioning period that does not correspond to the seasons of the other quarters, so it is plotted in black. In unresolved images like the Kepler observations, a binary orbit such as GJ 1245AC would be observed as the photocenter of the two stars orbiting their center of mass. Harrington (1990) measured a photocentric perturbation for GJ 1245AC of $0\farcs28$ with a period of 15.2 years. Given its expected amplitude and period, it should be detectable in the Kepler data.

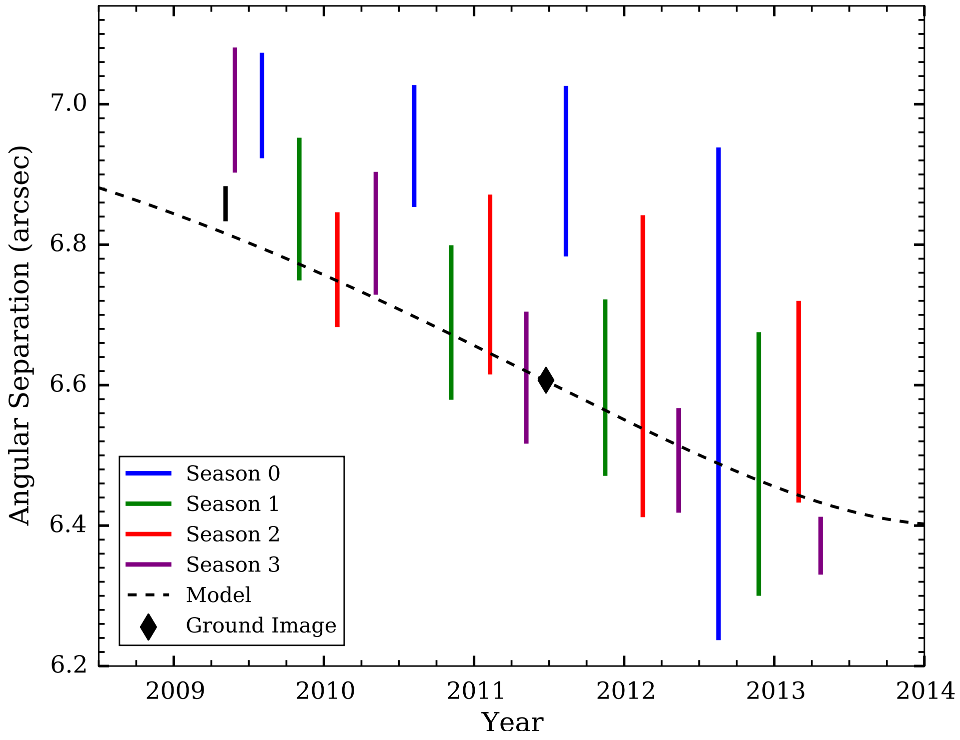

Figure 2.3: The ranges of angular separation in each Kepler quarter are plotted as vertical lines. Quarters are color-coded based on the observing season (spacecraft orientation) during which they were taken. The dashed line corresponds to the expected angular separation based on orbital parameters derived from HST FGS observations. The model is constrained to pass through the ground-based data point, shown as a black diamond. Quarter 0 does not correspond to the seasonal cycle, and is plotted in black. Quarter 17 (rightmost purple line) is only 30 days long, and therefore has a smaller variation.

Modeling the expected angular separation as a function of time requires knowing both accurate orbital parameters of the AC system, and a recent measurement of the separation between the AC and B components. The HST Fine Guidance Sensor (FGS) observations of GJ 1245 A and C described in Henry et al. (1999) were made as part of a long term astrometric program, and have yielded updated orbital parameters (Benedict et al. in prep.). The NOAO Science Archive contains a 2011 V filter observation of GJ 1245 taken with the WIYN 0.9m mosaic imager. We determined the angular separation of the AC and B components in this image by measuring the centroids with the IRAF *imexam* tool, and then converting their detector positions to R.A. and decl. using WCS transformations. The resulting angular separation is 6″.6 at position angle (PA) 77 degrees east of north. For comparison, the separation was 6″.96 at PA 83 degrees in 1998 (Dieterich et al., 2012), and 7″.97 at PA 98 degrees in 1975 (Harrington, 1990), evidence of the several hundred year orbital motion of the AC and B components around their center of mass.

Using the AC orbital parameters derived from the FGS observations, along with the AC to B component separation measured in the 2011 ground-based image, we model the expected angular separation in Figure 2.3. The model is constrained so that it must pass through the ground-based data point. The slope and amplitude of the model is consistent with the observations. The Season 0 data points have the largest scatter, and if they are disregarded the model agrees well with the data, given the fairly large intra-quarter variations. We did not attempt to correct for these variations, so a more detailed analysis and comparison to the much more precise HST observations is beyond the scope of this thesis. However, these results serve to validate our PRF models, given their agreement with the contemporaneous ground-based image, and that the long term trend is consistent with an astrometric perturbation due to the C component.

Rotation Periods

An example of the short cadence separated light curves produced by *kepprfphot* is shown in Figure 2.4. By eye, it is easy to see the two starspot signals, as well as flares that occur on one component but not the other. Lomb-Scargle periodograms of the 4 year, detrended, long cadence light curves discussed in §2.3 are shown in Figure 2.5. In the A component periodogram, there is a large peak at the 0.26 day rotation period of the A component, as well as at 1/2 of the A period. In the B component periodogram, there is a large peak at the 0.71 day rotation period of the B component, and at 1/2 of the B rotation period. There is also a small peak at the A component period. These periodograms indicate that the PRF models have cleanly deconvolved the two components with minimal cross-contamination.

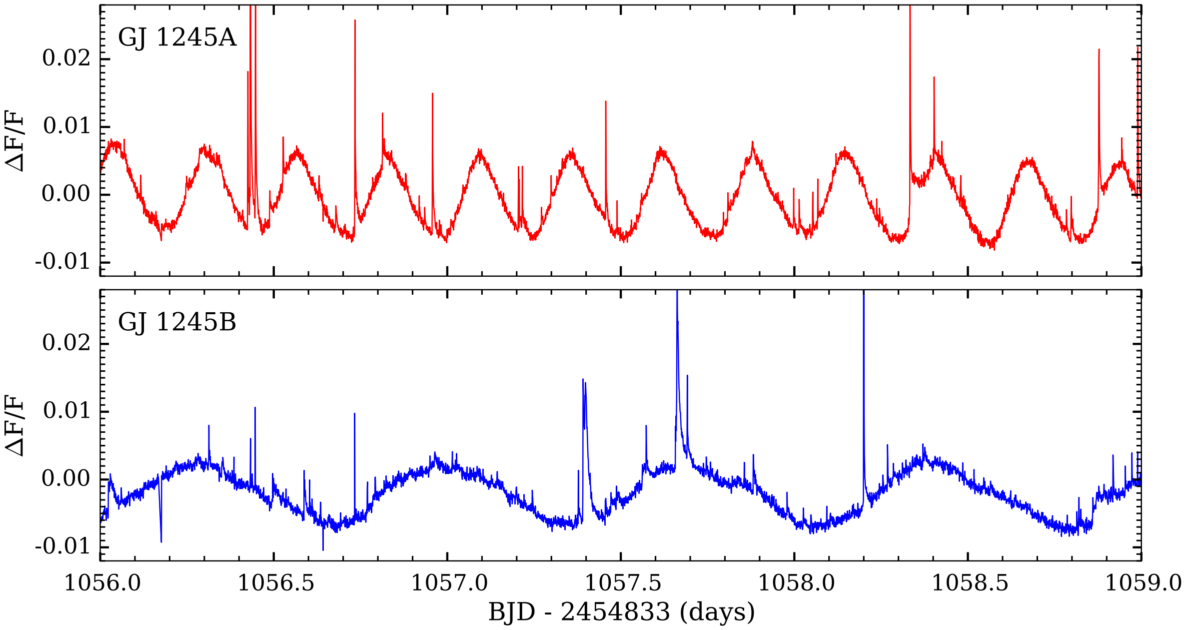

Figure 2.4: An example of the separated, short cadence light curves generated by the *kepprfphot* routine, in terms of relative flux. Nearly all of the flares shown are separate events occurring on only one star. The negative flux excursions are single-exposure errors in the models.

Flux Ratios

The PRF models consistently converge to a flux for the A component that is on average 2.9 times that of component B, and varies between quarters from 2.5 to 3.3. From the published photometry, the flux ratio of the A component to the B component is 1.84, 1.74, 1.64, and

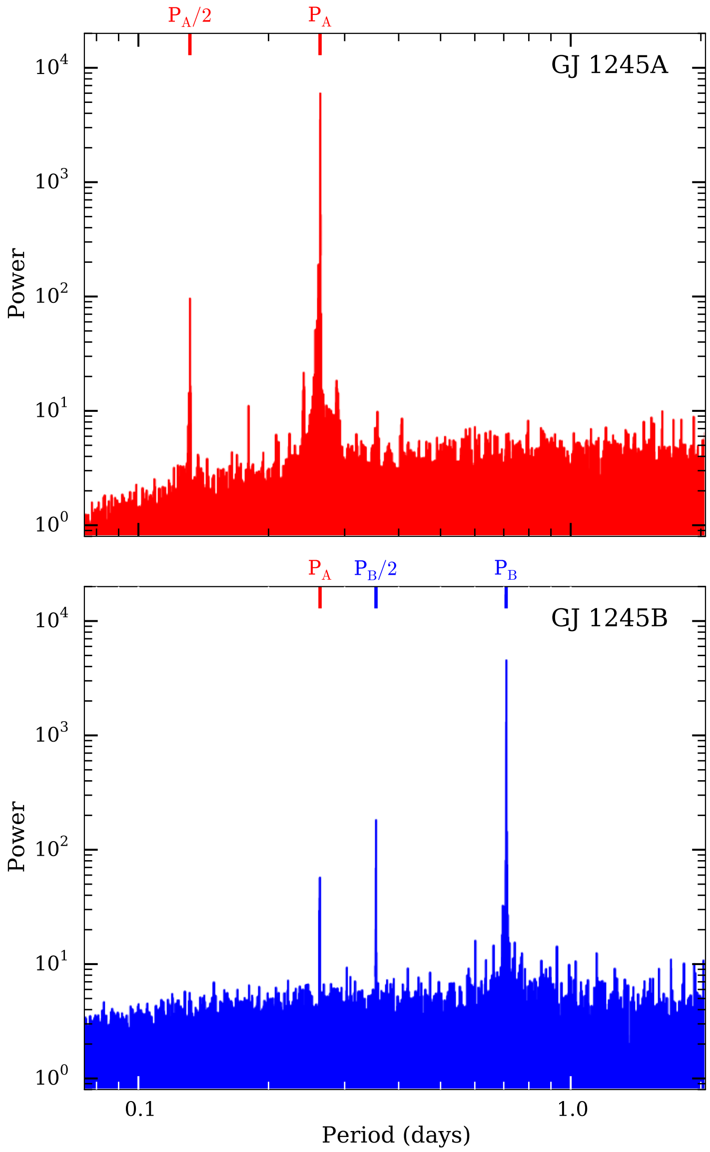

Figure 2.5: Lomb-Scargle periodograms for the four year, long cadence, separated light curves. The light curves were de-trended and converted to units of relative flux prior to generating the periodograms. Peaks corresponding to the full and half rotation periods of stars A and B are labeled. The other small peaks in the A component light curve do not correspond to the rotation period of either star, and are likely due to noise.

1.57 at B (Dahn et al., 1976), V, R, and I (Reid et al., 2004), covering the entire Kepler bandpass. Here we neglect the small flux contribution from the C component, as it is ~94% less bright than the A component. In the 2011 ground-based V filter image, the flux ratio is 1.8. The A and B components in their PDC-SAP light curves have a mean flux ratio of 2.0 over the four years of observations. While the A component PDC-SAP light curve appears to be uncontaminated, there is some A component contamination in the B component PDC-SAP light curve. Removing this contamination would raise the flux ratio somewhat higher than 2.0, in closer agreement with our models, but further from the ground-based data. The discrepancy between the PRF model and the ground-based photometry does not affect our results, other than to offset the flare energy distributions (see §2.4), but we discuss it here for completeness.

If the discrepant flux ratio were due to a systematic misassignment of flux by the model, it should appear in the model residuals. The residuals in the lower right panel of Figure 2.2 are typical of those for the model fits over the four years of data. Note that the residuals can have both negative and positive values, as the model can overpredict or underpredict the flux in a pixel. While the residuals for an individual pixel are as large as a few thousand e^{-} s^{-1}, this represents $\lesssim$ 1% of the total flux in the pixel mask of approximately 500,000 e^{-} s^{-1}.

Furthermore, the residuals show no spatial correlation, in the sense that the model does not systematically assign more flux to one component at the expense of the other. We verified this for each quarter of data by examining the 15 nearest pixels to the A and B component source locations. If a pixel was close to both components, it was assigned to the nearest component. For these two regions of pixels that "belong" to each component, we calculated the residuals between the observation and the model. The sum of the residuals across each region was relatively small, between a few hundred to a few thousand e^{-} s^{-1}. This is not large enough to explain the unexpectedly large flux ratio consistently obtained by the model fit. It appears that the PRF model is accurately reproducing the true PRF, and that the PRF itself is causing the B component to appear fainter relative to the A component than it is in ground-based images.

Potential sources of error in the PRF model listed in Bryson et al. (2010) are changes in focus since the commissioning observations, blends or variability in the stars used to compute the model, CCD non-uniformities, and the PRF dependence on star color, which was not modeled. The dithering observations of a finite number of calibration stars did not sample every pixel on the detector, so the PRF model must interpolate to be defined over the entire detector, limiting its accuracy. These and other factors may contribute to the residuals in the models, as well as the intra-quarter variations in angular separation.

While the residuals within a given pixel can be relatively large, the sum of the residuals across the mask remains small, of the order a few hundred e^{-} s^{-1}. This means that the model is recovering all of the flux in the mask, although in some cases it may be assigning some flux to the wrong component. Despite the discrepant flux ratios we obtain, the latter scenario appears unlikely, given the lack of starspot signal contamination in the A and B component light curves. While it is possible that our residuals and the flux ratio could be improved by additional modeling, the PyKE routines and the PRF model were developed by the Kepler science team, and we did not endeavor to augment them. Based on the overall strong agreement with the astrophysical constraints outlined above, we believe our light curves represent the best-fit models, and can reliably be used for the analysis that follows.

2.3 Starspot Evolution

We used the separated, long cadence light curves to analyze the starspot evolution of each star, as the 30 minute cadence sufficiently samples the 8 and 17 hour period starspot modulations. In this section we describe how long-term trends were removed from the light curves, and examine the evolution of the starspot features.

2.3.1 Light Curve De-trending

The separated light curves exhibit smooth, long-term trends that are typical of uncalibrated Kepler data. M dwarfs have been observed to exhibit long-term VRI photometric variability of up to 5% on multi-year timescales (Hosey et al., 2015). Such variations could in principle be detectable in our data. Unfortunately, because Kepler was not designed for absolute photometry, we are unable to determine whether the observed long term trends are physical or due to instrument systematics. Because our starspot analysis is concerned with short-term changes in the relative brightness of each star, we simply removed these long term trends and normalized the light curve into units of relative flux as described below.

We first smoothed the light curve using the one-dimensional Gaussian filter in the Python SciPy package, in order to trace the low frequency trends in the light curves without affecting the higher frequency starspot signals. A Gaussian filter functions as a low pass filter, and has a Gaussian frequency response function. The standard deviation, σ, of the kernel determines the cutoff frequency of the filter. Increasing σ decreases the cutoff frequency. In addition to long-term trends, the light curves also have some discontinuities that occur at gaps in data. We addressed this by identifying all data gaps longer than 0.5 days, and smoothing each section of light curve separately. There remained a few discontinuities that did not occur at data gaps, which we also analyzed individually.

So that flares did not skew the de-trending, we performed a initial smoothing with a kernel size of 10σ, and then rejected all points on the original light curve that were more than two standard deviations away from the smoothed light curve. We then smoothed the original light curve, with flares removed, using a kernel size of 40σ. We chose this kernel size because a Gaussian filtering of evenly spaced data at a 30 minute cadence with a 40σ kernel completely attenuates all signals below 1 day. The resulting smoothed light curve does not contain the starspot modulations, but traces the long term trends in the original light curve. The final, de-trended light curve was produced by subtracting the smoothed light curve from the original light curve, and then dividing by the median flux value of the entire un-smoothed four year light curve. The de-trended light curve has units of relative flux, or

$$\frac{\Delta F}{F} = \frac{f - f_s}{f_0} \tag{2.1}$$

where f is the flux in the original light curve, f_s is the flux in the smoothed light curve, and f_0 is the median value of f over the four year dataset. We stress that the purpose of this de-trending is to trace the low frequency trends and convert the light curve to units of relative flux. The size of the Gaussian kernel was chosen so that the de-trending did not affect the short period starspot signals.

2.3.2 Differential Rotation

Because the light curves represent the integrated flux from the hemisphere of the star visible at a given time as the star rotates, we are limited in our ability to determine the spatial distribution of the spot regions. For instance, we cannot say whether there are a few large spots or many small spots distributed over the star. We therefore refer to the light curve modulations as dark and light "features", with the minimum in the modulation corresponding to the visible hemisphere of the star that has the largest amount of spot coverage.

However, there are some basic measures of the starspot evolution that can be obtained from the light curves. Figure 2.6 shows the relative amplitudes of the starspot modulations as a function of time, with the light curves averaged in 10 day bins. The A component modulation generally has a larger relative amplitude, but the modulations on both stars show significant variations in amplitude over time. As a check of our models, we performed the same de-trending procedure on the long cadence PDC-SAP light curve for the A component, and the relative amplitude evolution appears nearly identical to that from our A component model light curve in Figure 2.6. The changes in starspot modulation amplitude are consistent with the spectropolarimetric results of Morin et al. (2010), who saw changes in the large scale magnetic field on GJ 1245B during a three year observing campaign.

Another measure of the starspot evolution is to examine if there is any phase shift in the starspot modulation. We assume that the modulations are due to darker spot regions rotating into and out of view, changing the integrated flux from the visible hemisphere of the star. Thus the starspot modulation as a function of rotation phase gives an indication of how the spots are distributed longitudinally on the star. In Figure 2.7, the light curves have been phase-folded at the respective rotation period of each star, and then averaged in

10 day bins. The light curves have been folded over two phases for visual clarity. A more detailed description of this phase-folding procedure and its application to modeling starspot features will be given in a forthcoming paper (Davenport et al. in prep). We fit the starspot features with bivariate Gaussians, where the x and y-dimensions are time and phase, and the z-dimension is relative flux. A cut through a bivariate Gaussian along the x-y plane creates an ellipse. In Figure 2.7, we cut through each Gaussian at its 2σ value, and represent the time axes of the resulting ellipses as yellow lines. The purpose of these fits is to guide the eye, and to enable a quantitative discussion of the spot evolution.

These stars are remarkable for the long-lived nature of their spot features. On the A component, we fit two spot features, both of which remain at nearly constant phase. This could also be interpreted as a single, long-lived spot. On the B component, we fit three spot features, all of which show a more rapid phase evolution than the features on the A component. Most notably, there is a dark feature migrating from phase $\sim$0.5 to $\sim$0.0 between days $\sim$350 and $\sim$700. This feature coincides with the minimum in the relative amplitude seen in Figure 2.6, indicating that the spot coverage was temporarily more evenly distributed with longitude. As is the case for the entire light curve, there is almost no signal present from the A component in this section of the B component light curve. This rules out the migrating feature being caused by contamination from the A component.

The phase evolution of these features can be explained by differential rotation. For example, a spot near the pole and a spot near the equator would appear to shift in phase relative to each other if there is a variation in rotation rate with latitude. The features in Figure 2.7 could potentially be due instead to the meridional flow of spots, or the emergence and disappearance of spots. However for component B, the former effect is too slow to explain the rapid phase evolution, and the latter is unlikely to result in the coherent phase evolution that is observed. The rate of change of phase with time, $\Delta\Omega$, reported in Table 2.2, gives a lower limit on the difference in rotation rate between the equator and the pole. Differential rotation also affects the measured period of the starspot modulation if spots are present at different latitudes. This creates some uncertainty in the rotation period determination.

Analyzing each of the 9 sub-quarters (∼1 month in duration) of short cadence separated light curves individually, we find mean rotation periods of 0.2632 ± 0.0001 and 0.709 ± 0.001 days for the A and B components, respectively. While the exact period determined depends on the subset of data analyzed and its duration, we confirm the rotation periods reported in Paper 1 within the uncertainties quoted above.

2.4 Flares

The 1 minute sampling of the short cadence data is most sensitive to flares. Although some flares are evident in the long cadence data, we have found that the 30 minute sampling makes it difficult to directly compare the measured energies to the short cadence data. Therefore we limit our flare analysis to the separated short cadence light curves, which comprise 3 quarters of Kepler monitoring. In this section, we describe how flares were identified in the light curves, and how the flare samples were prepared. We next discuss the effects of non-linear CCD response for high energy flares. Finally, we determine flare rates for each star, characterize their power law distributions, and determine the fraction of the stars' total energy emitted in flares.

2.4.1 Flare Identification

We identified flares using the automated selection procedure described in §2.1 of Paper 2. Briefly, the light curves were first iteratively smoothed to remove the periodic starspot modulations. This step is necessary because many flares have amplitudes smaller than the starspot modulation, and therefore would not be identified by a simple threshold search of the unmodified light curve. We note that this is a different smoothing procedure than the one described in §2.3. Here the function is to remove the starspot signal but preserve the flares. Flare candidates were identified as two or more consecutive observations with positive flux excursions more than 2.5 times the standard deviation of the smoothed light curve. The light curves with the tagged flare candidates were visually inspected to ensure that the selection procedure did not mistakenly identify data gaps or discontinuities as flares. Instances where

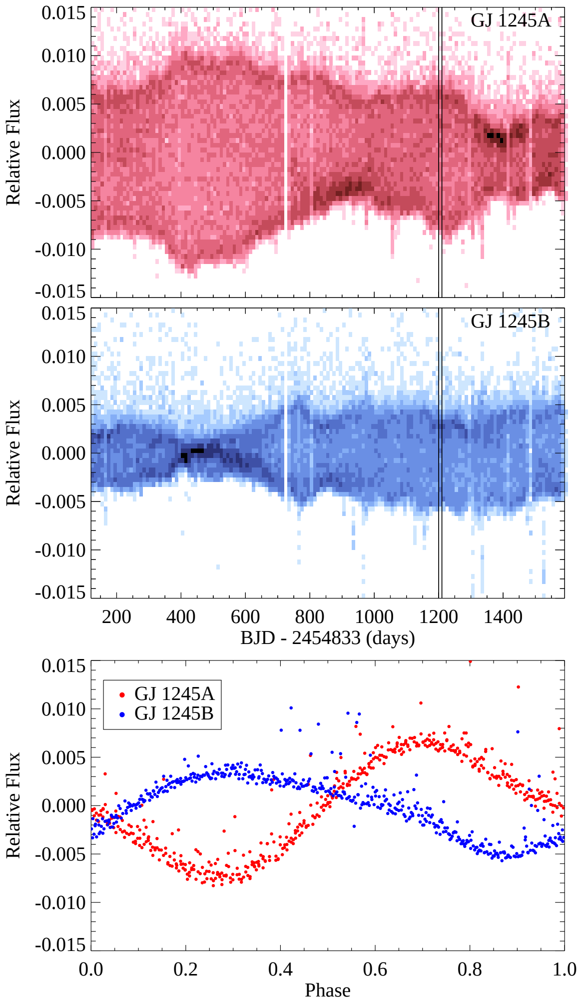

Figure 2.6: The top two panels show the relative amplitudes of the starspot modulations versus time, with the light curves averaged in 10 day bins. In the bottom panel, phase-folded light curves are plotted for the bins represented by the vertical lines in the top two panels. The contours in the top two panels correspond to the density of points in the bottom panel. Note how the amplitude of the light curves in the bottom panel corresponds to the amplitude of the contours in the top two panels. Flares are shown as positive flux excursions, while the negative excursions are due to small errors in the detrending discussed in §2.3.

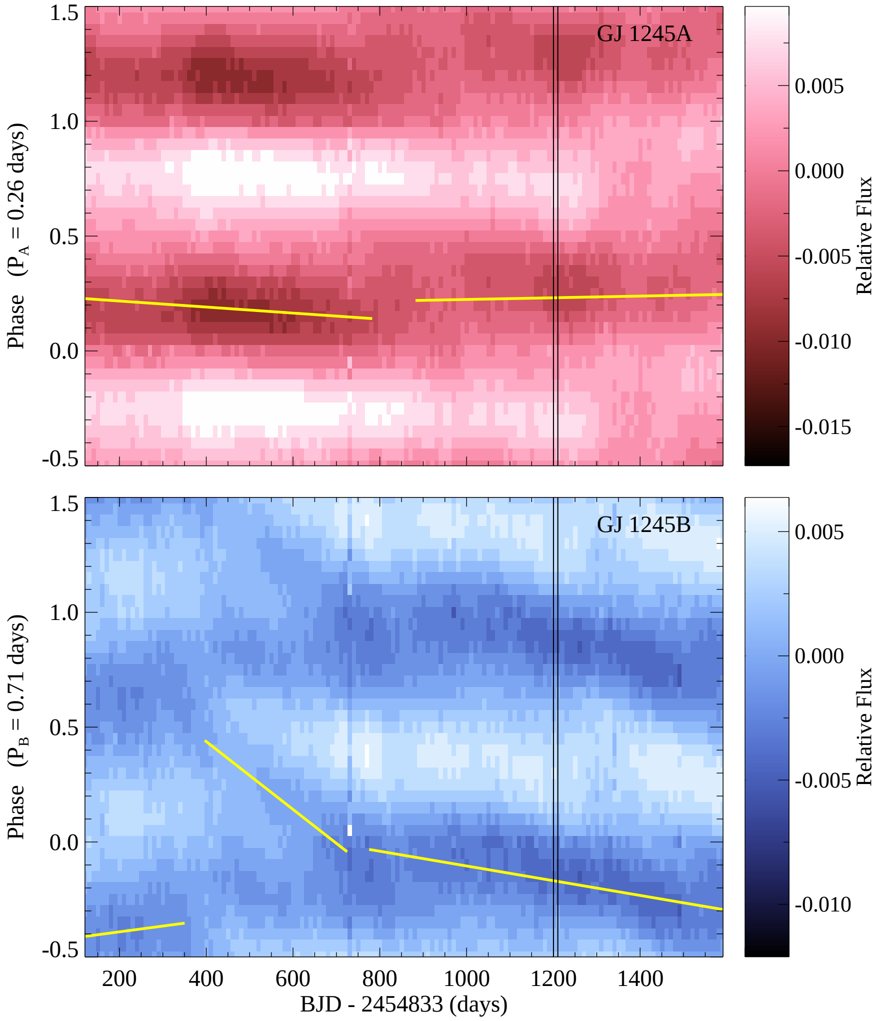

Figure 2.7: Starspot modulation phase versus time. The light curves have been folded over two phases at the respective rotation period of each star, and averaged in 10 day bins. In this figure, the contours represent relative flux. For the bins represented by the vertical black lines, note how the darkest contours correspond to the minima in the phase-folded light curves in the bottom of panel of Figure 2.6, at phase 0.3 and 0.9 for components A and B, respectively. We fit the spot features with bivariate Gaussians. Yellow lines represent the 2σ values along the time axis of the Gaussians.

this occurred were removed from the sample.

Due to noise in the light curves, there is a minimum flare energy below which we cannot reliably identify flares. Here we determine the energy of a flare in terms of its equivalent duration, i.e., the area under the flare light curve, measured in relative flux units. The calculation of equivalent duration is discussed in greater detail in Hunt-Walker et al. (2012). Equivalent duration has units of time, but is not to be confused with the duration of time over which the flare occurred. Multiplying the equivalent duration by the quiescent luminosity of the star gives the flare energy.

For a flare of a given equivalent duration, $\mathcal{E}$, and duration, τ, in time, we define the signal-to-noise (S/N) of the flare as

$$\mathrm{S/N} = \frac{\mathcal{E}}{\sqrt{\mathcal{E} + \sigma\tau}} \tag{2.2}$$

where σ is the standard deviation of the "continuum" light curve around the flare. Each flare candidate was visually inspected, in descending order of S/N. For both stars, spurious flare events began to contaminate the sample at a S/N value of 1.4. We therefore excluded flare candidates below this threshold. The S/N of flares correlates with equivalent duration, and therefore energy. Although a S/N value of 1.4 corresponds to the same equivalent duration value of 2.3 seconds for both stars, it corresponds to a lower flare energy limit on the B component, because a lower energy flare is easier to detect above the quiescent flux of the intrinsically fainter B component. Although many of the flare candidates below the threshold are real flare events, we set the threshold conservatively high to limit the impact of systematic effects in the model light curves.

As determined in §2.3 of Paper 1, the total quiescent luminosity of the GJ 1245 system in the Kepler bandpass is $\log L_{Kp} = 30.22$ erg s^{-1}. The quiescent luminosity was determined using the apparent Kepler magnitude of the GJ 1245 system listed in the Kepler Input Catalog, the zero-point of the Kepler magnitude system, and the trigonometric distance of the system. The individual quiescent luminosities of components A and B can be found from the total system luminosity if the flux ratio of the two stars in the Kepler bandpass is known, neglecting the small flux contribution of the C component. We adopt the flux ratio of 1.64 in the *R* filter based on the values in Reid et al. (2004). Among the standard photometric filters, the *R* filter is most representative of the Kepler wavelength response. This yields individual quiescent luminosities of $\log L_{Kp} = 30.01$ and 29.80 erg s^{-1} for the A and B components, respectively. We note that this adopted flux ratio is significantly smaller than that of our PRF models. Given the uncertainties associated with the Kepler PRF, we prefer the well calibrated optical photometry. We assume that the discrepant PRF model flux ratio is the result of the spacecraft optics and detector, that changes in brightness due to starpots and flares are proportional to the baseline, quiescent brightness. Thus this does not affect the measured relative flare energies, i.e, the equivalent durations.

Because the light curves were produced by fitting a PRF model to the pixel-level data, it is possible that a flare event, particularly one with a large amplitude, could appear in the pixels of both stars and be included in both light curves despite having originated from only one component. In this case, the flares in each light curve should reach their peak fluxes at the same time, and have similar light curve morphologies. Approximately 4% of the flares in the sample for each star had peak times that differed by less than 3 minutes from a flare on the other star above a S/N of 1.4. The remaining 96% were considered as separate events. Given the 1 minute time sampling of the short cadence data, two events occurring more than 3 minutes apart should easily be resolved.

The 4% of flares that overlapped by less than 3 minutes were discarded from the samples for both stars, with the exception of a few flares for which the equivalent duration was a factor of 10 greater on one star than the overlapping flare on the other star. In these cases, we were confident as to which component the flare originated from, and kept the larger equivalent duration flare while discarding the smaller. The overlapping flares present several issues for the flare samples. The A component is brighter, so a flare from component A is more likely to contaminate component B than vice versa. However, as they only represent 4% percent of the flares, this does not significantly bias the sample. It is possible that some of the discarded overlapping flares are in fact two separate events that happened to occur on each star at nearly the same time. The likelihood of such events is rare, and because flares occur randomly in time this should not affect the relative occurrence rates for each star.

We have neglected the contribution of the C component to the flare sample for the A component. While the C component may flare often, nearly all of its flares would be undetectable in the Kepler data. For a flare on the C component to be visible in the Kepler data, it must be brighter than the quiescent flux of the A component. This would require a flux enhancement of over 3 magnitudes. The flare frequency distributions (FFDs) of Hilton (2011) put an upper limit on the occurrence of such flares on M6 – M8 stars at approximately once per 100 hours. This is a conservative upper limit on the occurrence rate, as the flare sample was based largely on M6 and M7 stars, so the occurrence rate of such large flares would be lower for an M8 analog to GJ 1245C. During the 5,491 hours of Kepler short cadence exposures of the GJ 1245 system, we would expect to detect no more than 55 flares from the C component. However, such a flare would only remain at its peak, detectable brightness for a short time. They would appear as short-lived, low energy flares in the A component light curve, and would have been discarded by the minimum signal to noise threshold applied to the sample.

2.4.2 CCD Non-linearity and Saturation

Upon investigation of the target pixel files, we found that some high energy flares caused the Kepler CCD to respond non-linearly, and in some cases saturate. The effect on our flare samples is discussed in §2.4.3, but we first provide some details of our analysis, as they are relevant to other investigations of impulsive phenomena in the Kepler dataset. We examined the raw counts in the short cadence target pixel files, focusing on the brightest pixels for each component, as they are the most likely to respond non-linearly during a flare. It was crucial to inspect the uncalibrated raw counts, because the calibrated fluxes can disguise the effects of non-linearity and saturation. During Quarters 8, 10, and 11, the median counts in the brightest pixel for the A component were 46%, 83%, and 50% of the full well depth (10093 ADU; Van Cleve et al. 2009). The corresponding values for the B component were 37%, 45%, and 45%. Because the stars changed locations in the focal plane between spacecraft rolls, roughly half of the flux from the A component was concentrated in a single pixel during Quarter 10. In Quarters 8 and 11, the flux was distributed more evenly across several pixels, as was the flux from the B component during all three quarters. As the quiescent counts in these pixels are already a significant fraction of the full well depth, a flare that temporarily increases the counts in a pixel by more than a factor of two or three is a cause for concern.

The classical flare temporal morphology discussed in § 2.2 of Paper 1 is characterized by a rapid rise in flux, followed by a rapid decay, and then a slower exponential decay. A short cadence observation represents the sum of nine 6 second exposures (Van Cleve et al., 2009). Given the rapid rise and decay of a typical flare, a pixel could reach its full well depth in one or more these exposures even if the mean counts for all nine exposures is less than the full well depth. In this case the fluxes measured for the flare would only be lower limits. Because the CCD responded non-linearly, and because no information is retained on the individual 6 second exposures, we are unable to quantify the extent of the energy underestimation.

Although up to 25% and 9% of the flares in the sample for components A and B, respectively, may have caused the detector to respond non-linearly and potentially saturate, it does not appear that this caused any significant CCD bleeding effects onto adjacent pixels, with one notable exception. For the largest amplitude flare in the observations, bleeding along two pixel columns is evident, and at least 13 pixels are saturated during the brightest point in the flare. Additional bleeding likely occurred in pixels outside of the target pixel mask. The flare appears in the separated light curves of both stars, and was discarded from the sample under the criteria described previously.

2.4.3 Flare Rates and Statistics

The statistics of the flare samples are summarized in Table 2.1, and the flare energies are plotted as a histogram in Figure 2.8. This sample is comprised of all flares that met the sample criteria described in §2.4.1, including those affected by CCD non-linearity. The sharp turnover at lower energies is the result of the signal to noise cutoff in the flare samples. We

Table 2.1. Flare Statistics

Star	# Flares	Flares per day	Range $\log E_{Kp}$ (erg)
GJ 1245A	683	3.0	30.38 - 32.63[a]
GJ 1245B	605	2.6	30.16 - 33.14[a]

[a] This sample is comprised of all flares that met the sample criteria described in §2.4.1, including those affected by CCD non-linearity. The upper energy ranges are therefore lower limits.

note that by virtue of being on the same pixel masks, the two stars were observed for the same amount of time, so their flare distributions can be compared without normalization. The energy distribution histograms are similar, but are offset in energy due to the different quiescent luminosities of the two stars. For flares above the S/N threshold, the average rates are also similar, with the A component exhibiting 3.0 flares per day, compared to 2.6 on the B component. These similarities are somewhat unexpected if activity correlates with rotation period, given that the A component rotates almost three times faster than B.

The cumulative FFDs for components A and B are shown in Figure 2.9. The FFD gives the cumulative number of flares greater than or equal to the given energy that occur each day. Flare frequency is plotted versus energy on the top panel of Figure 2.9, and versus equivalent duration in the bottom panel. While it is useful to present the FFD in physical units, this is not a fair representation of the relative activity of the two stars. In the top panel, most of the offset between the two FFDs is due to the quiescent luminosity difference of the stars. In terms of equivalent duration, the FFDs lie closer together. The equivalent duration distribution represents the energy released in flares relative to the total energy output of the star (see Eqn. 6 below).

Flare occurrence is typically modeled using a power law distribution in energy of the form

$$N(E)dE = \beta E^{-\alpha} dE \tag{2.3}$$

where β is a constant. The slope of the cumulative FFD is equal to $1 - \alpha$. As seen in the bottom panel of Figure 2.9, the FFDs for both stars are not fit by single power laws, shown as green lines. This is due to the non-linear response of the CCD to high energy flares (see §2.4.2). Because the equivalent duration (and energy) measurements for these flares are only lower limits, we underestimate the frequency of high energy flares, causing the FFD to artificially steepen at high energies. The A component FFD begins to deviate from a single power law at an equivalent duration of approximately 10 seconds. The B component FFD is well fit by a single power law up to an equivalent duration of approximately 25 seconds. As expected, the deviation from a single power law is more pronounced for the A component. Due to its greater apparent brightness, a lower energy flare on the A component will cause its corresponding pixels to respond non-linearly compared to the fainter B component. Due to the non-linear response of the CCD, we are unable to determine if there is any intrinsic change in the power law slope at higher energies.

The measured energies for the high energy flares in our sample are compromised due to non-linear CCD response, and they are not included in the power law fits. Some turnover is evident in the FFDs below an equivalent duration of 2.7 seconds, due to incomplete detection of the lowest energy flares. We therefore fit power laws to the FFDs over an equivalent duration range of 2.7 – 10.0 seconds for each star. We assume that the samples are complete in this range, that these flares did not cause the detector to respond non-linearly, and that their energies are well constrained. The uncertainty in the number of observed flares at a given equivalent duration was assumed to follow a Poisson distribution. The largest contribution of uncertainty in the equivalent duration measurements is due to fitting of the underlying starspot modulation. This sets the baseline flux against which the flare is measured. We found that changes in the size of the window of quiescent light curve around the flare that is fit can change the measured equivalent duration by up to 10%. In most cases, the change was less than a few percent, but we conservatively set the uncertainties on all measured equivalent durations at 10%.

The power law fit was performed using a Bayesian Markov chain Monte Carlo-based algorithm (Kelly, 2007). The slopes with uncertainties are reported in Table 2.2. The FFDs for GJ 1245 A and B presented here supersede the combined FFD of Paper 1, which was based on the combined PDC-SAP light curve, and included flares from both stars. The power law slope for the combined FFD in Paper 1 was -1.32 ($\alpha = 2.32$), steeper than what we report here for the individual stars as a result of including the lower limits for the high energy flares in the power law fit.

In Figure 2.10, the number of flares and flare energies occurring on each star are plotted versus rotation phase. Only flares with equivalent durations less than 10 seconds are plotted, for which the energies are well constrained. For reference, one month of the nine month long separated short cadence light curves have been folded at the rotation period of the respective star. To the eye, the number distribution on the A component is suggestive of a correlation with rotation phase. However, any potential phase dependence is not statistically significant, given the assumed Poisson errors. The histogram is consistent with a constant distribution at the median value of the histogram with a reduced χ^2 of 0.87. For the B component histogram, the reduced χ^2 of constant fit is 0.88. Similarly, the flare energies show no correlation with rotation phase. These results suggest that the flare-producing regions are uniformly distributed in longitude across the star.

2.4.4 A New Metric for Comparing Flare Rates

From the power law distribution in Equation 3, an analytical relation can be obtained for the total energy, E_{tot}, released from flares with energies in the range E_0 to E_1.

$$E_{tot} = \frac{\beta}{2-\alpha}\left(E_1^{2-\alpha} - E_0^{2-\alpha}\right) \tag{2.4}$$

Alternatively, in terms of equivalent duration, $\mathcal{E}$

$$\mathcal{E}_{tot} = \frac{E_{tot}}{L_{\rm Kp}} = \frac{1}{L_{\rm Kp}} \frac{\beta}{2-\alpha} \left(\mathcal{E}_1^{2-\alpha} - \mathcal{E}_0^{2-\alpha}\right) \tag{2.5}$$

The constants for these relations are determined from the power law fit to the FFD. The total luminosity emitted in flares relative to the total luminosity through the Kepler bandpass is

$$\frac{L_{fl}}{L_{\rm Kp}} = \frac{E_{tot}/t_{exp}}{L_{\rm Kp}} = \frac{L_{\rm Kp}\,\mathcal{E}_{tot}/t_{exp}}{L_{\rm Kp}} = \frac{\mathcal{E}_{tot}}{t_{exp}} \tag{2.6}$$

where t_{exp} is the total exposure time of the observations. Note that by expressing the ratio $L_{fl}/L_{\rm Kp}$ in terms of equivalent duration, the Kepler luminosity cancels out, removing a source of uncertainty in comparing $L_{fl}/L_{\rm Kp}$ for different stars.

The values of $L_{fl}/L_{\rm Kp}$ for components A and B reported in Table 2.2 represent an integration of the power law distribution (Eqn. 5) over the equivalent duration range 2.7 – 10.0 seconds. These agree well with the values found by simply summing the equivalent durations of the observed flares over the same range. Note that in Table 2 of Paper 1, $L_{fl}/L_{\rm Kp}$ is reported as f_E. The values reported here supersede that of Paper 1, which was based on the unresolved light curve for components A and B, and was integrated over a wider equivalent duration range. We caution that due to the nature of power law distributions, $L_{fl}/L_{\rm Kp}$ depends on the range of equivalent durations (or energies) considered. Thus the limits of integration should be reported along with the values for $L_{fl}/L_{\rm Kp}$, and taken into account when comparing to other stars.

2.5 *Discussion*

We have used the PyKE PRF modeling routines to produce separate light curves for two active M dwarfs, GJ 1245 A and B, which were previously unresolved in the Kepler pipeline processing. Comparison of the model output to well constrained astrophysical parameters of the system confirms that we have successfully deconvolved the two stars. The model recovers the starspot modulations and flares on each star with minimal cross-contamination. The angular separation of the two stars, as determined by the PRF models, decreased in

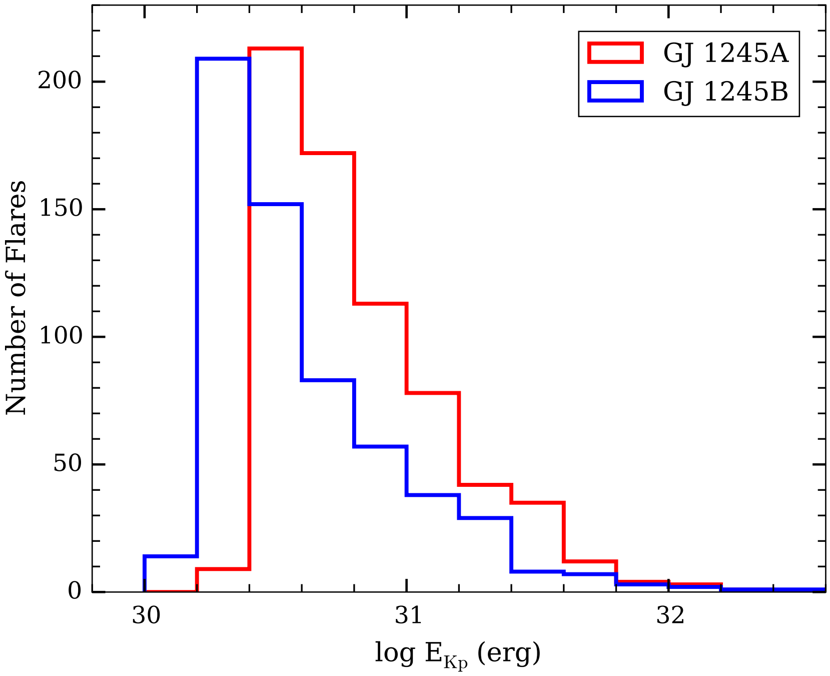

Figure 2.8: Flare energy histograms for stars A and B. The sharp cutoffs at low energy are due to the minimum signal to noise threshold assigned to the flare sample.

a manner consistent with an astrometric perturbation due to the orbit of the unseen C component. Unfortunately, the 4 years of Kepler observations only cover ∼25% of the total orbital period, and are plagued by significant systematics. A more robust astrometric analysis lies beyond the scope of this thesis. We hope that our results may encourage others to conduct a more in-depth search for astrometric perturbations in the Kepler dataset.

Because GJ 1245 A and B are coeval and have similar masses, we are able to take a holistic view of the dependence of flare occurrence and differential rotation on rotation rate. This is summarized in Table 2.2, in which we also include results for the active M4 star GJ 1243. Although we do not know the age of GJ 1243 relative to the GJ 1245 system, it is a useful comparison star that has been studied in a similar manner using Kepler data. The rotation period for GJ 1243 is taken from Paper 1, while the flare sample is taken from

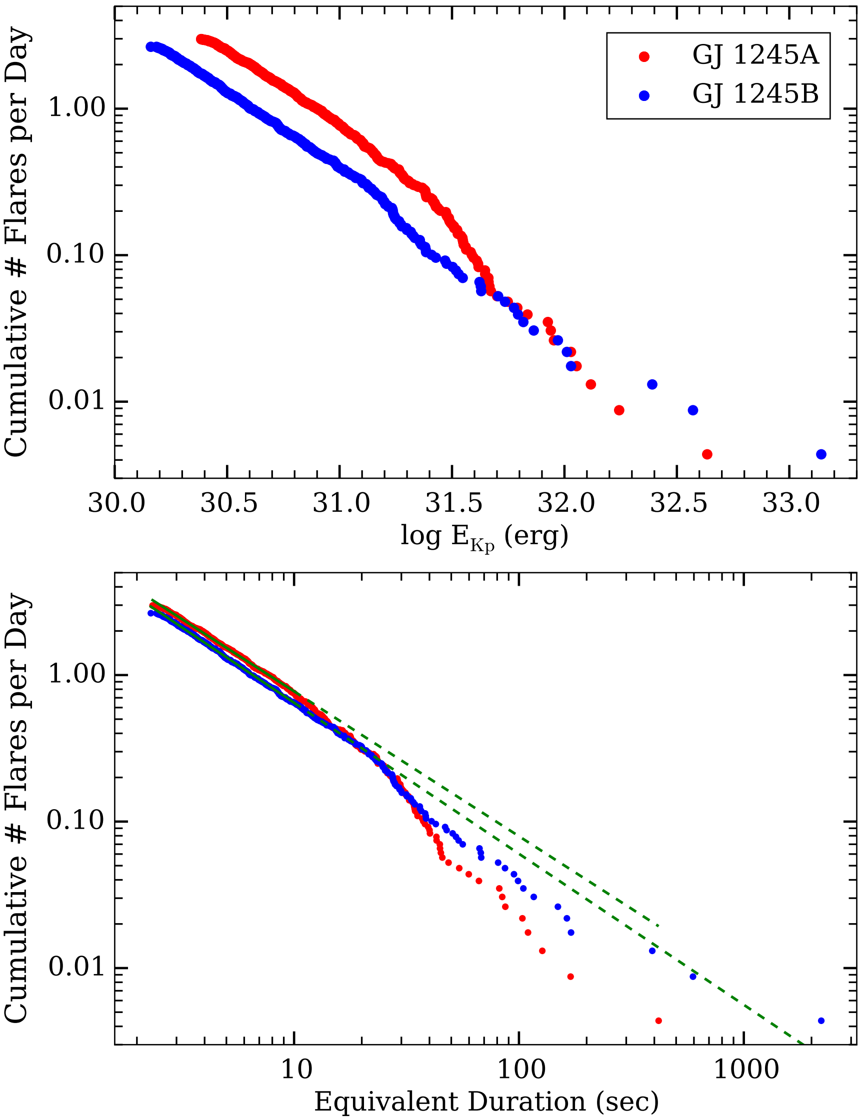

Figure 2.9: The cumulative flare frequency distributions for stars A and B are plotted versus energy (top panel) and equivalent duration (bottom panel). For a given energy (or equivalent duration) on the x-axis, the cumulative number of flares per day greater than or equal to that energy is given on the y-axis. The power law fits (solid green lines) do not include flares with $E_{Kp} > 32.3$ (dashed green lines).

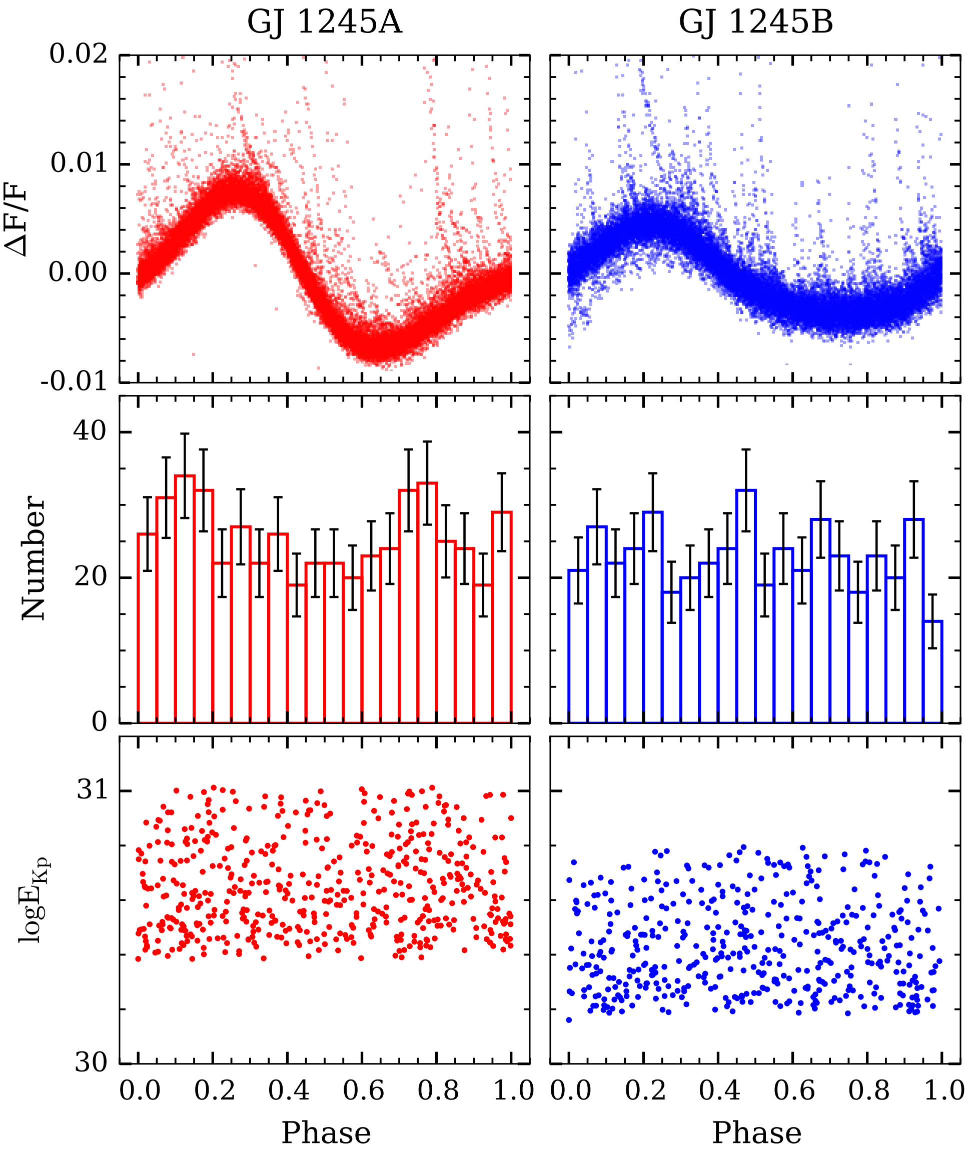

Figure 2.10: In the top panels, one month of short cadence separated light curves have been folded at the rotation period of each star. The number of flares (middle panels) and flare energy (bottom panels) for the 9 month dataset are plotted versus rotation phase. No correlations are seen with rotation phase.

Table 2.2. Comparison of Active M Dwarfs

Star	$\log L_{Kp}$ (erg s^{-1})	P_{rot} (days)	$\log L_{fl}/L_{\rm Kp}$[b]	α[c]	$\Delta\Omega$ (rad day^{-1})	$\log L_{\rm H\alpha}/L_{\rm bol}$
GJ 1243[a]	30.67	0.5927	-3.78 ± 0.01	1.92 ± 0.01	0.004	-3.56
GJ 1245A	30.01	0.2632	-3.93 ± 0.02	1.99 ± 0.02	0.0008	-4.14
GJ 1245B	29.80	0.709	-4.00 ± 0.02	2.03 ± 0.02	0.009	-3.97

[a] The values for GJ 1243 are taken from Papers 1 and 2.

[b] These values represent the integration of the energy distribution power law over the equivalent duration range 2.7 – 10 seconds.

[c] The slope of the cumulative FFD is $1 - \alpha$.

Paper 2. For consistency, the flare energy distribution slope, α, and the value for L_{fl}/L_{Kp} for GJ 1243 were determined using the same criteria described in §2.4 for GJ 1245 A and B. The measure of differential rotation, $\Delta\Omega$, corresponds to the value for the fastest migrating spot feature on each star. It represents a lower limit on the shear between the equator and the poles, expressed in radians per day. Differential rotation on these three stars will be examined fully in a forthcoming paper (Davenport et al. 2014, in prep.). Equivalent widths for Hα are reported in Paper 1. These were converted to $L_{\rm H\alpha}/L_{\rm bol}$ via multiplication by the χ factor (Walkowicz et al., 2004), which is the ratio between the continuum flux near Hα and the bolometric flux.

Ideally, the flare rates among stars should be compared in terms of the luminosity emitted in flares relative to the bolometric luminosity, L_{fl}/L_{bol}, similar to the use of $L_{\rm H\alpha}/L_{\rm bol}$ to compare the luminosity emitted in $H\alpha$. Observationally, we have determined the luminosity in flares relative to the luminosity in the Kepler bandpass, $L_{fl}/L_{\rm Kp}$. Conversion of $L_{fl}/L_{\rm Kp}$

to L_{fl}/L_{bol} requires knowing the color-dependent bolometric correction for the Kepler filter, which is being developed in a future work (Davenport et al. 2015, in prep.). We caution that the value of $L_{fl}/L_{\rm Kp}$, and therefore L_{fl}/L_{bol}, depends on the range of equivalent durations over which the energy distribution is integrated. These considerations must be taken into account when comparing different stars, especially those that differ significantly in spectral type.

Because GJ 1245 A and B are nearly the same color, we can neglect the bolometric correction, and compare their values of $L_{fl}/L_{\rm Kp}$ as representative of L_{fl}/L_{bol}. We find that GJ 1245A emits a slightly higher fraction of energy in flares, while Paper 1 found that GJ 1245B emits a slightly higher fraction of energy in Hα emission. Interestingly, the values of $L_{fl}/L_{\rm Kp}$ and $L_{\rm H\alpha}/L_{\rm bol}$ are comparable for the range of flare equivalent durations we have considered. The scatter in $L_{\rm H\alpha}/L_{\rm bol}$ for stars of the same spectral type (West et al., 2011) easily accounts for the difference between the A and B components. A similar scatter in $L_{fl}/L_{\rm Kp}$ is likely also present. We therefore do not find a correlation of activity parameters with rotation rate in the GJ 1245 AB system. From the measured rotation periods, and assuming radii of 0.15 $R_{\odot}$, GJ 1245 A and B have rotational velocities of 11 and 29 km/s, respectively. This well above the threshold velocity of $\sim$4 km/s, where Mohanty & Basri (2003) found no correlation between rotation rate and activity for stars of this spectral type.

If we compare GJ 1245 A and B to GJ 1243, we find that GJ 1243 has the largest value of $L_{fl}/L_{\rm Kp}$, with a trend of increasing $L_{fl}/L_{\rm Kp}$ with $L_{\rm Kp}$. Lacy et al. (1976) found the opposite trend in the U and B bands, although the values of $L_{fl,U}/L_U$ and $L_{fl,B}/L_B$ were $1-3$ orders of magnitude larger than what we measure in the Kepler bandpass. This underlines the importance of converting measures of L_{fl} taken in different bandpasses to L_{fl}/L_{bol}. Future work (Davenport et al. 2015, in prep.) will apply the flare light curve template presented in Paper 2 to understand the changes in relative flare luminosities in different bandpasses.

The flare energy distributions of all three stars have values of $\alpha \approx 2$. This is relevant to studies of the Sun, as the heating of the corona could be attributed to flares if $\alpha > 2$ for the solar flare energy distribution at lower energies (Schrijver et al., 2012). However, Paper 2 found that the FFD of GJ 1243 had a shallower slope (smaller α) at lower energies, and that fewer low energy flares were observed than predicted by a power law slope with $\alpha \approx 2$. The flare samples for GJ 1245 A and B are incomplete below our signal to noise threshold. We therefore cannot say whether the stars flare less frequently at lower energies than predicted by the power law, or whether those flares occurred and were simply not detected due to noise.

For GJ 1245 A and B, the number of flares and flare energies show no correlation with rotation phase. The same was observed for GJ 1243 in Paper 1. This is consistent with a scenario where many small flaring regions are distributed uniformly with longitude, while the long lived spot features originate from large, axisymmetric poloidal magnetic fields, as seen in spectropolarimetric Doppler imaging of GJ 1245 B (Morin et al., 2010).

In agreement with previous observations (Collier Cameron, 2007) and models (Küker & Rüdiger, 2011), the amount of differential rotation increases with decreasing rotation rate. The fastest rotator, GJ 1245 A, shows the least differential rotation, and likely rotates as a nearly solid body. The slowest rotator, GJ 1245 B, shows the greatest differential rotation, while the differential rotation of GJ 1243 is intermediate between GJ 1245 A and B. This is among the first observational constraints placed on the effect of rotation rate on differential rotation for M dwarfs, and in the case of GJ 1245 A and B, perhaps the first constraints for objects of the same age.

Our starspot and flare results are among the most detailed for an M dwarf multiple system, and involved an extensive analysis of the Kepler target pixel data. We emphasize the importance of the pixel data, both for the wealth of information they contain, and as a cautionary example of CCD non-linearity and saturation. Other investigations of impulsive phenomena using Kepler may encounter similar effects. In the broader context of stellar activity, these results contribute significantly to the existing dataset for fully convective M dwarfs. Together with other results from the Kepler program, they will help constrain the effects of age and rotation rate on stellar activity.

Chapter 3

TIDAL SYNCHRONIZATION OF KEPLER ECLIPSING BINARIES

The previous chapter investigated the rotation and activity of two fully convective M dwarfs in a wide binary that is not interacting. However, close binaries will tidally interact, changing the rotation rates and thus the activity. Few observational constraints exist for the tidal synchronization rate of low mass stars, despite its fundamental role in close binary evolution.

This chapter analyzes *Kepler* light curves of nearly 3,000 low mass eclipsing binaries (EBs), most of which have small separations due to the geometric probability of eclipses. The *Kepler* data are unique in that the rotation periods of low mass stars can be measured directly from starspot modulations. The challenge of this project is that other sources of variability contaminate the rotation period signals if not properly accounted for, requiring an intensive visual classification of the light curves. After developing a bonafide rotation period catalog of over 800 EBs, this chapter investigates the dependence of tidal synchronization on orbital period, eccentricity, stellar mass, and mass ratio. In addition, an unexpected population of subsynchronous EBs is detected, for which differential rotation is demonstrated to be a plausible explanation.

Material from this chapter was previously published in collaboration with Karl Vyhmeister, Suzanne L. Hawley, Jamel Adilia, Andrea Chen, James R. A. Davenport, Mario Jurić, Michael Puig-Holzman, and Kolby L. Weisenburger in the December 2017 edition of the Astronomical Journal (Lurie et al., 2017), and has been reproduced here with permission of the American Astronomical Society.

3.1 Introduction

At least half of star systems are binaries (Duchêne & Kraus, 2013), and many binaries are close enough that they will tidally interact. The evolution of stars in tidally interacting binaries is fundamentally different than for isolated stars. A tidally interacting system generally tends toward a state of equilibrium, where the orbit is circular, and the stellar rotation (P_{rot}) is coplanar and synchronized with the orbit (P_{orb}) (Hut, 1980). Outside of this equilibrium, binaries where $P_{rot} < P_{orb}$ are supersynchronous, while binaries where $P_{rot} > P_{orb}$ are subsynchronous. Binaries with eccentric orbits are expected to become "pseudosynchronized", so that the rotational angular velocity is nearly equal to the instantaneous orbital angular velocity at periastron (Hut, 1981). A pseudosynchronized binary appears supersynchronous because the orbital angular velocity at periastron is greater than the mean orbital angular velocity.

Tidal interaction can also lead to mass transfer and related phenomena including cataclysmic variables (Warner, 2003), supernovae (Langer, 2012), and degenerate object mergers (Postnov & Yungelson, 2014). Furthermore, tidal interaction can be used to probe the internal structure of stars (Ogilvie, 2014). Given the ubiquity of binaries and the importance of tidal interaction, observational constraints in this area are crucial to understanding stellar populations as a whole.

While numerous observational studies have focused on tidal circularization (e.g., Koch & Hrivnak 1981; Duquennoy & Mayor 1991; Meibom & Mathieu 2005; Van Eylen et al. 2016), progress on tidal synchronization has been limited by three major factors. First, stellar rotation rates are generally more difficult to measure than orbital periods. Second, most studies of synchronization have measured rotational velocities from line broadening. Conversion from rotational velocities to periods depends on the stellar radius and inclination, which may be uncertain. Third, and perhaps most importantly, most synchronization studies have focused on early-type stars with radiative envelopes (e.g., Levato 1974; Giuricin et al. 1984a; Abt & Boonyarak 2004; Khaliullin & Khaliullina 2010). Only a few studies have focused on late-type stars with convective envelopes (Giuricin et al. 1984b; Claret et al. 1995; Meibom et al. 2006; Marilli et al. 2007), where the tidal dissipation mechanism is likely different than in radiative envelopes (Zahn, 1977; Ogilvie, 2014).

The *Kepler* mission offers to greatly expand the number of rotation period measurements of tidally interacting binaries with convective envelopes, because of its unmatched ability to observe a large sample of eclipsing binaries (EBs) and to measure their rotation periods directly from starspot modulations. The Kepler Eclipsing Binary Catalog (KEBC[1], Prša et al. 2011; Slawson et al. 2011; Kirk et al. 2016) contains over 2,800 candidate EBs observed during the original *Kepler* mission. *Kepler* has also revolutionized the study of the stellar rotation period distribution, with tens of thousands of rotation periods measured to date for single stars (e.g. Harrison et al. 2012; McQuillan et al. 2014; Meibom et al. 2011; Nielsen et al. 2013; Reinhold & Gizon 2015).

While most *Kepler* rotation studies have excluded stars with known stellar and substellar companions, Walkowicz & Basri (2013) reported rotation periods for 950 exoplanet candidate (*Kepler* Object of Interest) host stars. This study incidentally measured rotation periods for EBs that were misidentified as transiting exoplanets. 116 systems in that study are confirmed EBs in the *Kepler* false positive list (Bryson et al. 2015), of which 48 have rotation periods within 25% of the orbital period, suggesting that synchronization is occurring. However, rotation periods remain unmeasured for the vast majority of the KEBC.

Here, we systematically measure rotation periods for the KEBC, which allows us to investigate the dependence of tidal synchronization on several key orbital and stellar parameters. In the traditional paradigm, tidal energy is dissipated by convective turbulence in convective regions, and by radiative diffusion in radiative regions (Zahn, 1977). These two processes proceed at different rates, and the rate of tidal evolution for a given star depends on the locations and relative thicknesses of its convective and radiative regions. The rate of tidal interaction also depends on the mass ratio, with the rate increasing for more equal mass bi-

---

[1] `http://keplerebs.villanova.edu`

naries. Also, tidal forces are stronger at smaller separations, so shorter period EBs should be more synchronized. However, a state of true synchronization is impossible in eccentric binaries. Instead, the binary approaches "pseudosynchronization", where the rotational angular velocity synchronizes to the orbital angular velocity at periastron, where the tidal forces are the strongest (Hut, 1981). Thus, mass, mass ratio, orbital period, and eccentricity are all important parameters to investigate.

An unexpected result of our investigation is a population of EBs that are rotating typically 13% slower than synchronous. After ruling out instrumental and numerical causes, differential rotation is the most likely physical explanation. Differential rotation is important to binary evolution in its own right, as it influences magnetic braking through surface activity and the magnetic dynamo (Schatzman, 1962). Reinhold et al. (2013) and Reinhold & Gizon (2015, hereafter RG15) presented differential rotation measurements for thousands of single *Kepler* stars, and examined trends with effective temperature and rotation period. Using a similar technique, we measure differential rotation for the EBs, and demonstrate how differential rotation explains the subsynchronous population of EBs.

The remainder of the chapter is organized as follows. In §3.2, we describe the KEBC and the *Kepler* light curves. In §3.3, we classify the EB light curves and measure rotation periods for EBs with starspot modulations. In §3.4, we examine the dependence of tidal synchronization on orbital period, eccentricity, stellar mass, and mass ratio, while in §3.5 we focus on differential rotation. We present additional results in §3.6, and conclude in §3.7.

3.2 Data

3.2.1 The Kepler Eclipsing Binary Catalog

We began with the 2863 targets in the KEBC downloaded on 2017 March 24. The KEBC includes orbital periods, ephemerides, and primary and secondary (when detected) eclipse depths, widths and phase separations. There are some uncertainties in the KEBC that are relevant to our analysis. A circular EB with nearly equal primary and secondary eclipse depths may be mistaken for an EB with only a primary eclipse at half the given period. Some systems with small eclipse depths may be transiting exoplanets or brown dwarfs, although most have been removed by the KEBC and *Kepler* mission teams. Although substellar companions are not the focus of this work, we include them in our analysis for completeness. In §3.4.3, we use rotation period measurements to identify when the above cases occur.

We excluded the following targets from our sample. There are 11 systems with eclipses at multiple periods (nine with two periods and two with three periods) due to the ambiguity of assigning orbital periods to a measured rotation period. There are 406 targets flagged as uncertain in the KEBC, most of which are contact binaries or ellipsoidal variables and would not have been analyzed in any case. There are 168 targets flagged as heartbeat stars (Kumar et al., 1995; Thompson et al., 2012), which we excluded due to the complex light curves and extreme dynamics of these systems. After these exclusions, there were 2278 EBs remaining that we analyzed.

3.2.2 Eccentricity

Constraints can be placed on the orbital eccentricity from the timing and relative durations of primary and secondary eclipses[2]. These constraints are uncertain upon the argument of periastron ω. In a circular orbit, the primary and secondary eclipses will be separated in phase by 0.5, and will have the same duration, regardless of ω.

Using the timings of primary and secondary eclipses t_{pri} and t_{sec}, $e\cos\omega$ can be approximated as

$$e\cos\omega \approx \frac{\pi}{2}\left(\frac{|t_{sec} - t_{pri}|}{P_{orb}} - \frac{1}{2}\right) \tag{3.1}$$

If $t_{pri} - t_{sec} = P_{orb}/2$, then $e\cos\omega = 0$. This corresponds to either a circular orbit, or an eccentric orbit with $\omega = 90^\circ$. If $t_{pri} - t_{sec} \ll P_{orb}$, then $e|\cos\omega|$ approaches a maximum value of 1, corresponding to a highly eccentric orbit.

---

[2] The eccentricity may also be constrained using the duration differences between ingress and egress (Barnes, 2007a; Barnes et al., 2015).

From the durations of primary and secondary eclipses d_{pri} and d_{sec}, $e\sin\omega$ can be approximated as

$$e\sin\omega \approx \frac{(d_{sec}/d_{pri}-1)}{(d_{sec}/d_{pri}+1)} \tag{3.2}$$

An approximation of the eccentricity can then be determined from the combination of $e\cos\omega$ and $e\sin\omega$. Constraining the eccentricity in this way requires an EB with detected primary and secondary eclipses. This favors binaries with comparable surface temperatures and relatively small orbital separations. Of the 816 EBs in our rotation period catalog (see §3.3.1), 484 have eccentricity constraints using this method.

We stress that these eccentricities should only be regarded as approximations for the purposes of studying bulk trends with eccentricity. The KEBC does not include uncertainties on the eclipse timings and durations, and therefore we cannot propagate the uncertainties in our calculations. A fuller treatment of the uncertainties would require intensive modeling that is beyond the scope of this work. Ultimately this is of little concern, as we are most interested in differences in synchronization between clearly circular and clearly eccentric systems, rather than the exact dependence on eccentricity.

3.2.3 Kepler Light Curves

We analyzed *Kepler* quarters 0-17 light curves from Data Release 25. We used the Simple Aperture Photometry (SAP) fluxes, detrended by the *Kepler* mission pipeline Presearch Data Conditioning (PDC). Cadences were excluded if they had `SAP_QUALITY` flag values of 128, indicating that a cosmic ray was found and corrected in the optimal aperture, or 2048, indicating that an impulsive outlier was removed before detrending (Thompson et al., 2016). For each quarter, we subtracted and then divided by the median flux value. The resulting dimensionless relative flux values are useful for intercomparing EB light curves, and are necessary for the autocorrelation function method to measure rotation periods (see §3.3.2).

The current PDC pipeline suppresses stellar variability at periods longer than approximately 20 days (Gilliland et al., 2015). There is a tradeoff between using undetrended SAP and detrended PDC light curves. By using the PDC light curves, we are more confident that the rotation periods we measure are not due to instrumental artifacts, but we may detect fewer slowly rotating stars. If we had used the undetrended SAP light curves, we may have found more slow rotators, but would be less sure that they were astrophysical in origin. Even without the pipeline suppression, slow rotators are intrinsically more difficult to detect, because the amplitude of their starspot modulations is lower (McQuillan et al., 2014). Given these limitations, our synchronization study is primarily focused on EBs with rotation periods less than 20 days.

3.3 Classification and Rotation Period Analysis

Our analysis involved two steps. First, we visually inspected the light curves to classify EBs with starspot modulations, as well as other types of EBs. Next, we measured the rotation periods for EBs with starspot modulations.

3.3.1 Light Curve Classification

Light curves were divided into six categories based on the morphology of their out-of-eclipse variability. Examples are shown in Figure 3.1.

1. There are 816 EBs with starspot modulations (SP). These appear as roughly sinusoidal variations, and are due to periodic dips in brightness as spots (or spot groups) rotate into and out of view. The key feature of starspot modulation we used for classification is the phase and amplitude evolution of the modulations. An example of this evolution is shown in the top panel of Figure 3.1. Between days 910 and 945, the out-of-eclipse variability has two humps. Between days 945 and 965, the smaller hump disappears, and the amplitude of the larger hump increases. This is due to the combination of differential rotation of the star, and the formation and dissipation of starspots. For a schematic of how differential rotation and spot evolution change the light curve appearance, see Figure 4 of Davenport et al. (2015).

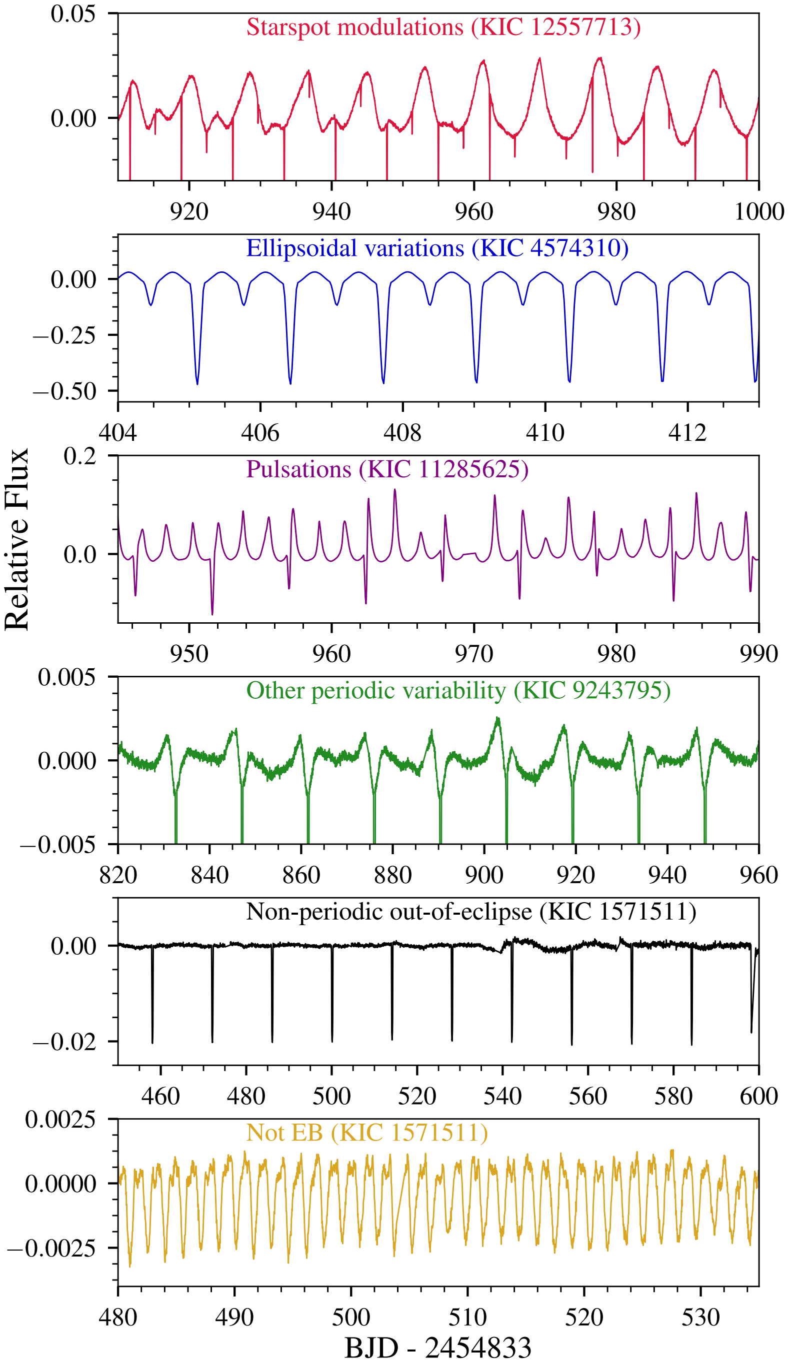

Figure 3.1: Example light curves for the six classification types.

2. There are 779 EBs with ellipsoidal variations (EV). Ellipsoidal variations are due to the changing apparent cross section of the tidally distorted stars as they orbit each other. The stars have the largest cross sections at quadrature, resulting in two peaks in the light curve halfway between the primary and secondary eclipse. Unlike starspot modulations, ellipsoidal variations do not evolve over the 4 year observation baseline of *Kepler*.

   This category includes EBs with well-defined eclipses such as in the second panel of Figure 3.1, and contact binaries without well-defined eclipses. Most EBs with ellipsoidal variations are likely circularized and synchronized due to the strong tidal forces at their small separations. However, ellipsoidal variations do not constitute a direct measurement of stellar rotation, and are not the focus of this work.

3. There are 27 EBs with δ Scuti and γ Doradus pulsations (PU) and 21 with possible pulsations (PUX). An example is shown in the third panel of Figure 3.1. In Table 3.3.1, we note 12 EBs that are not listed as pulsators in the KEBC or the literature.

4. There are 27 EBs with other periodic out-of-eclipse variability that is not due to one of the above phenomena (OT). Some of these may be previously unidentified heartbeat stars, such as the example shown in the fourth panel of Figure 3.1.

5. There are 598 EBs without any clear periodic out-of-eclipse variability (NP), like that in the fifth panel of Figure 3.1. Many of these have essentially flat out-of-eclipse light curves, or long term, smooth variations due to instrumental effects. Some EBs in this category have low level variability that may be due to starspots, but were too ambiguous to include in the starspot modulation category.

6. There are 10 targets where starspot modulations appear to have been mistaken for ellipsoidal variations, an example of which is shown in the bottom panel of Figure 3.1. Due to the lack of clear eclipses, these targets may not be EBs.

Table 3.1. Previously Unidentified Pulsators

Likely Pulsators (PU)
KIC 10549576
KIC 11724091
KIC 11817750
Candidate Pulsators (PUX)
KIC 5565486
KIC 6063448
KIC 6109688
KIC 6145939
KIC 6147122
KIC 9552608
KIC 11923819
KIC 12106934
KIC 12167361

3.3.2 Measurement of Rotation Periods

We measured rotation periods for the 816 EBs with starspot modulations using the following procedure. First, we linearly interpolated over eclipses, and then measured initial rotation periods using the autocorrelation function (ACF, see McQuillan et al. 2013). The ACF is not very sensitive to multiple rotation period signals in the light curve that may originate from the two separate stars in an EB (Rappaport et al., 2014), or from differential rotation on one star (RG15). We therefore searched for multiple rotation periods using the Lomb-Scargle periodogram (Lomb, 1976; Scargle, 1982), with the ACF-based periods serving as a validation.

Interpolation over Eclipses

Eclipses are a source of contamination and were removed prior to measuring rotation periods. We linearly interpolated over windows around the eclipses that were equal to 1.5 times the eclipse widths listed in the KEBC. This larger window ensures that the eclipses are entirely removed. Interpolating over the eclipses does not adversely affect the rotation period measurements, because the EBs with starspot modulations typically have small eclipse widths; more than 83% have total eclipse widths (primary plus secondary) less than 10% of the total orbit.

Initial Periods from the Autocorrelation Function

The ACF computes the self-similarity of a light curve at different time lags. Periodically varying light curves have a peak ACF value at the time lag corresponding to that period. We identify the peak in the ACF using the procedure of McQuillan et al. (2013). The ACF was first smoothed using a Gaussian filter with a kernel standard deviation of 18 time lags and window size of 56 time lags. In general, the first peak in the ACF is the highest, and corresponds to the stellar rotation period. However, if there are spots on opposite hemispheres, there will be a lower ACF peak at half of the rotation period. We manually

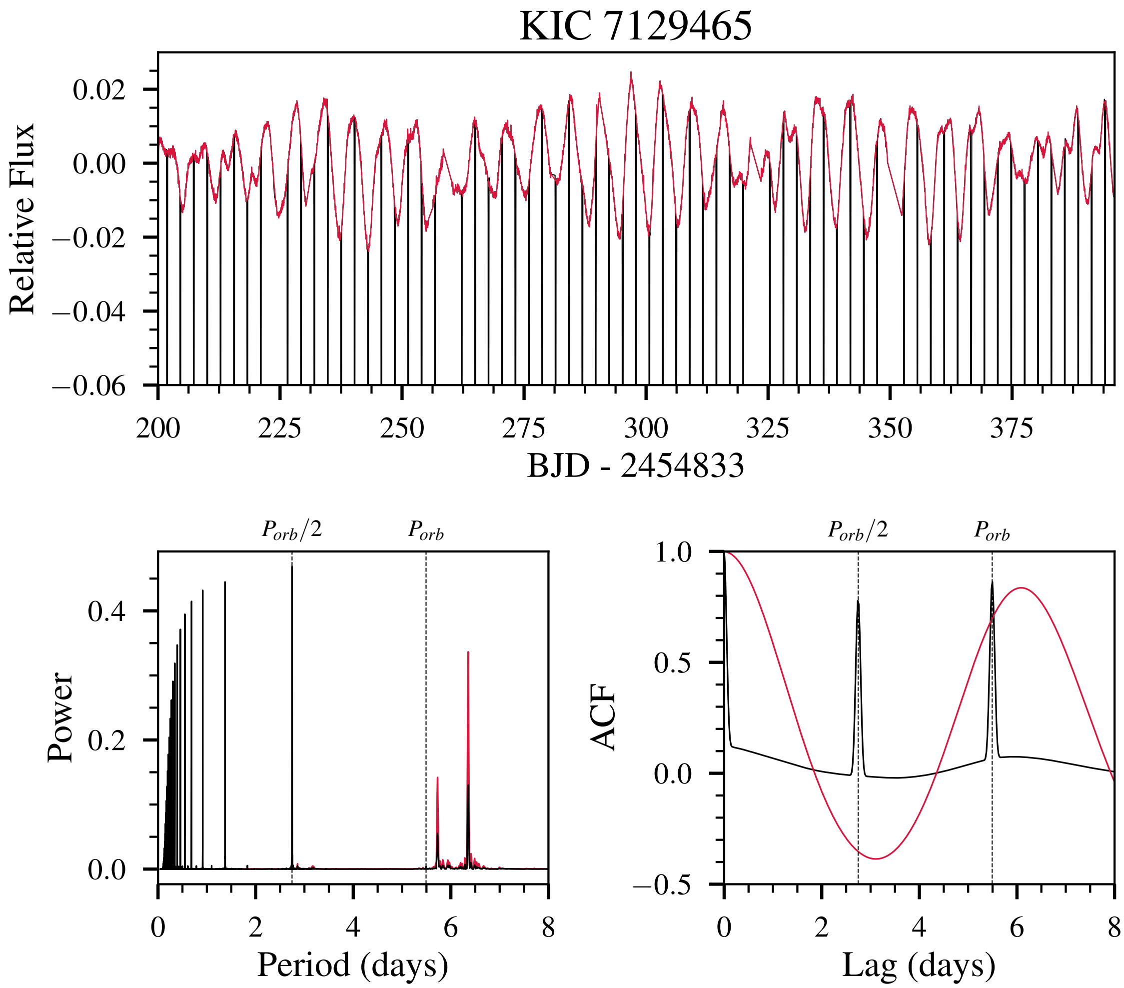

Figure 3.2: Eclipse removal and rotation period measurements for the representative EB KIC 7129465. Top panel: A 200 day segment of the full 1460 day light curve. The out-of-eclipse light curve is plotted in red, while eclipses are plotted in black. The flux range has been truncated to focus on the out-of-eclipse variability. Bottom left panel: Lomb-Scargle periodograms for the full (black), and out-of-eclipse (red) light curves. The black periodogram has been multiplied by a factor of five for clarity. Bottom right panel: Autocorrelation functions for the full (black) and out-of-eclipse (red) light curves.

corrected such instances, as well as cases where peaks at longer time lags were erroneously identified by the automated code.

Figure 3.2 demonstrates the rotation period measurement for the 5.5 day orbital period EB KIC 7129465. There is a dramatic difference in the ACFs before and after eclipse removal. The black ACF (with eclipses) has sharp peaks at the half and full orbital periods due to the strong periodic signal of the eclipses. In contrast, the red ACF (without eclipses) has a wider peak at 6.1 days, somewhat longer than the orbital period. The shape of the red ACF is similar to those for single stars with starspot modulations (McQuillan et al., 2013). This indicates that the eclipses have been successfully removed, and that the rotation period is longer than the orbital period, in this case.

As further validation of our rotation periods, we compare the ACF peak heights of EBs with starspot modulations to the EBs without periodic out-of-eclipse variability. Following McQuillan et al. (2013), we define the peak height as the height of the ACF peak relative to the adjacent minima. Unlike the absolute height, the relative height is less susceptible to systematic effects in the light curve such as long term trends. The ACF has values between -1 and 1, so the relative peak height has values between 0 and 2.

Figure 3.3 shows the distribution of ACF relative peak heights for EBs with starspot modulations and no periodic out-of-eclipse variability. The two distributions are clearly separated. 84% of the starspot modulation category have peak heights greater than 0.5, compared to only 24% for the non-periodic category. This provides validation that the EBs classified as having starspot modulations do exhibit significant out-of-eclipse periodicity.

Multiple Rotation Periods from the Periodogram

The bottom left panel of Figure 3.2 shows periodograms for the full light curve (black) and after eclipses have been removed (red). The black periodogram has peaks at the half orbital period and lower harmonics, as is typical for EB periodograms. There are also two smaller peaks at 5.7 and 6.4 days, again somewhat longer than the orbital period. When the eclipses are removed (red periodogram), the orbital period harmonic peaks essentially disappear, and

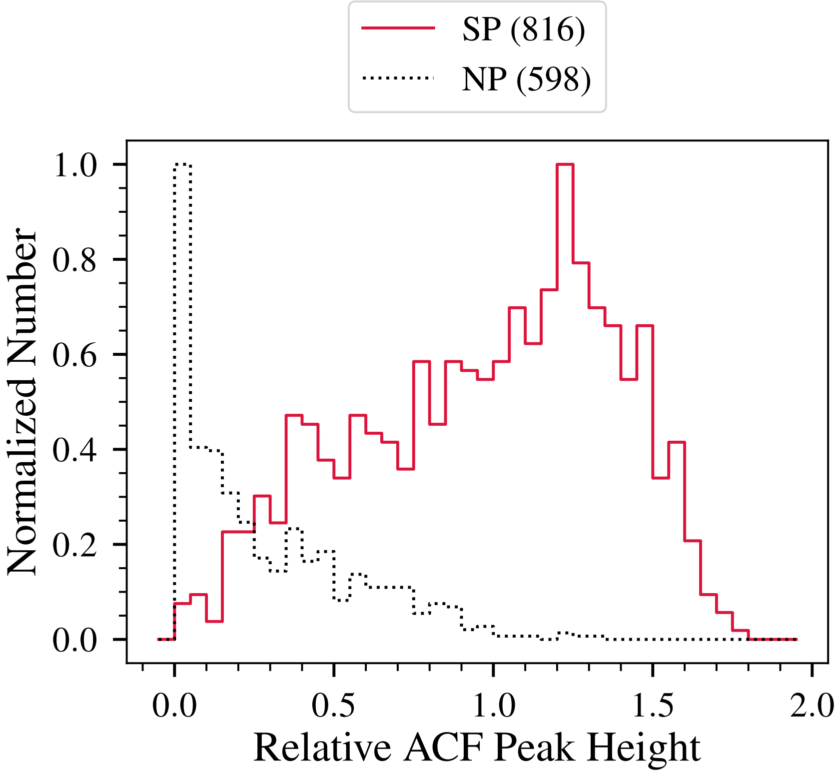

Figure 3.3: Distributions of relative ACF peak heights for EBs with starspot modulations (SP, solid red line) and non-periodic out of eclipse variability (dotted black line). The histograms are normalized to their maximum values, and the number of EBs in each category are listed in parentheses. The likely starspot systems have the highest peaks, corresponding a strong periodic signal.

only the peaks at 5.7 and 6.4 days remain. Importantly, the locations of the peaks do not change, meaning that the removal of the eclipses cannot be responsible for the peaks.

As discussed below, many of the EBs in our sample have two peaks in their periodograms after eclipses have been removed. This highlights the importance of using both the ACF and the periodogram. Had we only relied on the ACF, we would have missed information in the light curves. Meanwhile, the ACF provides validation that the peaks are due to starspot modulations.

We identified multiple rotation periods adapting the procedures of Rappaport et al. (2014) and RG15. This involved generating periodograms for each EB on a uniform frequency grid using the Python package `gatspy` (VanderPlas & Ivezić, 2015; VanderPlas, 2016). The grid had frequency bin widths of 5.7×10^{-5} day^{-1}, which resulted in a very oversampled periodogram, as was desired. We then smoothed each periodogram using a Gaussian filter with a kernel standard deviation of 30 frequency bins and a window size of 120 bins.

We searched for peaks in the smoothed periodogram in a period range from 2/3 of the ACF rotation period up to 200 days. Next, we identified the two highest significant peaks in the smoothed periodogram. Peaks were defined as significant if their heights were at least 30% that of the highest peak. Lowering this threshold increases the possibility of finding multiple rotation periods, but also increases the possibility of finding spurious signals.

Next, we identified neighborhoods around the two peak groups in which we can search for subpeaks. The neighborhood is the frequency range between the local minima to the left and right of dominant peaks in the smoothed periodogram. Within each neighborhood, we applied the same threshold that significant subpeaks must be at least 30% as high as the highest subpeak in the group. We then selected the subpeaks with the largest frequency separation.

Figure 3.4 demonstrates our multiple peak-finding algorithm for four representative cases. In the case of KIC 7129465 (top left panel), there are groups of peaks at 5.71 and 6.41 days (0.175 and 0.156 day^{-1}), as discussed above. However, there is only one significant subpeak in each group. In the case of KIC 4751083 (upper right), there are two well separated peak groups, with two significant subpeaks in each group. In the case of KIC 2438061 (lower left), there is only one significant group of peaks, and there are two significant subpeaks in that group. Finally, in the case of KIC 2445975 (lower right), there is only one significant subpeak, and hence no detection of multiple rotation periods.

We define a conservative rotation period limit of 45 days. Robustly measuring longer period signals is difficult due to instrumental systematics that differ between *Kepler* quarters. Quarters are approximately 90 days long, and a cutoff of 45 days requires that we would see

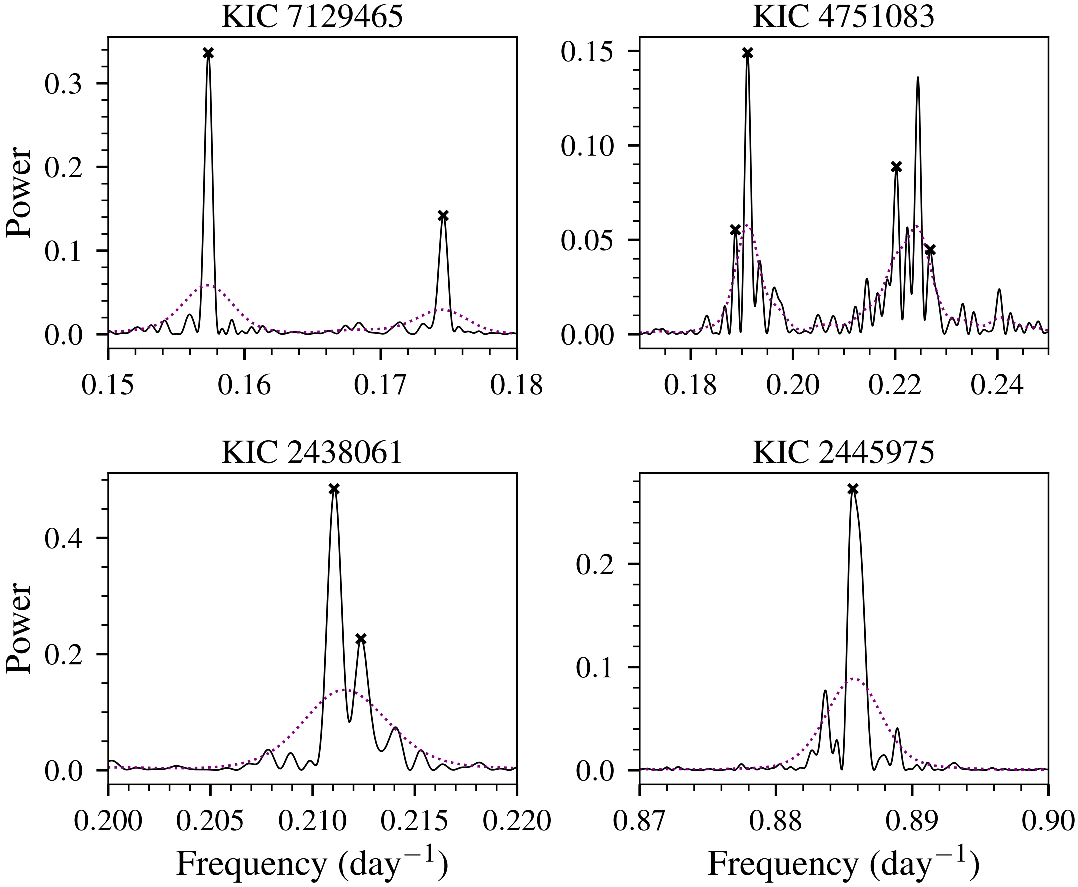

Figure 3.4: Examples of the routine to find multiple rotation periods in the Lomb-Scargle periodogram. The solid black curve shows the oversampled periodogram, while the dashed purple curve shows the periodogram smoothed with a Gaussian filter. The black crosses indicate the significant subpeaks within each group.

the rotation signal repeat twice in a single quarter. We do measure rotation periods longer than 45 days, but they should be treated with caution. This cutoff has a minimal effect on our synchronization analysis (§4.5), which is primarily focused on the one to twenty day rotation period range.

3.4 Tidal Synchronization

In this section, we give a brief overview of our rotation period catalog, and the orbital period distribution of the different EB categories. We then use the catalog to investigate the dependence of tidal synchronization on orbital period, eccentricity, stellar mass, and mass ratio.

3.4.1 Rotation Period Catalog

Table 3.2 lists a representative subset of entries in our rotation period catalog. The full catalog is available in the online supplement. For each EB, the table includes the orbital period and the visual classification. For EBs for which rotation periods were measured (category SP), the table lists the ACF rotation periods, ACF peak heights, as well as the periodogram periods and peak heights. ACF rotation periods and peak heights are listed for the nonperiodic out-of-eclipse variability (NP) category for validation purposes, but flagged "a" in the Notes column to indicate that they should not be used for tidal synchronization analysis. For 12 EBs in the SP category flagged with "b", P_{ACF} should not be used, however the periodogram periods are correct. The ACF detected a spurious signal due to systematic artifacts in the light curve.

Unless otherwise stated, the following analysis uses the minimum periodogram-based rotation period for each EB (column $P_{1,min}$ in Table 3.2). Assuming solar-like differential rotation, $P_{1,min}$ will be closest to the equatorial rotation period. This provides a consistent reference point for the differential rotation discussion below.

We also note that the conclusions presented below are the same when using the ACF-based periods, and so using the periodogram period does not bias our results. However, the periodogram based rotation periods provide more information than the ACF-based periods with regards to EBs with multiple rotation periods.

Table 3.2. EB Classifications and Rotation Periods - Representative Subset

KIC ID	P_{orb}	Class.	P_{ACF}	h_{acf}	$P_{1,min}$	$P_{1,max}$	$P_{2,min}$	$P_{2,max}$	$h_{1,min}$	$h_{1,max}$	$h_{2,min}$	$h_{2,max}$	Notes
2997455	1.130	SP	1.124	0.652	1.127	1.131			0.062	0.084			
2998124	28.598	NP	56.785	0.717									a
3003991	7.245	SP	9.563	0.493									
3097352	4.030	SP	27.871	0.435	3.957	3.989			0.012	0.012	0.005	0.005	b
3098194	30.477	SP	29.731	0.147	26.521	33.270			0.023	0.036			
3102000	57.060	SP	14.733	0.905	13.998	15.483			0.048	0.043			
3102024	13.783	SP	4.884	0.803									
3104113	0.847	EV											
3113266	0.996	NP	0.981	0.236									a
3114667	0.889	SP	0.879	0.626									
3115480	3.694	SP	3.617	1.198									
3119295	0.440	EV											
3120320	10.266	SP	13.261	0.782	12.473	13.670	14.389	14.617	0.028	0.032	0.031	0.043	
3122985	0.993	SP	1.471	1.416	1.453	1.465	1.497	1.504	0.020	0.043	0.092	0.056	
3124420	0.949	EV											
3127817	4.327	EV											
3127873	0.672	EV											
3128793	24.679	SP	66.307	0.986									
3218683	0.772	EV											
3221207	0.474	EV											

bP_{ACF} is incorrect due to systematic artifacts in the light curve.

Note. — A full version of the table is available in the online supplement.

[a] P_{ACF} and h_{ACF} for the NP (no periodic out-of-eclipse variability) category are for validation purposes only, and should not be used for tidal synchronization analysis.

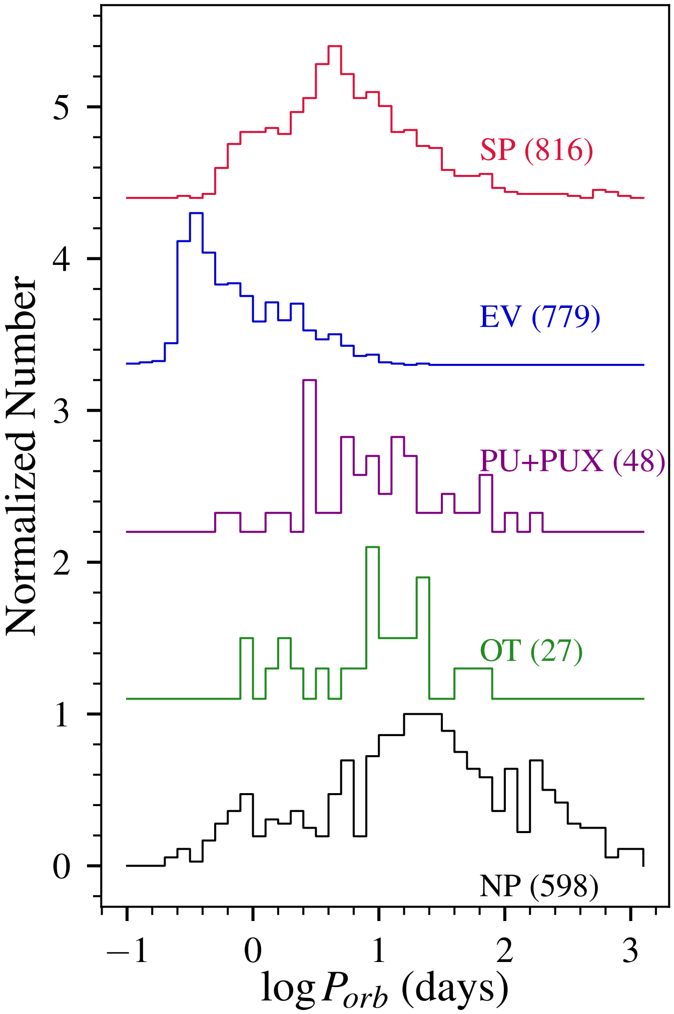

Figure 3.5: The distributions of orbital periods for the light curve visual classifications. From top to bottom: starspot modulations (SP), ellipsoidal variations (EV), likely and possible pulsators (PU and PUX), other out-of-eclipse variability (OT), and no periodic out-of-eclipse variability (NP). Each histogram has been normalized by its maximum value, and the histograms are vertically offset for clarity. The number of EBs in each class is indicated in parentheses.

3.4.2 Orbital Period Distribution of EB Categories

Figure 3.5 shows the distributions of orbital periods for the five true EB categories from §3.3.1, not including the last category (10 objects) where starspots may have been mistaken for ellipsoidal variations. The distributions show evidence of tidal interaction. Strong tidal forces at short orbital periods drive the ellipsoidal variations. Compared to the non-periodic category, EBs with starspot modulations favor shorter orbital periods where the stars are tidally spun up, resulting in stronger magnetic activity. The non-periodic systems are concentrated at longer orbital periods where the tidal forces are weaker. These EBs have not synchronized, so the stars are rotating more slowly and therefore do not have strong magnetic activity that produces detectable starspot modulations. The pulsation and other variability categories do not show a strong dependence on orbital period, because these processes are apparently independent of rotation and hence orbital period.

3.4.3 The Period Ratio Diagram

To measure the degree of synchronization for a given EB, we compute the *period ratio* P_{orb}/P_{rot}. This is equal to $\Omega_\star/n$, where $\Omega_\star$ is the rotational angular velocity of the star, and n is the mean orbital angular velocity. Synchronization occurs at $P_{orb}/P_{rot} = 1$, while $P_{orb}/P_{rot} > 1$ is supersynchronous, $P_{orb}/P_{rot} < 1$ is subsynchronous.

Figure 3.6 shows the period ratio diagram for the 816 EBs in the SP category. These EBs are divided into a main population, and three categories of outliers. The outliers are discussed below, before moving on to the main population.

Asynchronous Systems with Short Periods

Before investigating trends in synchronization, we identify 61 asynchronous systems with orbital periods less than 10 days that have a period ratio less than 0.6 or greater than 1.2. The outliers are listed in Table 5.1 (§ 5.5 of Chapter 5), and are divided into four categories.

1. There are 11 EBs where the rotation period is exactly twice or half of the orbital

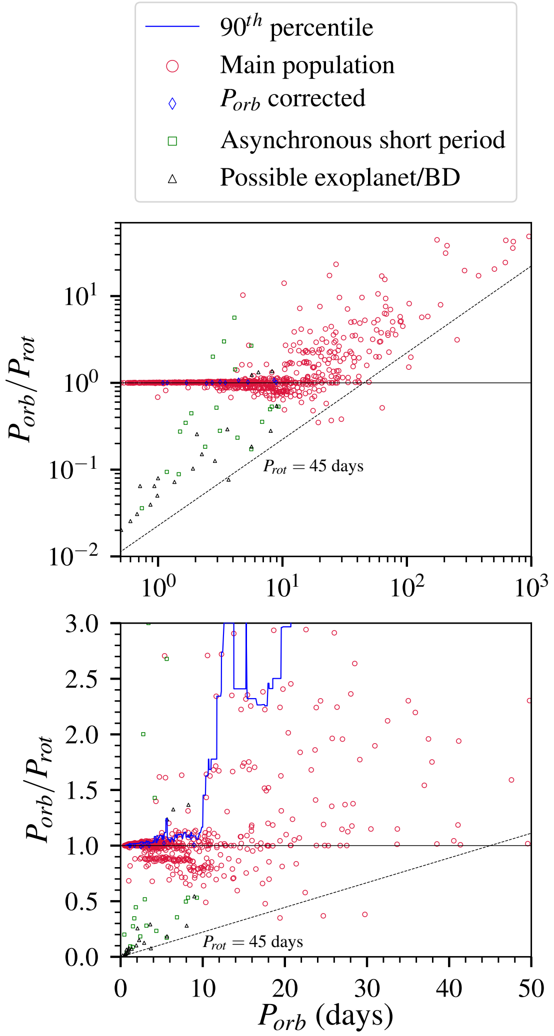

Figure 3.6: The distribution of period ratio versus orbital period for the EBs with starspot modulations. Likely non-EB outliers are indicated by black triangles, EBs with orbital period corrections are indicated by blue diamonds, and asynchronous short period EBs are indicated by green squares. The black horizontal line corresponds to synchronization at $P_{rot} = P_{orb}$, while the dashed diagonal line indicates conservative rotation period limit of 45 days. The blue curve indicates the running 90^{th} percentile. The bottom panel shows the region around synchronization in more detail.

period. We argue that these are not in fact outliers, but instead the KEBC orbital period is incorrect. This can occur because it is difficult to distinguish between a circular EB with only primary eclipses, and an EB with nearly equal primary and secondary eclipse depths at twice the period. Our rotation period measurement could be incorrect by a factor of two due to aliasing effects, but this is unlikely as we used the ACF for validation. We therefore corrected the orbital periods, moving these EBs into the synchronized population. They are indicated by blue diamonds in Figure 3.6.

2. There are 21 systems with unambiguous primary and secondary eclipses, meaning they are most likely EBs. These EBs may be asynchronous because they are young, or have a complex dynamical history. They are indicated by green squares in Figure 3.6 and are included in the synchronization analysis below.

3. There are 22 systems that are likely not EBs. They are indicated by black triangles in Figure 3.6, and are *not* included in the analysis below. We further divide these systems into two categories:

    (a) There are 12 systems with very low signal-to-noise primary eclipses and no secondary eclipses. They may be false positives because a close, stellar mass companion should have synchronized the binary.

    (b) There are 10 systems with unambiguous but shallow primary eclipses and no secondary eclipses. The occulting object may be a planet or brown dwarf, which is not massive enough to have synchronized the star.

    Of these 22 systems, Kolbl et al. (2015) found that KIC 7763269, KIC 9752973, KIC 10338279, and KIC 10857519 show evidence of a close stellar companion in their spectra. However, without multi-epoch radial velocities, it is unclear whether the spectral companion is responsible for the eclipses.

4. There are 7 EBs in this range ($P_{orb} < 10$ days and $0.6 < P_{orb}/P_{rot} < 1.2$) that appear to be pseudosynchronized, as discussed in §3.4.4.

Furthermore, it is possible that the starspot modulation we detected does not originate from the EB at all, and instead comes from a third star in the system, or an unrelated star at a small angular separation. All of these outlying systems are worthwhile targets for observational followup, especially those that are potentially young or have an interesting dynamical history. With a small number of radial velocity and/or adaptive optics observations, it would be straightforward to distinguish between the cases listed above.

3.4.4 Dependence on Orbital Period

Orbital period is arguably the most important quantity for tidal synchronization, as the synchronization timescale is predicted to increase with orbital period to the sixth power (Hut, 1981).

Synchronization and Differential Rotation Below 10 Days

As seen in Figure 3.6, EBs with orbital periods less than 2 days are nearly all synchronized. 94% of the sample has $0.92 < P_{orb}/P_{rot} < 1.2$. Between 2 and 10 days, the sample is divided into two clusters. The main cluster is centered slightly above the synchronization line, while the second cluster is centered around $P_{orb}/P_{rot} = 0.87$. 72% of EBs with orbital periods between 2 and 10 days have have $0.92 < P_{orb}/P_{rot} < 1.2$ (main cluster), while 15% have $0.84 < P_{orb}/P_{rot} < 0.92$ (subsynchronous cluster).

The subsynchronous rotation periods of the EBs is not an instrumental or numerical artifact. The subsynchronous peaks are present in the full light curve periodogram (black curve in lower left panel of Figure 3.2), meaning that interpolating over the eclipses cannot explain the subsynchronous rotation. Furthermore, the ACF-based rotation periods also have a subsynchronous cluster, so this cannot be an artifact of the periodogram. We therefore conclude that the subsynchronous signal is due to starspot modulations.

The cluster of subsynchronous EBs are an unexpected and intriguing result. To our knowledge, this phenomenon has not been observed previously. In §3.5, we demonstrate that the subsynchronous rotation is consistent with differential rotation. If the stars are tidally synchronized at the equator, then starspots at higher, slower rotating latitudes will make the measured rotation period subsynchronous.

A Transition to Eccentric, Pseudosynchronized EBs

Beyond roughly 10 days there is a decrease in the number of EBs centered around the synchronization line. This coincides with an increase in the number of supersynchronous EBs ($P_{orb}/P_{rot} > 1.2$).

To quantify this transition, we compute the 90th percentile of the period ratio distribution in a running manner. For each EB, we take the other 29 EBs with the nearest orbital periods to calculate the percentile. The asynchronous non-EB systems (§3.4.3) were excluded. A larger value of the 90th percentile indicates that the supersynchronous tail of the distribution is more significant.

The running 90th percentile is plotted as a thick black curve in the bottom panel of Figure 3.6. At 10 days there is a rapid increase in the 90th percentile. Although there are some supersynchronous EBs at shorter periods, they are a small fraction of the sample, whereas at 10 days the fraction of supersynchronous EBs increases dramatically at the expense of synchronized EBs.

We therefore divide the period ratio distribution into two main populations. Below 10 days, the bulk of EBs are synchronized, with a subpopulation of subsynchronous rotators. Above 10 days, there is a significant increase in the number of supersynchronous rotators. As we demonstrate below, this transition occurs because a large fraction of the EB orbits are eccentric, and those EBs are pseudosynchronized.

Figure 3.7 shows the same distribution as Figure 3.6, but the points are colored according to eccentricity, measured as described in §3.2.2. There is a clear division in Figure 3.7 based on eccentricity. Most of the EBs with small eccentricities (yellow circles) have orbital periods less than 10 days and are concentrated near synchronization. In contrast, most of the EBs with larger eccentricities (dark green and purple circles) have orbital periods greater than 10 days, and are supersynchronous.

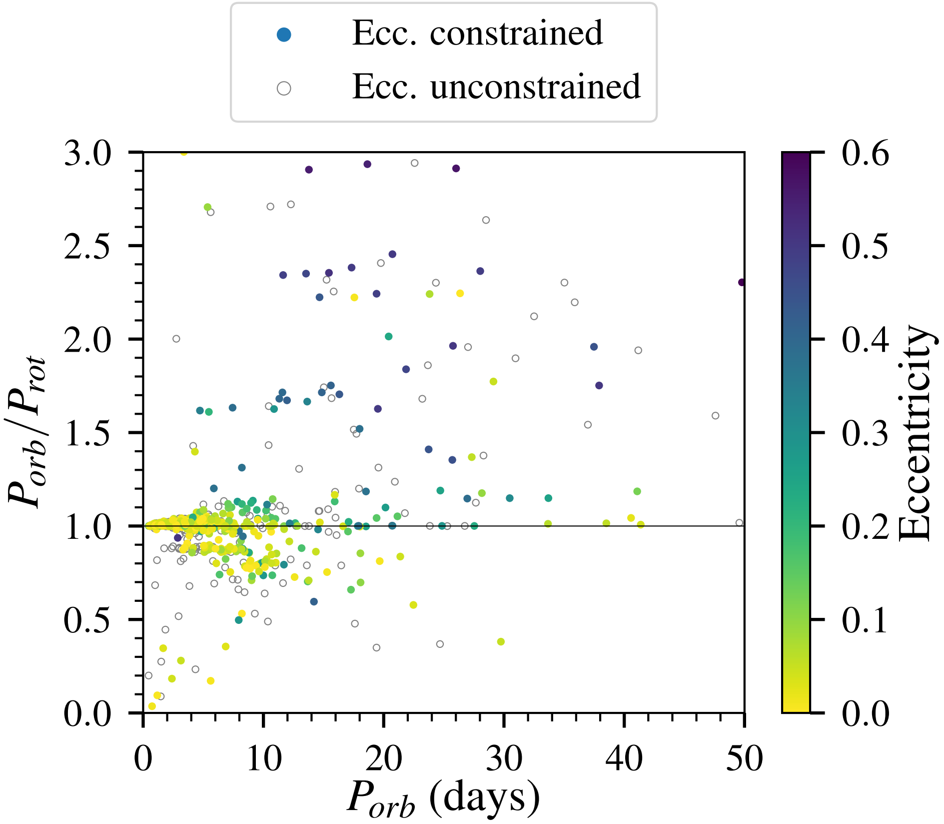

Figure 3.7: Distribution of period ratio versus orbital period for EBs with starspot modulations. Points are colored according to eccentricity. EBs without eccentricity constraints are indicated by open grey circles.

The distribution of EBs without eccentricity constraints overlaps those with constraints. If the eccentricities were measured, it is reasonable to assume that they would follow the same trends described above. Alternatively, some supersynchronous EBs without eccentricity constraints may not have tidally interacted. The EB may have a low mass ratio, as is consistent with a lack of secondary eclipses, which are required to measure eccentricity.

Pseudosynchronization can explain the slightly supersynchronous rotation of the main cluster of EBs with periods less than ten days. These slightly supersynchronous EBs may have eccentricities that are too small to measure by our approximation. In that case they would technically be pseudosynchronized, but only slightly supersynchronous due to the small eccentricity. Consistent with this scenario, the upper right corner of the cluster has the largest eccentricities (light green points), and are also the most supersynchronous. This is unlikely to be an artifact of the periodogram analysis, because the ACF-based rotation periods are also slightly supersynchronous.

Further evidence for pseudosynchronization is found in the distribution of the period ratio versus eccentricity, shown in Figure 3.8. The eccentric EBs appear to be pseudosynchronized, but are below the model prediction of Hut (1981, Eq. 42) by up to 50%. Of the four EBs in our sample with eccentricity measurements by Kjurkchieva et al. (2016) and Kjurkchieva & Vasileva (2018), three agree to within 5%, and one we overestimate by 26%. In §3.5, we argue that this may be due to differential rotation. Alternatively, the model may underpredict the pseudosynchronization period

Zahn & Bouchet (1989) predicted the existence of a cutoff orbital period for circularization between 7.2 and 8.5 days for stars with masses between 0.5 and 1.5 $M_{\odot}$. The cutoff is determined by the maximum orbital period at which the extended pre-main sequence binaries can circularize. When the stars begin to contract onto the main sequence, the rotation rate increases and becomes supersynchronous, but the orbit remains circular. Binaries that do not circularize on the pre-main sequence slowly circularize during the main sequence phase. Meibom & Mathieu (2005) report a tidal circularization period of $10.3^{+1.5}_{-3.1}$ days based on data for 50 nearby solar-type binaries from Duquennoy & Mayor (1991). This is in excellent agreement with the rapid increase in eccentric, supersynchronous EBs near 10 days.

Previous studies support the existence of a transition period for pseudosynchronization. Mazeh (2008) compiled data for eight pre-main sequence binaries from Marilli et al. (2007) and six binaries in young clusters from Meibom et al. (2006). Orbital parameters were

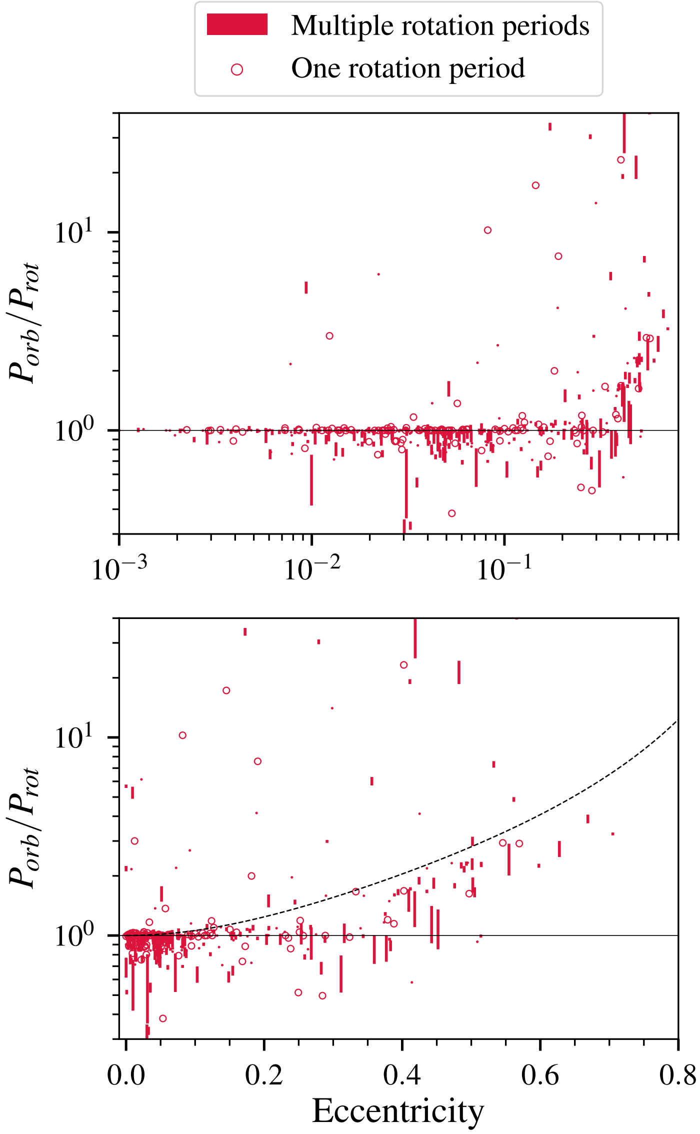

Figure 3.8: The distribution of period ratio versus eccentricity for EBs with starspot modulations. Vertical bars indicate the range of rotation periods measured, while open circles indicate EBs with only one rotation period measurement. The solid line corresponds to synchronization, while the dashed curve shows the predicted value of the period ratio from Hut (1981) for pseudosynchronization.

determined from radial velocities, and rotation periods were determined from starspot modulations. Mazeh finds a transition period between 8 and 10 days from circular, synchronous binaries to eccentric, supersynchronous binaries, in excellent agreement with our result.

Of the seven binaries that are eccentric and supersynchronous in Mazeh's sample, the two most eccentric binaries are rotating slower than the predicted pseudosynchronization period, while the other five are rotating faster than predicted. This is in contrast to our sample, where the majority of eccentric binaries are rotating slower than predicted, with the caveat of differential rotation discussed previously. Mazeh argues that the stars in the compiled sample are too young to have achieved pseudosynchronization, and that an older population of binaries would show a greater degree of pseudosynchronization. The latter appears to have occurred for our sample of Milky Way field binaries.

It is possible that some EBs are in a spin-orbit resonance. Unlike planets such as Mercury, stars do not have a fixed shape that would lead to a resonance. However, the existence of eccentric, supersynchronous EBs leaves open the possibility for coupling with the convective motions or internal pressure and gravity modes (Burkart et al., 2014). There is no obvious clustering of EBs near the 2:1 or 3:2 resonances ($P_{orb}/P_{rot} = 2$ and 1.5), however there is some suggestion of clusters near $P_{orb}/P_{rot} = 1.6$ and 2.3. The nearest, low integer ratio resonances are 5:3 and 7:3, although we hesitate to draw any conclusions given the small number of EBs in this range.

Behavior at Longer Periods

So far, we have focused on eccentric, pseudosynchronized binaries. However, Figure 3.7 also contains some EBs with small eccentricities and orbital periods greater than 10 days that are synchronized or nearly synchronized. This raises the question of to what extent circularization and synchronization continue during the main sequence phase. The EBs in our sample are part of the Milky Way field population. They should typically be at least a few Gyr old, and therefore have had a long main sequence phase during which tidal interaction could take place.

While old binaries are circularized at longer periods than young binaries, the difference is only about a factor of two. Latham et al. (2002) reported orbital solutions for 171 high proper motion binaries, which are likely members of the halo. For this sample, Meibom & Mathieu (2005) found a circularization period of $15.6^{+2.3}_{-3.2}$ days. Thus even for the oldest main sequence binaries in the Galaxy, we should not expect tidal circularization to have reached beyond ∼20 days.

Our results support this conclusion, in that we observe very few synchronized EBs with small eccentricities and orbital periods longer than 10 days. Five notable exceptions seen in Figure 3.7 are synchronized and have nearly circular orbits between 32 and 50 days. These are KIC 3955867, KIC 4569590, KIC 5308778, KIC 7133286, and KIC 8435232. They have flat-bottomed primary and secondary eclipses, which we interpret as containing a main sequence and evolved star. If one of the stars is evolved, its larger radius would allow for tidal circularization and synchronization at longer orbital periods than on the main sequence.

Beyond 30 days, there are very few synchronized EBs (except the possibly evolved stars), and only a handful of possibly pseudosynchronized EBs. This is consistent with the expectation that tidal interaction decreases rapidly with increasing orbital period.

3.4.5 Dependence on Stellar Mass (Color)

We now investigate the dependence of tidal synchronization on stellar mass. For a given semimajor axis, the synchronization timescale decreases with stellar radius to the sixth power (Hut, 1981). We therefore expect that EBs with more massive primaries (larger radii) should be synchronized at longer periods. However, the timescale also depends on other factors, including the mass ratio (see §3.4.6) and initial eccentricity. Furthermore, the efficiency of the tidal dissipation mechanism likely depends on the thickness of the convective envelope, which increases with decreasing mass.

Photometric colors are the only mass estimates available for the entire sample. In what follows, we assume that the EBs contain main sequence stars (with the exception of the five possibly evolved stars noted above), and that $g - K$ colors from the *Kepler* Input Catalog

Table 3.3. Spectral Types of Rotation Period Catalog

Sp. Type	$g-K$	Number	Structure
A	< 0.8	5	Radiative envelope
F	0.8 - 1.5	122	Small convective envelope
G	1.5 - 2.3	428	Medium convective envelope
K	2.3 - 4.5	181	Medium convective envelope
M0 - M4	4.5 - 6.2	8	Large convective envelope

Note. — $g-K$ colors are taken from Covey et al. (2007) for dwarfs. 8 EBs do not have $g-K$ values, and 64 do not have $E(B-V)$ values listed in the Kepler Input Catalog, and so were not assigned spectral types.

(Brown et al., 2011) are indicative of the mass of the primary star. As a conceptual tool, Table 3.3 divides the sample into spectral types A through M, using the main sequence color relations from Covey et al. (2007). Prior to assigning spectral types, we corrected for interstellar reddening using the $E(B-V)$ values in the Kepler Input Catalog. We stress that these spectral types are intended as approximations, given the limited mass information available for most of the sample.

Figure 3.9 shows the distribution of orbital periods versus dereddened $g-K$ color. Over half (57%) of the EBs with A and F primaries have ellipsoidal variations. A and F stars are not expected to have starspots, which would leave ellipsoidal variations as the dominant source of out-of-eclipse variability. For the cluster of short period ellipsoidal variables, there is a trend of decreasing P_{orb} with increasing $g-K$ values, which we discuss in §3.6.2.

Nearly all EBs (90%) have F, G and K primaries, reflecting the selection of solar-like

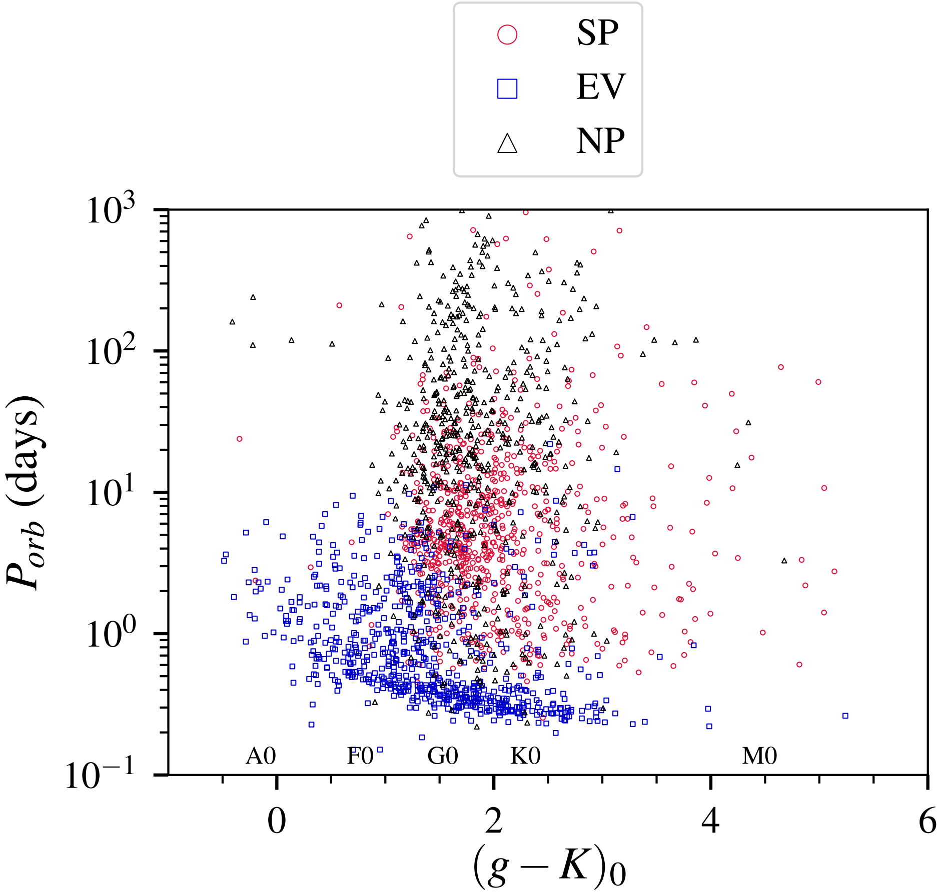

Figure 3.9: The distribution of orbital period versus dereddened $g-K$ color for EBs with starspot modulations (red circles), ellipsoidal variations (blue squares), and non-periodic out-of-eclipse variability (black triangles). Spectral types from Covey et al. (2007) are given for reference.

stars for the *Kepler* target list. This selection effect is beneficial in the sense that it greatly increases the number rotation period measurements for primaries with convective envelopes, whereas most previous observational studies of synchronization focused on primaries with radiative envelope.

Using the above color limits, the rotation period catalog only contains no fully convective primaries (later than M4), and five primaries with radiative envelopes. These numbers are insufficient to draw any conclusions about the tidal synchronization changes in the radiative envelope and fully convective regimes. We therefore concentrate on the differences between F, G and K primaries.

Figure 3.10 shows the distributions of period ratio for three different orbital period ranges: $P_{orb} \leq 2$ days, $2 < P_{orb} \leq 10$, $P_{orb} > 10$, with separate histograms for F, G, and K primaries. Our results indicate that there is no obvious difference in the period ratio distribution over the relatively narrow mass and radius range spanned by F, G, and K primaries. Thus primary mass does not appear to be a strong factor in the tidal synchronization of the F, G, and K primaries in our sample.

3.4.6 Dependence on Mass Ratio

Given the above results for primary mass, we now investigate the dependence of tidal synchronization on mass ratio, defined as M_{sec}/M_{pri}. The mass ratio has a maximum value of one for equal mass binaries, and approaches zero for very unequal masses. The tidal synchronization timescale is predicted to decrease with increasing mass ratio (Hut, 1981), so that EBs with nearly equal mass ratios should be synchronized at longer periods than EBs with low mass ratios, keeping all other factors constant.

We create two subsamples of EBs with the greatest difference in mass ratio. The first subsample has primary eclipse depths $\delta_{pri} < 0.1$, and no detected secondary eclipses, indicating a small companion mass relative to the primary. The second subsample has ratios of primary to secondary eclipse depth $\delta_{sec}/\delta_{pri} > 0.7$, indicating a roughly equal mass companion.

Figure 3.11 shows the distributions of period ratio for $P_{orb} \leq 2$ days, $2 < P_{orb} \leq 10$ days, and $P_{orb} > 10$ days , with separate histograms for the small and roughly equal mass ratio subsamples. Most EBs with orbital periods less than 2 days are synchronized. This is true regardless of the mass ratio, although there are some subsynchronous EBs with low mass ratios as discussed in §3.4.3 (small peak near zero in top yellow histogram). In the 2 to 10 day orbital period range, the low mass ratio EBs have a higher relative number of ∼13%

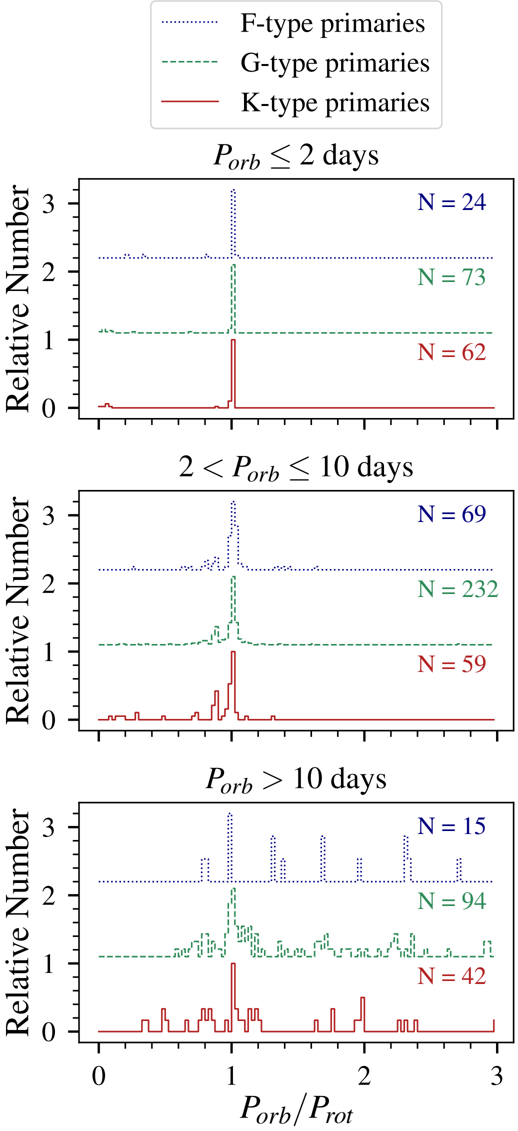

Figure 3.10: From top panel to bottom: the distributions of period ratio for $P_{orb} \leq 2$ days (top panel), $2 < P_{orb} \leq 10$ days (middle), and $P_{orb} > 10$ days (bottom). EBs with F-, G-, and K-type primaries are denoted by dotted blue, dashed green and solid red lines, respectively. Each histogram is normalized to its maximum value and vertically offset for clarity. The number of EBs in each histogram is listed.

subsynchronous EBs compared to the equal mass ratio subsample. At orbital periods longer than 10 days, the equal mass ratio subsample is somewhat more synchronized than the low mass ratio subsample, with 44% of the equal mass ratio subsample having rotation periods within 20% of the orbital period, compared to 22% for low mass ratio EBs.

It appears that synchronization has a somewhat stronger dependence on mass ratio than on the mass of the primary. However, the mass ratio of our sample spans a relatively narrow range from 1 to roughly 0.1, because the companions are likely stars. Some systems may have substellar companions and be asynchronous (§3.4.3), suggesting that mass ratio becomes more important in the very small mass ratio regime.

3.5 Differential Rotation

As was noted repeatedly in the previous section, there is a population of subsynchronous EBs with orbital periods between two and ten days. Additionally, there is a population of eccentric EBs that are rotating supersynchronously, as is consistent with pseudosynchronization, but that are rotating up to 50% slower than predicted by the model of Hut (1981).

In this section, we argue that both of these populations can be explained by differential rotation. We first examine the differential rotation measurements of the EBs, and conclude that they are consistent with single stars. Then we demonstrate how differential rotation explains the observed subsynchronous rotation.

3.5.1 Comparison to Single Stars

Of the 816 stars with starspot modulations, 206 had two periodogram peak groups, while 422 had one peak group. The remaining 188 only had a single significant peak, and hence do not show evidence of multiple rotation periods.

Following RG15, we express differential rotation in two ways. Absolute shear $d\Omega = 2\pi(1/P_{min} - 1/P_{max})$ measures the difference in rotational frequency between two latitudes in radians per day. P_{max} and P_{min} are the maximum and minimum rotation periods identified in §3.3.2. On a star with $d\Omega = 0.05$ rad/day, the slower rotating latitude would lag the

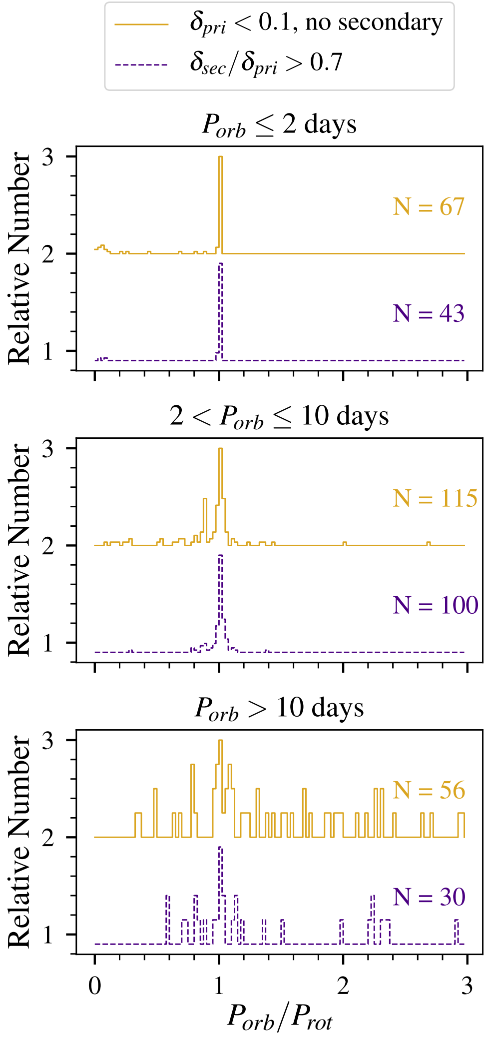

Figure 3.11: The dependence of synchronization on the mass ratio. The distribution of the period ratio is shown for three orbital period ranges: $P_{orb} \leq 2$ days (top panel), $2 < P_{orb} \leq 10$ days (middle), and $P_{orb} > 10$ days (bottom). The solid yellow histograms are for EBs with primary eclipse depths less than 0.1, and no secondary eclipses. This indicates a small mass ratio. The dashed purple histograms are for EBs with secondary-to-primary eclipse depths ratios greater than 0.7, indicating a roughly equal mass ratio.

faster latitude by 0.05 rad = 2.86° after one day. This quantity is measured directly from the frequency difference in the periodogram peaks.

Relative shear is defined as $\alpha = (P_{max} - P_{min})/P_{max}$. This is equal to the difference in rotation period between the poles and equator relative to the poles, and can take values between zero and one. Relative shear is a more intuitive quantity to understand the subsynchronous rotation scenario in §3.5.2. Our differential rotation measurements are lower limits, because the starspots that trace rotation may not be exactly on the equators and poles.

The top and bottom panels of Figure 3.12 show the distribution of absolute and relative shear versus the minimum rotation period measured for each EB. For comparison, we show the single star sample of RG15 with $T_{eff} < 6300$ K.

In general, our sample overlaps with the RG15 sample. The sequence of blue triangles below the RG15 distribution is most likely due to differences between our periodogram analyses. We therefore conclude that the vast majority of the multiple rotation period results are consistent with differential rotation of starspots detected on the only the primary star. Notable exceptions are KIC 10068919, KIC 11147460, and KIC 11231334, which have shear measurements above the RG15 sample, and are the best candidates for having periods originating from the two separate stars in the EB.

It is not surprising that we only detect starspot modulations from the primary, given the steepness of the stellar mass-luminosity relation. The starspot modulations from the more massive companion will dominate the light curve, except in the rare case of very nearly equal mass stars. Only 9% of EBs in our sample have $\delta_{sec}/\delta_{pri} > 0.9$, where we would most likely expect to detect both stars. Furthermore, the slightly subsynchronous population of EBs is more pronounced among EBs with low mass ratios (middle panel of Figure 3.11). If the subsynchronous population is due to differential rotation, as we argue below, then the low mass ratio further supports that the signal originates from the primary star only.

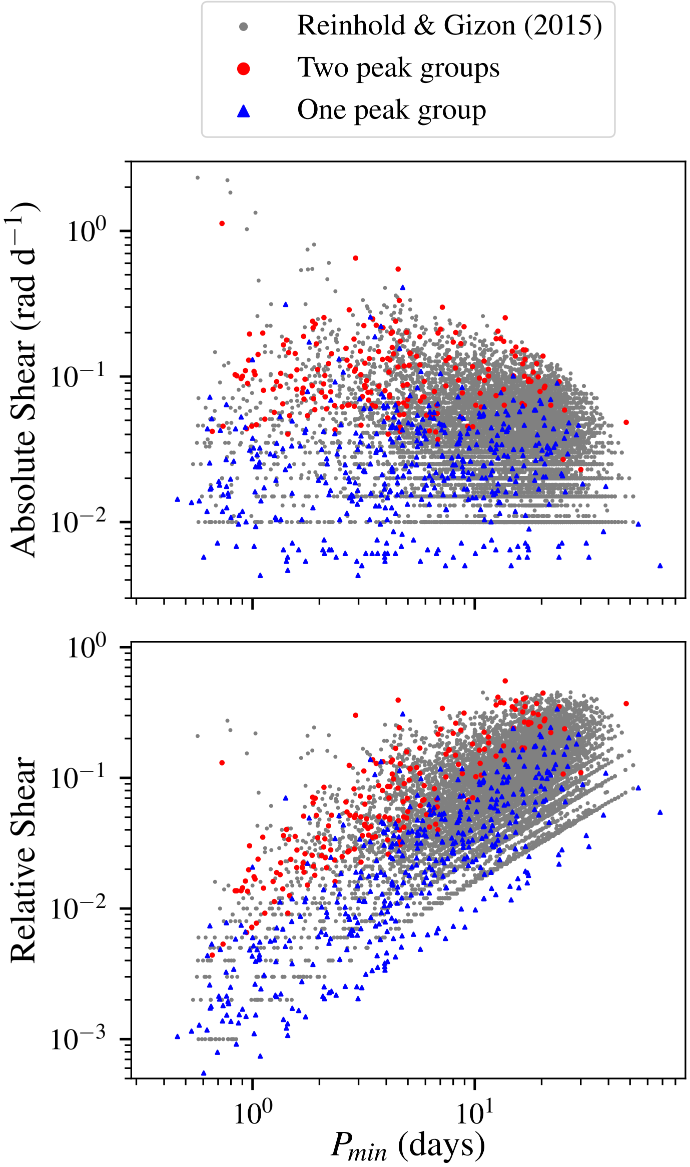

Figure 3.12: Absolute shear $d\Omega$ (top panel) and relative shear α (bottom panel) versus the minimum periodogram rotation period. EBs with two groups of peaks are shown as red circles, and EBs with one peak group as blue triangles. For comparison, the single star sample of Reinhold & Gizon (2015) for $T_{eff} < 6300$ K is shown as grey circles.

3.5.2 Subsynchronous Rotation

Given the above results, we will assume that we are detecting differential rotation on the primary star, and now demonstrate how differential rotation explains the subsynchronous population of EBs. To help illustrate this, Figure 3.13 shows the period ratio diagram, with the range of rotation periods due to differential rotation indicated by vertical lines.

Below 10 days, the EBs are synchronized to the rotation period at the equator. As the orbital period increases, so does the rotation period. As is shown in Figure 3.12, there is a larger amount of relative shear at longer rotation periods. Because of this, the measured values of the period ratio decrease with orbital period. We can then envision an envelope in the P_{orb}/P_{rot}-P_{orb} space that stars can occupy. It extends from the synchronization line (or slightly above), and expands downwards. The lower edge of the envelope is dictated by the maximum amount of relative shear possible at a given rotation period, which appears to be roughly 15 to 20%. Stars could then lie anywhere in this envelope depending on the distribution of their starspots.

In this scenario, EBs with no detected differential rotation (black circles in Figure 3.13) have primaries with starspots that exist only in a narrow latitude range. However, the spots could occur at any latitude, which explains why the black points are distributed throughout the envelope. The single periodogram peak group category (blue vertical lines) have spots in a relatively narrow latitude range, but some differential rotation is detected within this latitude range. In contrast, the two spot group category (red vertical lines) have spots at a large latitude range. In the extreme case, there are spots near the equator and near the poles, so that the vertical line spans the entire envelope. The latitude distribution of spots may also vary over time due to activity cycles.

The subsynchronous population does not extend below orbital periods of approximately two days. There may be very little differential rotation on the most rapidly rotating, tidally synchronized stars. In that case, the higher latitude starspots will have the same rotation period as the equator. Alternatively, the starspots could preferentially be located near the

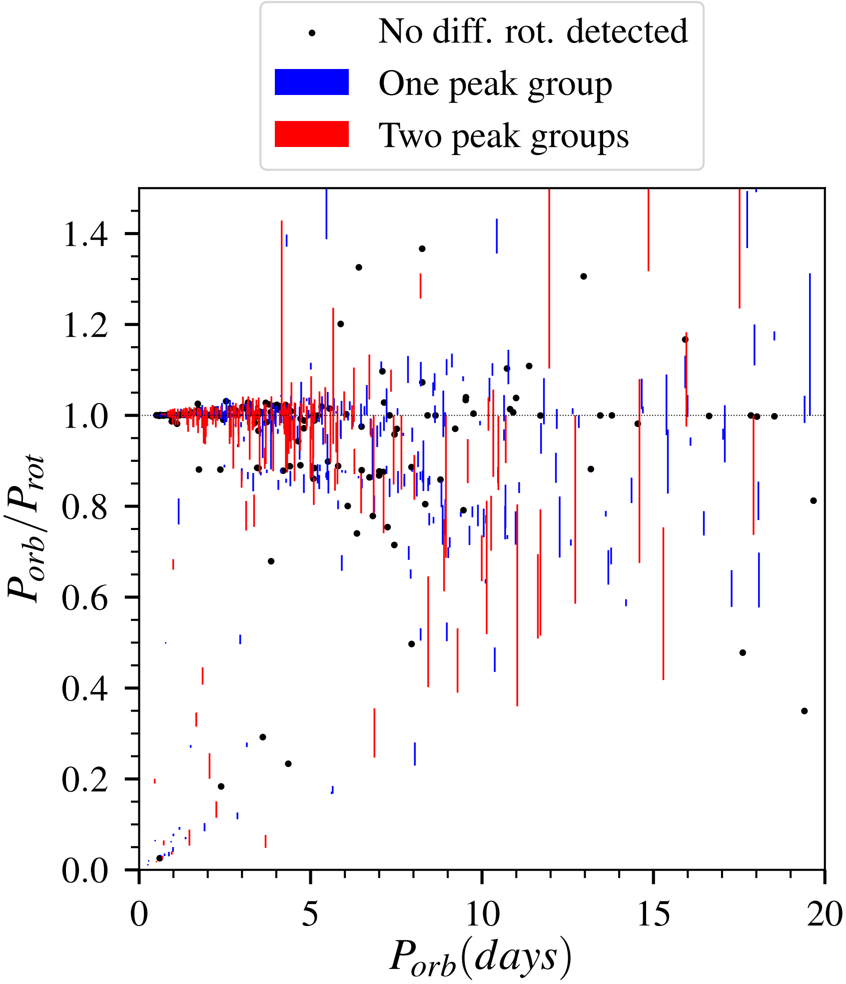

Figure 3.13: The distribution of period ratio versus orbital period. Vertical lines indicate EBs with multiple rotation periods due to differential rotation. Red lines are for EBs with two periodogram peak groups, and blue lines are for one peak group. As discussed in $3.5.1, both rotation periods most likely originate from the primary star. Black circles indicate EBs with only one rotation period measurement, for which differential rotation was not detected.

equator in these rapidly rotating stars.

The differential rotation scenario is consistent with two expectations from previous studies: that rapidly rotating stars have less differential rotation than the Sun (Collier Cameron, 2007; Küker & Rüdiger, 2011); and that rapidly rotating stars have starspots near their poles (Strassmeier, 2002). On the Sun, latitudes ±50° rotate roughly 13% slower than the equator (Beck, 2000), whereas the maximum latitude where sunspots occur is roughly 30°. This implies that the subsynchronous EBs have starspots at higher latitudes than the Sun, perhaps near the poles. If the subsynchronous starspot modulation originates from the poles, then the total equator to pole relative shear is $\alpha \approx 0.13$, compared to approximately 0.3 on the Sun. This is consistent with less differential rotation than the Sun.

It is possible that the subsynchronous population is comprised of evolved stars, whereas the synchronized population is comprised of main sequence stars. Two pieces of evidence that support this hypothesis are that the relative number of subsynchronous stars is greatest for K-type primaries (middle panel of Figure 3.10), and for EBs with shallow primary eclipses and no secondary eclipses (middle panel of Figure 3.11). Both of these results are consistent with an EB containing a K giant (or subgiant) and a G, K, or M dwarf. This hypothesis can best be tested with accurate luminosities from the upcoming Gaia data release. However, the subsynchronous population represents 15% of the total sample with orbital periods between 2 and 10. This relatively high percentage is at odds with the low fraction of evolved stars in the disk, combined with the *Kepler* target selection process that favored main sequence stars.

A combination of ellipsoidal variations and starspot modulations is an alternate explanation for the EBs with two periodogram peaks. In this case, the ellipsoidal variations cause the peak at the orbital period, and the starspot modulations cause the subsynchronous peak. However, when we folded the light curves at the orbital period, they showed no evidence of the ellipsoidal variations. We conclude that the periodicity is originating from starspot modulations.

Throughout this discussion, we have assumed that the stars are tidally synchronized to the rotation period at the equator. It is possible that the subsynchronous EBs have achieved resonance locking with convective motions or gravity modes, rather than the surface rotation (Burkart et al., 2014). Alternatively, the EBs could be synchronized to the rotation rate of the radiative core if the tidal energy is dissipated there (Witte & Savonije, 2002). In any case, these results provide a new and important test for tidal theory.

3.6 Additional Results

3.6.1 Starspot Occultations on a Candidate RS CVn System

We briefly highlight the interesting EB KIC 10614158. It is listed in the KEBC as having an orbital period of 4.46 days, and only primary eclipses. It has an effective temperature of 4600 K according to the *Kepler* Input Catalog. Visual inspection of the light curve shows that every other eclipse has a completely flat bottom, while the intervening eclipses have bumps that appear to be spot occultations[3]. Some flares and instrument-related discontinuities are also visible.

This pattern is demonstrated in Figure 3.14, where each successive eclipse is vertically offset for clarity. The spot occultations occur near phase zero and move in phase over time. This pattern is inconsistent with only primary eclipses. We instead argue that KIC 10614158 has an orbital period of 8.92 days. The primary eclipses with spot occultations occur when the main-sequence star passes in front of the larger, more luminous evolved star, which has spots. The secondary eclipses occur when the main-sequence star disappears behind the evolved star. KIC 10614158 is a good target for further investigation, as it provides a unique opportunity to study the tidal interaction and starspot distribution of evolved stars.

3.6.2 The Period-Color Relation for Contact Binaries

There is a well known relation between the orbital periods and photometric colors of contact binaries (e.g, Eggen 1967; Rucinski 1994; Rubenstein 2001). These stars are filling their Roche lobes, directly linking the orbital period to the stellar radius, mass, and photometric color. The redder contact binaries (larger color indices) have shorter orbital periods, implying

---

[3] See Silva (2003) and Morris et al. (2017) for examples of spot occultations by planets orbiting main sequence stars.

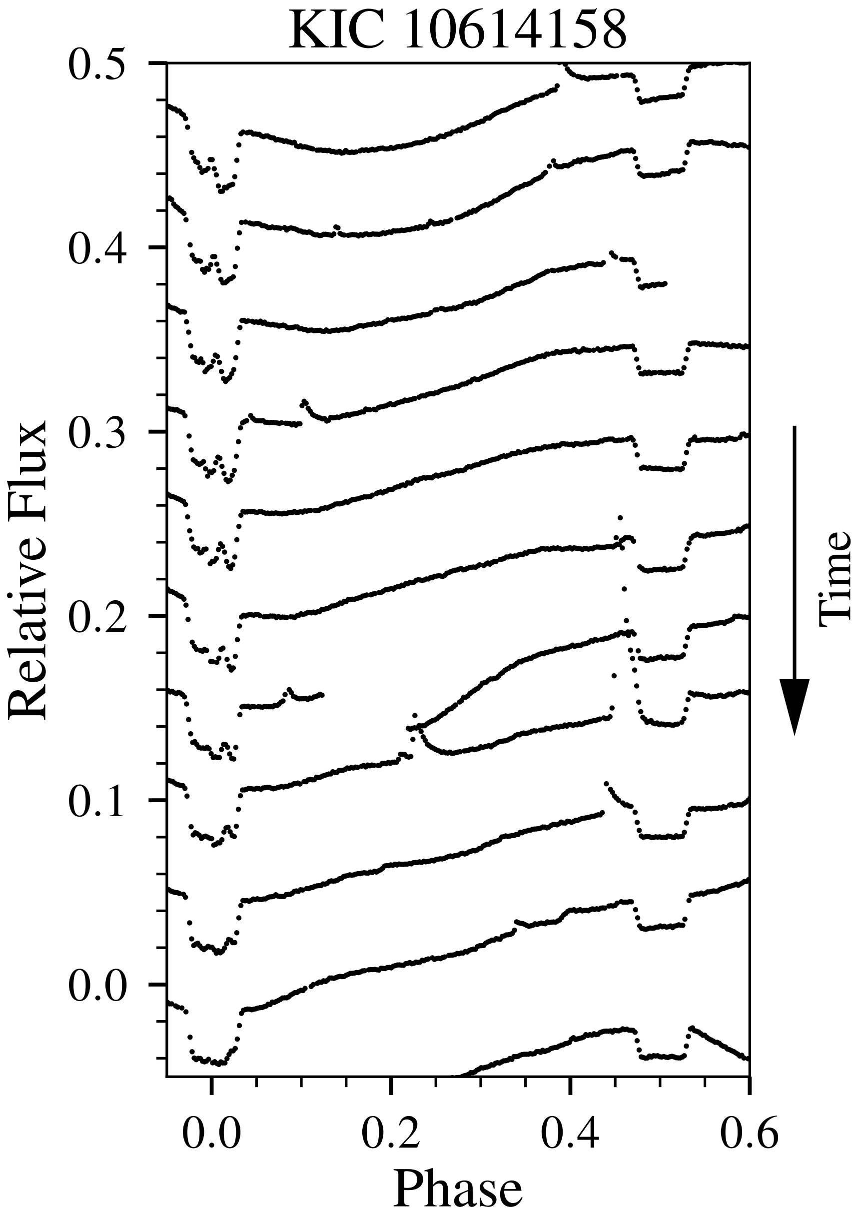

Figure 3.14: Successive eclipses for the candidate RS CVn system KIC 10614158. Time increases towards the bottom of the figure. Spot occultations are visible in the primary eclipses near phase zero, while the secondary eclipses at phase 0.5 have flat bottoms.

smaller stellar radii.

Figure 3.15 shows the distribution of orbital periods versus dereddened $J-K$ colors for EBs with ellipsoidal variations and orbital periods less than 0.6 days. These EBs appear to be contact binaries based upon their light curves. For comparison, we show the period-color relation from Chen et al. (2016), based on a fit to over 6000 contact binaries collected from the literature. Their relation is a good fit to our sample as well.

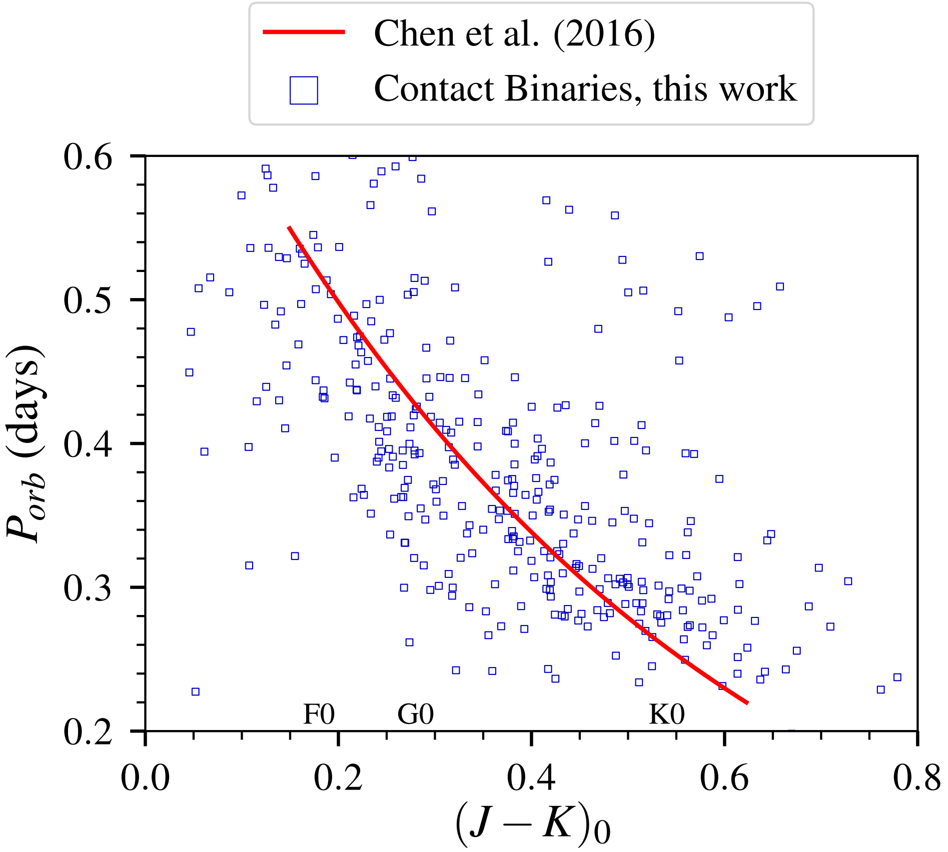

Figure 3.15: The distribution of orbital period versus dereddened $J-K$ color for contact binaries. The red curve shows the empirical period-color relation from Chen et al. (2016). Spectral types from Covey et al. (2007) are shown for reference.

3.7 Conclusion

We have analyzed 2278 EBs in the *Kepler* Eclipsing Binary Catalog for evidence of tidal synchronization. EBs were visually classified based on their out-of-eclipse variability as having starspot modulations, ellipsoidal variations, pulsations, other out-of-eclipse variability, or no out-of-eclipse periodic variability. For EBs with starspot modulations, we measured multiple rotation periods using a combination of the autocorrelation function and the Lomb-Scargle periodogram. Our main results are summarized as follows:

- At orbital periods less than 10 days, most EBs are tidally synchronized. Below two days, 94% of EBs are synchronized, defined as having rotation periods within 10% of their orbital periods. At orbital periods between two and ten days, this number is 72%.

- There is a population of subsynchronous EBs, which has not been observed in previous studies. Between orbital periods of two and ten days, 15% of EBs have rotation periods that are typically 13% longer than their orbital periods.

- This subsynchronous population has low eccentricities, slightly favors lower mass ratios, and shows no strong correlation with mass for F, G and K type primaries.

- We demonstrated that the subsynchronous population is consistent with differential rotation. Over three quarters (77%) of EBs with starspot modulations have multiple rotation periods, which are likely originating from differentially rotating active latitudes on the primary star. The primaries are likely synchronized to the rotation period at the equator, and spots near the poles cause the measured rotation period to be longer than the orbital period. Some EBs appear have spots near both the equator and poles, perhaps due to activity cycles or a range of differential rotation profiles.

- At an orbital period of roughly 10 days, there is a transition from primarily circularized and synchronized EBs to primarily eccentric and pseudosynchronized EBs. This transition is in good agreement with the predicted and observed tidal circularization period for Milky Way field binaries.

- Our rotation period catalog mostly contains EBs with F, G and K type primary stars, because the *Kepler* target selection favors solar-type stars, and because starspot modulations are not found on earlier type stars. This is beneficial in that it greatly increases the number of published rotation period measurements for such binaries. There is no clear difference in synchronization between F, G and K primaries, suggesting that primary mass is not an important factor in synchronization over the relatively small mass range of F, G and K stars.

- For both small and nearly equal mass ratios, EBs with periods less than 10 days are highly synchronized. Beyond ten days, EBs with small mass ratios are somewhat less synchronized than EBs with nearly equal mass ratios.

The tidal interaction of close binaries is an important aspect of stellar astrophysics, but also has much broader implications for stellar populations. Our results represent a substantial increase in the observational data for tidally interacting late-type binaries, and offer many opportunities for further investigation. The transition from circular, synchronized EBs to eccentric, pseudosynchronized EBs is worthy of additional modeling to better understand the complex dynamics at work. The same can be said for the differential rotation mechanism we introduced to explain the population of subsynchronous EBs.

Chapter 4

ASYMMETRIES IN THE MILKY WAY DISK

The previous two chapters used *Kepler* photometry to investigate the rotation and magnetic activity of a wide binary, and the tidal interaction of close binaries. Due to the richness of the *Kepler* light curves, each star was regarded as an individual astrophysical object with its own complex behavior. However, *Kepler* only probed a small volume of the Milky Way.

This chapter also uses photometry of low mass stars, but from a different survey and in a different manner. Rather than analyze stellar variability, this chapter analyzes the average colors and brightnesses of millions of stars over 75% of the sky imaged by the Pan-STARRS survey. In this way, it is possible to use low mass stars as tracers of Galactic structure.

The stellar density distribution of the Galactic disk is highly complex, containing numerous overdensities and asymmetries. These substructures are often cited as evidence of interactions with satellite galaxies in the cosmological context of hierarchical galaxy formation, although internal processes undoubtedly also play an important role.

Previous studies have approached these issues using low mass stars as tracers of disk structure, but were limited by the lack of deep optical photometry of the disk. This chapter uses Pan-STARRS photometry to search for disk asymmetries in a comprehensive, model-independent manner. The results reveal new details about how the different substructures may be related.

Material from this chapter is being prepared for publication in collaboration with Mario Jurić, Edward F. Schlafly, and Colin T. Slater.

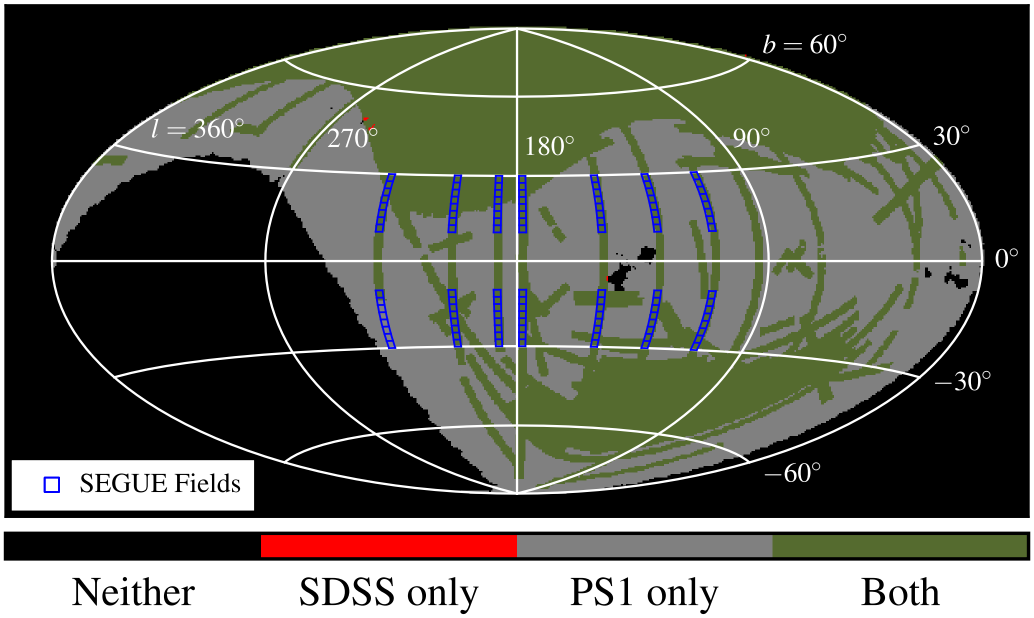

Figure 4.1: The SDSS and PS1 survey footprints, shown as a Hammer equal-area projection in Galactic coordinates. The PS1 footprint contains the entire SDSS footprint, with the exception of the small areas in red. PS1 has dramatically more coverage at low Galactic latitudes. The edge of the PS1 survey at declination -30° is indicated by the yellow line. Blue boxes indicate the SDSS SEGUE stripe fields analyzed by Xu et al. (2015). We repeat their analysis with PS1 data in §4.3.

4.1 Introduction

To first order, the vertical density distribution of the Milky Way (MW) disk is often treated as smooth and symmetric. Yet it has long been known that this is an oversimplification (e.g., the HI disk warp, Burke 1957; Kerr et al. 1957; Westerhout 1957). In recent years, large scale photometric surveys have revealed asymmetries in the stellar component of the MW disk. Using photometry from the Sloan Digital Sky Survey (SDSS, York et al., 2000), Widrow et al. (2012) and Yanny & Gardner (2013) found three asymmetries within 1 kpc of the Sun. There is one over-density of stars ∼0.5–1.0 kpc above the plane, and two overdensities ∼0.3–0.5 kpc and ∼1.0–2.0 kpc below the plane. Xu et al. (2015) et al. also found a wave-like series of disk asymmetries in the SDSS data, extending from 2 - 16 kpc from the Sun towards the galactic anticenter. At least some of these asymmetries are likely due to bending mode oscillations (warps) in the MW disk.

Interactions with satellite galaxies can lead to bending mode oscillations by transferring energy to disk stars (Toth & Ostriker, 1992; Sellwood et al., 1998). Along with bending modes, satellite interactions are also expected to induce breathing mode oscillations (compression-rarefaction, Widrow et al. 2014). Evidence for such breathing modes have been found in three independent radial velocity studies of the MW disk (Widrow et al., 2012; Carlin et al., 2013; Williams et al., 2013). The relative strengths of the bending and breathing modes depend on the velocity of the satellite perpendicular to the disk (Widrow et al., 2014). In addition to satellite properties, studies of disk oscillations may help constrain the properties of the dark matter distribution (Binney, 1978).

The discoveries of oscillations in the MW disk have also led to renewed debate over the origin of the Monoceros Ring (MRi). The MRi was originally discovered as a stellar overdensity near the edge of the SDSS footprint (Newberg et al., 2002; Yanny et al., 2003). It is now known to extend from $120° < l < 240°$ and $-30° < b < 40°$, with a galactocentric distance range of roughly 12 - 19 kpc (Morganson et al., 2016). The MRi was originally characterized as the tidal debris of a dwarf galaxy (Martin et al., 2004; Peñarrubia et al., 2005), but may alternatively be part of the perturbed MW disk (Momany et al., 2004; Kazantzidis et al., 2008). Slater et al. (2014) found that neither tidal debris nor disk perturbation models were entirely consistent with observations of the MRi. Subsequently, Gómez et al. (2015) analyzed cosmological N-body simulations of MW-like galaxy, and found that a satellite interaction with the host halo triggered disk oscillations that better reproduced the MRi observations. Yet it remains unclear if and how the bending mode oscillations at smaller radii are related to the MRi.

In this context, we set out with two questions in mind: (1) What asymmetries are present in the MW disk, and (2) are they consistent with a bending wave perturbation? To answer the first question, we used photometry from the Panoramic Survey Telescope and Rapid Response System 1 survey (PS1, Chambers et al., 2016) to identify and characterize asymmetries in the MW disk. PS1 has vastly increased coverage of the Galactic plane compared to SDSS, and allows us to see the asymmetries in an improved and contiguous manner. Our asymmetry mapping technique is model independent, and involves subtracting color magnitude diagrams[1] (CMDs) for sight lines above the plane from sight lines at the same longitudes but opposite latitudes. To answer the second question, we generated mock photometric catalogs for a toy model MW-like galaxy with bending mode perturbations, and produced a map of asymmetries using the same technique.

The remainder of the chapter is divided as follows. In §4.2, we describe the PS1 survey and our sample selection, accounting for potential systematics that could bias our asymmetry analysis. In §4.3, we demonstrate that asymmetries exist over a large portion of the outer MW disk, and validate the PS1 observations by comparison against SDSS results. In §4.4, we explain our automated asymmetry identification and mapping technique. In §4.5, we present maps of the asymmetries identified in PS1 data. In §4.6, we introduce our toy model for bending mode perturbations, generate mock catalogs, and present maps of the asymmetries in the mock catalogs. We discuss the implications of our results in §4.7, and summarize in §4.8.

4.2 Pan-STARRS1 Data

In this section, we prepare the PS1 data for our asymmetry analysis, but we first provide a brief summary of the survey. The survey imaged the entire sky north of declination −30°, as shown Figure 4.1. The survey used five filters: $g_{\rm P1}$, $r_{\rm P1}$, $i_{\rm P1}$, $z_{\rm P1}$, and $y_{\rm P1}$, which are similar to those used in SDSS. The most important difference is that $g_{\rm P1}$ filter is 20 nm wider at the red end compared to $g_{\rm SDSS}$ (Tonry et al., 2012). The data reduction pipeline consisted of image processing (Magnier, 2006), calibration (Schlafly et al., 2012), and zero

---

[1] Strictly speaking, our analysis uses Hess diagrams, which represent the color-magnitude distribution as a 2-D histogram. For simplicity, we refer to them as CMDs.

point determination (Tonry et al., 2012). The pipeline produced a catalog of calibrated, single exposure magnitudes, to which we applied additional processing.

4.2.1 Producing a Stellar Sample

In order to reject bad data, the objects in our sample must have at least two detections in $g_{\rm P1}$ and $i_{\rm P1}$ that pass the following quality cuts. We rejected detections with any of the PS1 pipeline flags listed in Table 4.1, and we only included detections that fell on at least 85% unmasked pixels (`PSF_QF` > 0.85, Magnier et al. 2013). For our asymmetry analysis, we used the median PSF magnitudes of multiple detections, but also used the median aperture magnitudes for star-galaxy separation, as discussed below.

To analyze asymmetries in the MW disk, we must remove galaxies and other non-stellar sources from the catalog to the furthest extent possible. The PS1 catalog does not include star-galaxy separation, so we must perform it on our own. Model magnitudes (e.g., exponential or de Vaucouleurs) are optimal for galaxy photometry, but the PS1 pipeline (Processing Version 2) does not calculate them. Instead, we used the difference between PSF and aperture magnitudes. We only included objects that met

$$-0.2 < i_{_{PSF}} - i_{_{ap}} < 0.1 \tag{4.1}$$

The positive cutoff of 0.1 excludes galaxies and other extended sources. The difference between PSF and aperture magnitudes will be positive for extended sources because the aperture includes more flux, resulting in a more negative magnitude. The negative cutoff of -0.2 excludes stars in crowded fields and artifacts of image processing issues (Morganson et al., 2016).

We validated our star-galaxy classification by comparison against the SDSS pipeline classification, which includes model magnitudes. We matched objects in the PS1 catalog with $b > 70^\circ$ to the nearest object within $1''$ in the SDSS DR8 catalog (Aihara et al., 2011). This resulted in 3.1 million objects classified by SDSS as galaxies (`objc_type = 3`), and 2.9 million stars (`objc_type = 6`).

Table 4.1. Data Quality Bit-flags

Flag Name	Hex Value	Description
FITFAIL	0x00000008	Fit (non-linear) failed (non-converge, off-edge, run to zero)
POORFIT	0x00000010	Fit succeeds, but low S/N, high chi-squared
SATSTAR	0x00000080	Source model peak is above saturation
BLEND	0x00000100	Source is a blend with other sources
EXTERNALPOS	0x00000200	Source based on supplied input position
BADPSF	0x00000400	Failed to get good estimate of object's PSF
DEFECT	0x00000800	Source is thought to be a defect
SATURATED	0x00001000	Source is thought to be saturated pixels (bleed trail)
CR_LIMIT	0x00002000	Source has crNsigma above limit
EXT_LIMIT	0x00004000	Source has extNsigma above limit
MOMENTS_FAILURE	0x00008000	Could not measure the moments
BIG_RADIUS	0x00100000	Poor moments for small radius
SIZE_SKIPPED	0x10000000	Size could not be determined

Note. — Detections with any of the above quality flags were rejected from our sample. Quality flag names, hex values, and descriptions are taken from `https://confluence.stsci.edu/display/PANSTARRS/PS1+Detection+Flags`

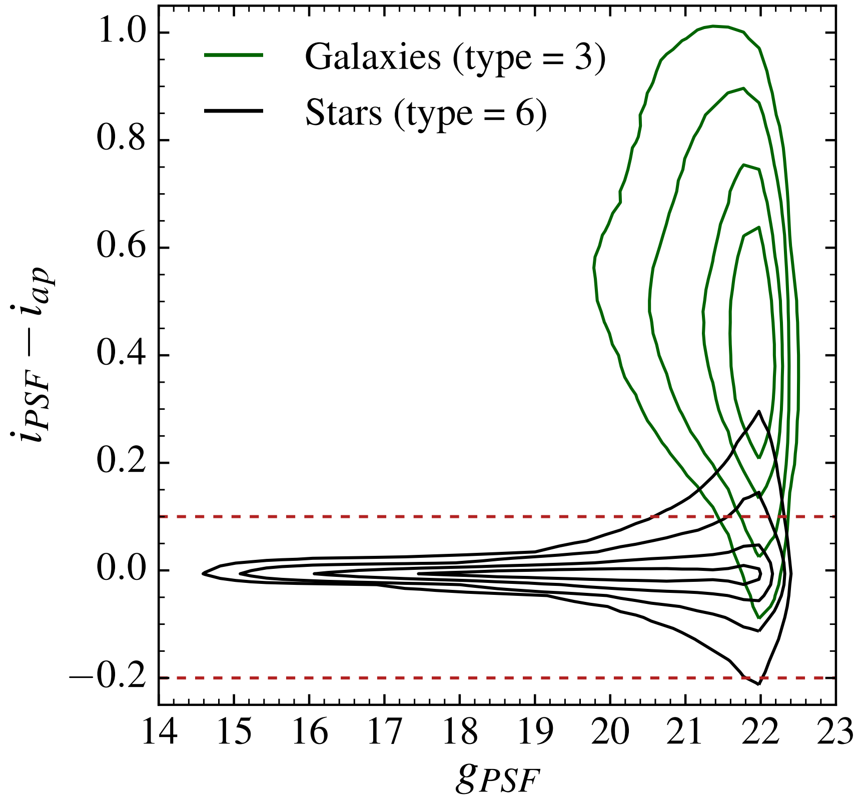

Figure 4.2: Star-galaxy separation using the difference between i_{P1} PSF and aperture magnitudes, plotted versus g_{P1} PSF magnitude. Green contours: objects identified as galaxies (`objc_type = 3`) in the SDSS pipeline. Black contours: objects identified as stars (`objc_type = 6`). The contours contain 90, 75, 50, and 25% of the respective distributions. We classify objects between the dashed red lines as stars in our sample. Compared to SDSS, we correctly classify 88% of stars, with only 3.4% of galaxies misclassified as stars. These values improve to 97% and 0.67% respectively for objects brighter than $g_{PSF} < 21$.

Figure 4.2 shows the results of the SDSS cross-match. The difference between i_{P1} PSF and aperture magnitudes is plotted versus g_{P1} PSF magnitude. Green contours correspond to objects identified as galaxies by the SDSS photometric pipeline, while black contours correspond to stars. The contours contain 25, 50, 75, and 90 percent of the respective distributions. Objects between the the dashed red lines were classified as stars in our sample.

The distributions of stars and galaxies are well separated, and the criterion in Equation 4.1 is successful at classification. 88% of stars are correctly classified compared to SDSS, while only 3.4% of galaxies are misclassified as stars. These values improve to 97% and 0.67% respectively for objects brighter than $g_{PSF} < 21$. Our sample is still contaminated by a small percentage ($\lesssim 5\%$, Jurić et al. 2008) of faint quasars, which are difficult to remove with *grizy* photometry. Fortunately, quasars are distributed isotropically on the sky, and will cancel out in the residual CMDs. In summary, our stellar sample is well suited for our MW asymmetry analysis.

4.2.2 Correcting for Extinction

We intend to study stars in the MW disk, some of which are significantly extincted. To correct for extinction, we used the SFD (Schlegel, Finkbeiner, & Davis, 1998) maps of reddening $E(B-V)$, and converted $E(B-V)$ to extinction A_λ in the Pan-STARRS filters using the coefficients from Schlafly & Finkbeiner (2011) with $R_V = 3.1$. Extinction-corrected magnitudes are denoted with the subscript 0 throughout the remainder of this chapter, e.g., g_0. We discuss how extinction affects our asymmetry analysis in §4.7.4.

4.2.3 Sky Binning and Spatial Completeness

For a large-area survey such as PS1, it is important to divide up the sky in an efficient manner. We binned the sky into two 90×90 pixel Lambert azimuthal equal-area projections centered at each Galactic pole. Each sky pixel has an area of 3.2 square degrees. This projection forms the base of our analysis. We will use it to determine the spatial completeness of our sample. In our later asymmetry analysis, we will generate CMDs for each sky pixel, and then subtract the southern Galactic hemisphere from the north.

We need to determine the spatial completeness of our sample, because the asymmetry analysis requires overlapping coverage above and below $b = 0°$. This step is also necessary because differences in spatial completeness between corresponding north-south pixels could introduce false asymmetries. We determined the spatial completeness by dividing each of the 90×90 sky pixels into a 40×40 subpixel grid, where each subpixel has an area of 7.3 square arcmin. The spatial completeness in each 90×90 pixel is equal to the number of sub-pixels containing at least one object divided by the total number of sub-pixels.

Figure 4.3 shows the spatial completeness of our sample. The top and bottom panels are for the northern and southern hemispheres, respectively. The grey reference grid indicates Galactic longitudes and latitudes. The lower limit of the colorbar is truncated at 0.7 (70% completeness) to emphasize areas of partial completeness.

We can now define the sample area with overlapping north-south coverage in which we will search for asymmetries. This area is outlined in black in Figure 4.3. To avoid sight lines with high extinction, we also exclude sky pixels with $|b| < 10^\circ$. The spatial completeness in our sample area is high and nearly uniform. There are some areas of partial completeness, but 96% of sky pixels are at least 95% complete. In total, our sample area contains 6598 sky pixels covering over 21,000 square degrees.

4.3 An Overview of the Asymmetric Milky Way

In this section, we produce CMDs for a representative subset of longitudes. This analysis follows that of Xu et al. (2015, hereafter X15), who analyzed the same longitudes using SDSS photometry, thus providing a validation of our PS1 sample. The CMDs demonstrate that asymmetries exist over a large area in a visually intuitive manner.

X15 analyzed SDSS photometry from the Sloan Extension for Galactic Understanding and Exploration (SEGUE, Yanny et al. 2009). Their sample area consisted of seven $2\overset{\circ}{.}5$ wide stripes with central longitudes of $110^\circ < l < 229^\circ$, in the latitude range $10^\circ < |b| < 30^\circ$. By design, the SEGUE stripes were observed along lines of constant Galactic longitude. For our analysis, we used the PS1 data described in §4.2 over the same regions as the SEGUE stripes. Like X15, we divided each stripe into sixteen $2\overset{\circ}{.}5$ square fields, outlined in blue in Figure 4.1.

We corrected the CMDs for spatial incompleteness using the maps described in §4.2.3.

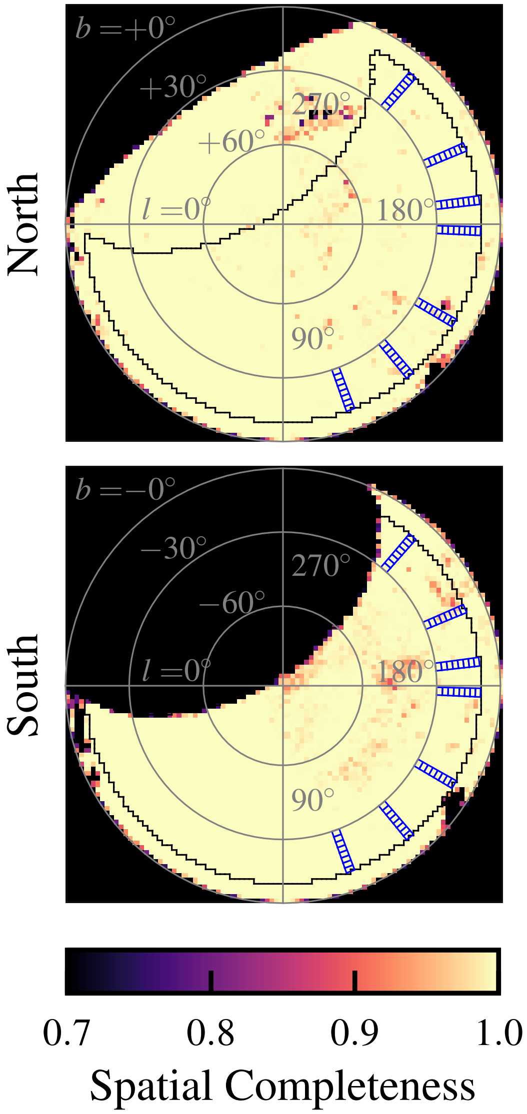

Figure 4.3: The spatial completeness of our sample, shown as 90 × 90 pixel Lambert azimuthal equal-area projections for the northern (top panel) and southern (bottom panel) Galactic hemispheres. Blue boxes indicate the SEGUE fields analyzed in §4.3. Our sample area is outlined in black. The spatial completeness is high: 96% of fields are at least 95% complete.

The SEGUE fields are outlined in blue in Figure 4.3. Because the CMDs are two dimensional histograms, we simply divided each one by the corresponding completeness in each field. The corrections were minimal: 92% of fields required no correction, and the largest correction was 1.2%. This correction ensures that the features we see are not due to differences in spatial completeness.

The g_0 versus $(g-i)_0$ CMDs for the northern and southern SEGUE fields are shown in the top and bottom panels of Figure 4.4, respectively. The central longitude of each field is indicated at the top of the panels, and the latitude ranges are indicated on the right side. The median g_{P1} extinction is printed in the upper right corner of each field. Each row (latitude) in both the north and south has the same colormap range, corresponding to the 98th percentile value of all pixels on those rows.

For an arbitrary sight line, stars should be distributed smoothly in apparent magnitude, assuming the stellar number density is a smooth function. This is not the case for the CMDs in Figure 4.4. Stars will be concentrated in apparent magnitude if they are at a similar distance from the observer. This occurs in the familiar case of star clusters, but these have a small angular extent. The CMDs in Figure 4.4 have magnitude-concentrated features over 109° of Galactic longitude, suggesting that there are over-densities over a large area of the MW disk.

The northern CMDs contain several features that were seen by X15. The northern portion of the MRi is visible as the blue tip and turnoff of a main sequence at $(g-i)_0 \sim 0.3$ and $g_0 \sim 19$. The "north near" asymmetry (following the naming convention of X15) resembles a main sequence that is 3 to 4 magnitudes brighter than the north MRi. Additionally, there is a horizontal distribution of stars centered at $(g-i)_0 \sim 2.0$ and $g_0 \sim 21.5$. This feature is due to nearby late-type main sequence stars near the photometric detection limit of PS1.

The southern latitude CMDs are shown in the bottom panel of Figure 4.4. The southern portion of the MRi is at $(g-i)_0 \sim 0.5$ and $g_0 \sim 18$. X15 referred to this as the "south middle" feature, distinct from the north MRi. We revisit the appropriateness of this distinction in §4.7. Nearby late-type main sequence stars occupy the bottom right corner of the CMDs.

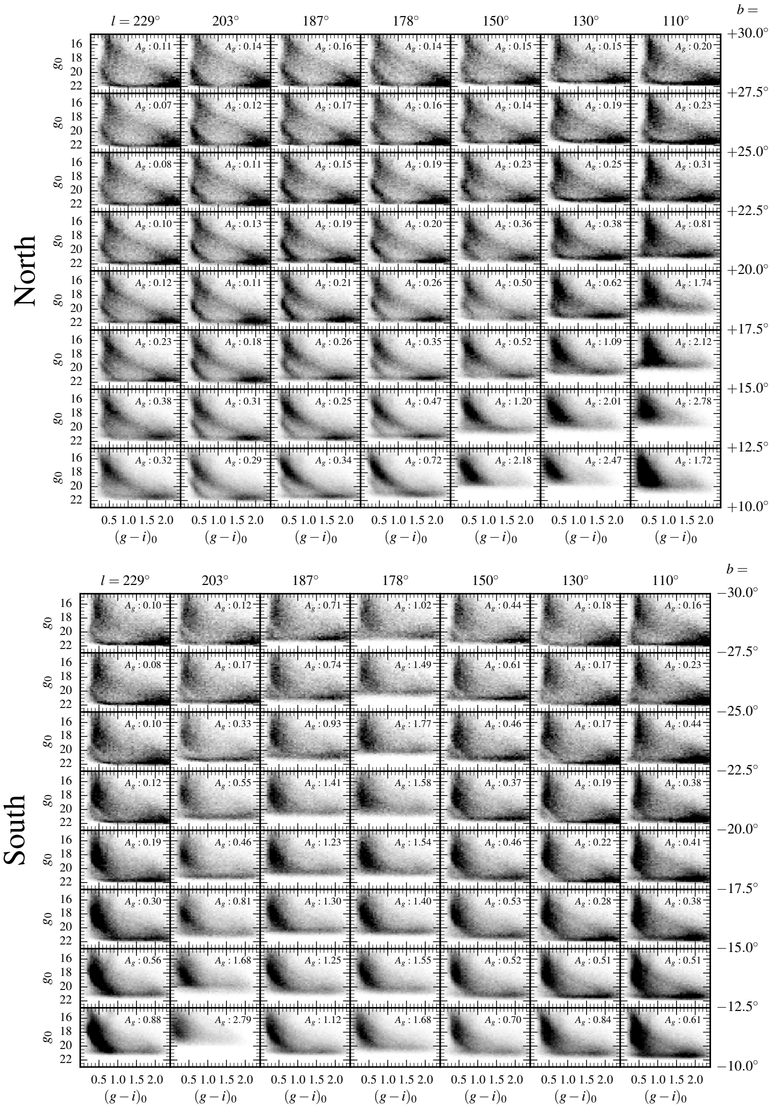

Figure 4.4 CMDs for the northern (top panel) and corresponding southern (bottom panel) SEGUE fields. These correspond to the regions outlined in blue in Figure 4.1. The central longitudes and latitudes of the fields are indicated above and to the right of the panels. The median g_{P1} extinction in each field is indicated in the upper right corner of each cell. Each row (latitude) in both the north and south is on the same colormap scale, having maximum values equal to the 98th percentile value of all pixels in those rows. Four features are visible over a wide range of l and b, which are discussed in §4.3. Note that the longitude and latitude orders are reversed compared to Figures 2 and 3 in Xu et al. (2015).

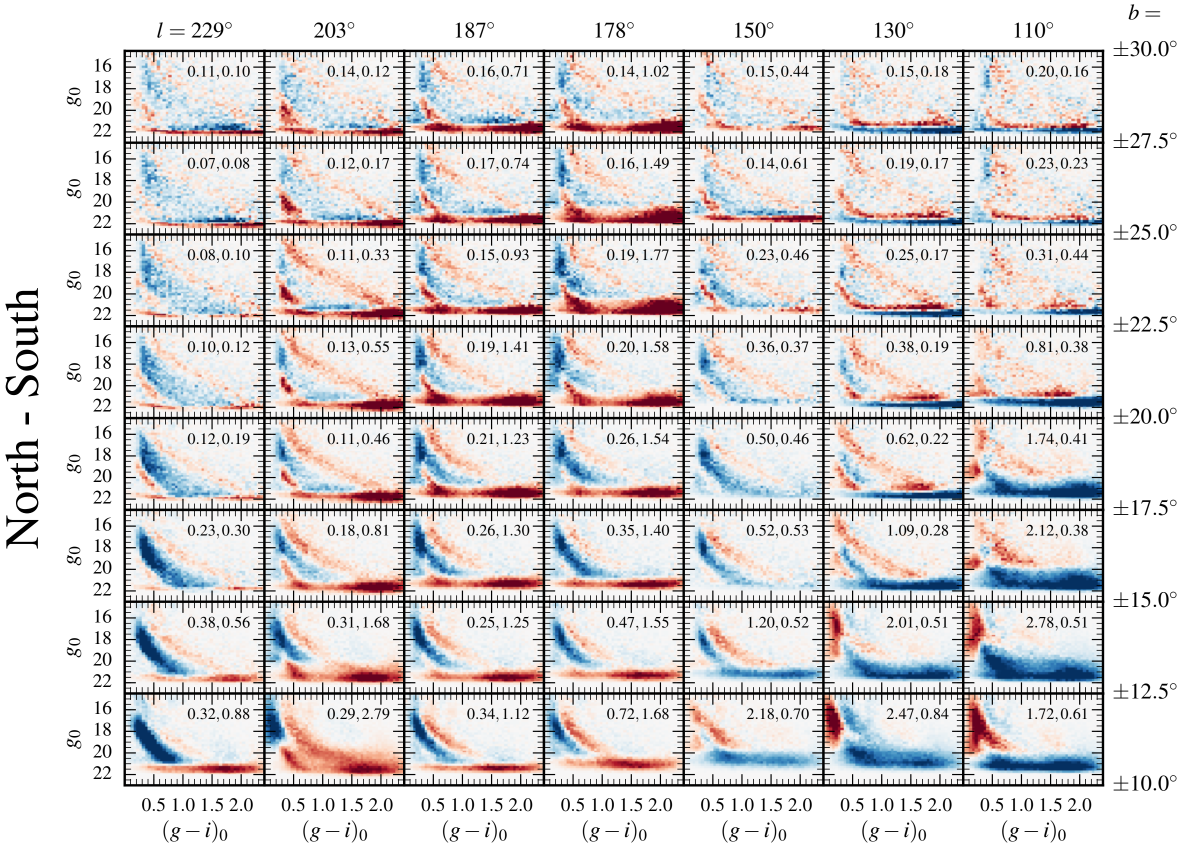

Figure 4.5: The residuals from subtracting the southern CMDs in Figure 4.4 from the corresponding diagrams in the north. White indicates no difference, red pixels indicate an excess of stars in the north, while blue pixels indicate an excess in the south. The median $g_{\rm P1}$ extinctions in each northern and southern field is indicated in the upper right corner of each panel. Each row (latitude) is on the same colormap scale, with maximum and minimum values equal to the 98th percentile of the absolute values of all the pixels in the row. Three asymmetric features are visible over a wide range of l and b, which are discussed in §4.3. Note that the longitude and latitude orders are reversed compared to Figure 4 in Xu et al. (2015).

Like in the north, the southern CMDs are consistent with those of X15, although the PS1 data have a fainter limiting magnitude.

In the southern CMDs, a feature X15 associated with the Triangulum Andromeda asymmetry (TriAnd, Majewski et al. 2004; Rocha-Pinto et al. 2004) is barely visible at $(g-i)_0 \sim 0.3$ and $g_0 \sim 20$ in some sight lines, particularly those with $b < -22.5°$. In some sight lines, the TriAnd overlaps in color-magnitude space with the north MRi. The north MRi has more star counts, and therefore we do not detect the TriAnd in the residual CMDs presented below. This is not a significant issue for this work because we are not focused on the TriAnd.

The CMDs in Figure 4.4 are evidently not symmetric with respect to $b = 0°$. To better illustrate this, we subtract the CMDs for the southern latitudes from the diagrams at the corresponding northern latitudes, as shown in Figure 4.5. The colormap in each row is normalized to the 98th percentile of the absolute value of all pixels in that row. For a given color and apparent magnitude range, the color of each pixel corresponds to the difference in star counts at a given longitude and northern latitude, and the corresponding coordinates in the south. White pixels indicate no difference, red pixels indicate an excess in the north, while blue pixels indicate an excess in the south.

If the observed star counts were symmetric with respect to $b = 0°$, the residual CMDs should have no features other than random noise. Instead, the northern and southern CMDs are dramatically different, and the distributions of stars are offset by nearly two magnitudes. There are three distinct features that resemble main sequences. The north near, south MRi, and north MRi alternate in a north-south sense with increasing apparent magnitude. This suggests a bending mode asymmetry in the MW disk over a large longitude range, which we demonstrate more fully in §4.5 - 4.7.

4.4 The Asymmetry Mapping Technique

Due to the large number of CMDs in our sample, it is not feasible to manually identify individual features in all of them. However, we want to use the information contained in the residual CMDs because we can see the asymmetries in an intuitive and model-independent way. Therefore we have developed an automated algorithm to detect and measure CMD features. This enables a consistent and uniform analysis over a large area with minimal human intervention. The process has two steps which are outlined in this section. First, candidate features are identified in CMDs, and then template features are fit to determine distances and reject spurious features.

4.4.1 CMD Feature Identification

To search for asymmetries, we generated CMDs for the pixels in the Lambert projection within the sample area described in §4.2.3 and outlined in black in Figure 4.3. The CMDs had a maximum apparent magnitude of $g_0 = 21$ to avoid the extinction effects discussed in §4.7.4. The star counts in pixels with partial coverage were corrected for incompleteness using the spatial completeness maps in §4.2.3. Next, we subtracted the CMDs in the southern projection from the corresponding diagrams in the northern projection to produce residual CMDs analogous those in Figure 4.5. This resulted in 3299 residual CMDs over 21,000 square degrees in which we wish to automatically identify asymmetric features.

The top left panel of Figure 4.6 shows a representative residual CMD for the sight line centered at $(l, |b|) = (198.4^\circ, 20.3^\circ)$. By eye, it is clear that this CMD contains three asymmetric features: two in the north and one in the south. The challenge is to write a computer algorithm that will recognize and define the boundaries of the features. To do so we used image segmentation, which is a standard technique for identifying features in images (Sezgin & Sankur, 2004). In this case pixel values correspond to residual star counts, rather than intensity as in traditional image analysis, but the technique is still analogous.

We smoothed the residual CMDs prior to identifying features because the CMDs are somewhat noisy, which interferes with the identification. The color-magnitude pixels are small and more susceptible to random fluctuations. To reduce noise, we applied a Gaussian smoothing filter to the CMDs. The Gaussian kernel had a standard deviation equal to one pixel. We found that the identification routine performed better on smoothed CMDs with small pixels than on unsmoothed diagrams with large pixels.

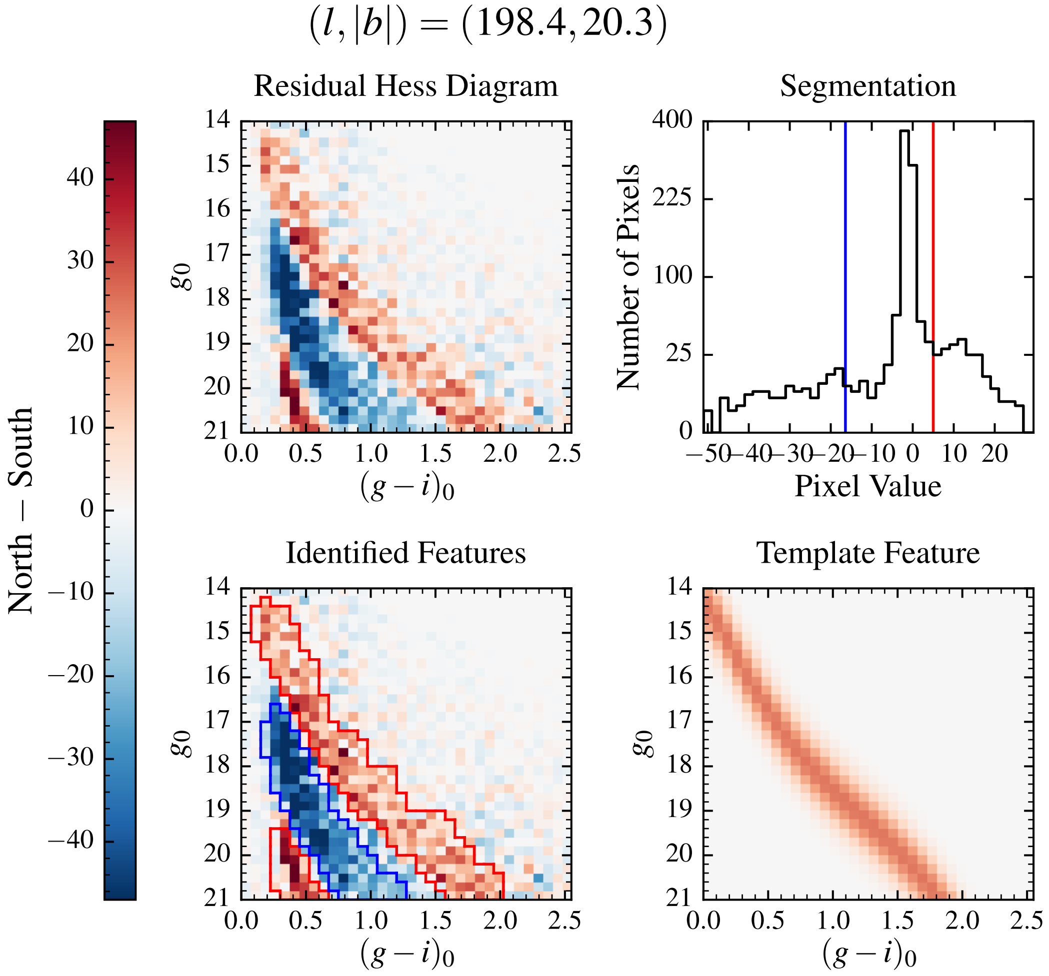

Figure 4.6: A demonstration of the CMD feature identification algorithm. Top left panel: A representative residual CMD. Three asymmetric features are visible: two in the north and one in the south. Top right panel: Features are identified by image segmentation, separating pixels into negative (southern) features (below blue line), background pixels (between lines), and positive (northern) features (above red line). Bottom left panel: Positive and negative features are outlined in red and blue, respectively. Bottom right panel: The best fitting template isochrone for the topmost feature in the left panels.

Image segmentation involves finding two thresholds that divide pixels into three groups. Negative-valued pixels below a given threshold belong to candidate southern features, while positive-valued pixels above a second threshold belong to candidate northern features. Pixels with values between the two thresholds belong to the background. The threshold values were found using the Minimum Cross Entropy (MCE) method (Li & Lee, 1993; Li & Tam, 1998). The MCE method is well suited to instances such as ours where the values of feature pixels are close to the background level. Techniques exist for multilevel thresholding, in which case we could simultaneously find both the positive and negative thresholds. Unfortunately, this could result in an invalid case where both thresholds are either negative or positive. Instead, we only considered pixels with values > 0 when determining the positive threshold, and < 0 for the negative threshold.

The top right panel of Figure 4.6 shows a histogram of the pixel values for the smoothed CMD. The number of pixels in each bin is on a square-root scale. The red and blue lines indicate the negative and positive thresholds, respectively. The pixel values for the northern and southern features are very close to the background level, but the MCE method finds threshold values that accurately identify the features, as described below.

The final step in the identification process is to determine which pixels represent coherent features. The image segmentation process only uses the values of the pixels, and has no knowledge of the pixel locations. Individual features are defined as regions of neighboring positive or negative pixels that touch on at least one edge.

The bottom left panel of Figure 4.6 shows the results of the candidate CMD feature identification. The pixels belonging to each candidate CMD feature are outlined in red and blue for the positive and negative features, respectively. The algorithm successfully identified all three features.

4.4.2 CMD Feature Fitting

The asymmetric features identified by the algorithm, like those in Figure 4.6, resemble main sequences. To determine the distances to the features, we fit a template feature based on a PARSEC isochrone (Bressan et al., 2012) . This step also rejects features that only have a small number of pixels, or do not resemble a main sequence. We stress that the feature *identification* algorithm described above is model independent. The feature *fitting* algorithm is necessarily model dependent. However, the choice of isochrone determines the absolute distances of the features, but not their relative distances from the Sun. As we argue below, our fundamental conclusions about MW asymmetries are independent of the isochrone parameters.

The feature template t is given as

$$t(g,(g-i)|\sigma,d) = \frac{1}{\sigma\sqrt{2\pi}}\exp\left(-\frac{1}{2}\left(\frac{g-(M(g-i)+d)}{\sigma}\right)^2\right) \tag{4.2}$$

where g and $(g{-}i)$ are the apparent magnitude and color of a pixel. The distance modulus d is the offset to the absolute magnitude needed to match the observed apparent magnitude, and σ is the standard deviation in magnitudes. $M(g{-}i) = M(g{-}i|\tau, Z)$ is the absolute magnitude as a function of color, calculated from an isochrone of a given age τ and metallicity Z. The isochrone is only for main sequence stars, i.e. we ignore other evolutionary phases. Although Equation (4.2) looks somewhat complicated, the important portion is the $g-(M(g-i)+d)$ term, which controls the shape of the template. The Gaussian portion simply gives the template some width in apparent magnitude. An example of the best-fitting template is shown in the bottom right panel of Figure 4.6 for the brighter feature in the north.

In order to determine the distance to each feature, we found the distance modulus that maximized the normalized cross-correlation (NCC) between the feature f and the template t. The NCC is an established technique for image template matching (Briechle & Hanebeck, 2001). We already know which pixels belong to candidate features, and use the cross-correlation to assess the goodness of fit. A benefit of this method is that it penalizes features with only a few pixels, and those that do not resemble a main sequence. The normalized cross-correlation is given as

$$NCC = \frac{1}{N}\sum_{g-i,g}\frac{(f(g-i,g)-\overline{f})(t(g-i,g)-\overline{t})}{\sigma_f\sigma_y} \tag{4.3}$$

where $f(g-i,g)$ and $t(g-i,y)$ are CMDs for the feature and template, respectively. N is the number of pixels, and $\overline{f}$, $\bar{t}$, σ_f, σ_t are the respective means and standard deviations.

While finding the best-fitting distance modulus, the values for σ, τ, and Z were kept fixed at 1 mag, 1 Gyr, and 0.005 respectively. We found that the best fit value of d was not dependent on the choice of σ or τ. The value of σ controls the width of the feature, but not the peak location, which determines the distance modulus. An age of 1.0 Gyr is relatively young for MW disk stars, but was necessary to produce a main sequence stars that were as blue as observed. This is likely due to the extinction effects described in §4.7.4. Age has no appreciable effect on the main sequence of the isochrone after 1 Gyr, and therefore age does not affect our distance measurements.

The fitting algorithm is not sensitive to metallicity, introducing a source of systematic uncertainty in our distance estimates. For a given color, lower metallicity stars are less luminous. An underestimate of the metallicity results in an underestimate of the distance, and vice versa. We are unable to constrain the metallicity largely because *grizy* CMDs are not very sensitive to metallicity without the addition of a near-UV band (Ivezić et al., 2008). It is important to note that an uncertainty in the metallicities of the asymmetries does not affect our ability to detect them. Nor can it affect alternating north-south pattern of the asymmetries, which is indicative of a bending mode oscillation.

However, we are able to improve our distance estimates by making reasonable assumptions about the metallicities of the asymmetries. If the asymmetries are due to bending modes in the disk, they will not have a single metallicity, but rather some mean metallicity that is characteristic of their locations in the disk. After we made a preliminary map of the CMD features using a fixed metallically, it was straightforward to manually identify where individual features formed large scale asymmetries. We then adjusted the distances of each feature using the assumed metallically for the asymmetry to which it belongs.

Table 4.2. Disk Asymmetry Properties

Asymmetry	$\langle A\rangle$	R_{hel}	R_{gal}	Z	l	ϕ	Metallicity
				PS1 Catalog			
South Near	−0.10	1.0 - 1.9	7.7 - 7.8	−0.2 - −0.5	56.0 - 89.9	165.6 - 173.5	−0.5
North Near	0.17	1.4 - 2.8	8.9 - 9.9	0.4 - 0.8	59.2 - 239.0	139.6 - 191.9	−0.5
South MRi	−0.31	3.2 - 6.7	10.9 - 14.1	−1.0 - −2.1	122.0 - 238.9	156.7 - 203.2	−0.6
North MRi	0.25	7.0 - 11.3	14.2 - 18.5	3.3 - 5.4	84.6 - 236.7	116.9 - 212.4	−0.96
				Mock Catalog			
S1	−0.09	1.5 - 4.4	5.4 - 6.9	−0.3 - −1.0	2.2 - 76.4	155.2 - 179.2	−0.5
N1	0.16	1.3 - 3.3	8.9 - 10.6	0.4 - 1.0	53.3 - 225.0	93.2 - 188.9	−0.5
S2	−0.30	4.0 - 6.3	11.6 - 13.8	−1.5 - −2.4	95.6 - 225.0	135.5 - 198.3	−0.6
N2	0.57	7.0 - 11.6	14.4 - 18.9	2.3 - 3.7	81.1 - 225.0	107.1 - 204.6	−0.96

Note. — For each asymmetry, the columns list the median asymmetry excess, the range in heliocentric radius, Galactocentric radius, height above the Galactic plane, Galactic longitude, Galactocentric azimuth, and the metallicity.

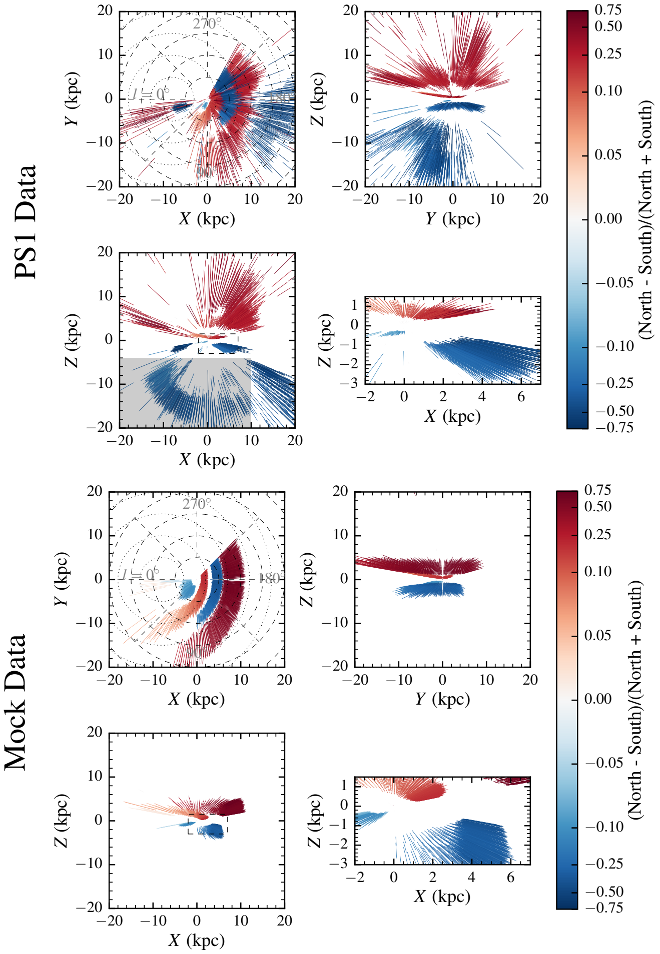

Figure 4.7 The spatial distribution of asymmetries identified in the PS1 catalog (top four panels) and mock catalog (bottom four panels). The maps are in Cartesian coordinates centered on the Sun. For each catalog, the top left panel shows the X-Y plane. Dashed circles indicate lines of constant heliocentric distance, with longitudes labeled. Dotted circles indicate lines of constant galactocentric distance, assuming the Sun is 8 kpc from the Galactic center. Top right and bottom left: Views in the Z-Y and Z-X planes. Bottom right: A zoomed in view of the region outlined in the bottom left. Each line corresponds to a feature identified in a residual CMD. The color indicates the excess number of stars in the features. The PS1 data contain a series of asymmetries in the MW disk over a large area. The observed asymmetries are qualitatively similar in many respects to the mock galaxy with bending mode perturbations in the midplane. The southern arm of the Sagittarius stream in the grey box (lower left panel, PS1 data) has been excluded from the top left panel.

4.5 Maps of the Asymmetric MW

In Figure 4.7, we map the 3D distribution of asymmetric features identified in the residual CMDs. The top set of panels are for the PS1 data. The bottom set of panels are for the mock catalog that we introduce in §4.6. For each dataset, the top left, top right, and bottom left panels show the heliocentric $X-Y$, $Z-Y$, and $Z-X$ locations of the identified features, respectively. The bottom right panel is a zoom-in of the bottom left, focusing on the asymmetries close to the plane. In this coordinate system, the Galactic center located at $(X, Y, Z) = (-8.0, 0, -0.0025)$ kpc, and the $+Z$ axis points towards the North Galactic Pole. The dashed black circles in the top left panel indicate constant lines of heliocentric distance, while the dotted gray lines indicate the same for Galactocentric distance. Lines of constant Galactic longitude are labeled for reference.

The red and blue lines in Figure 4.7 correspond to individual features identified in the residual CMDs. We refer to a *feature* as an individual main sequence-like feature in a single residual CMD, while we refer to an *asymmetry* as a coherent collection of many features over large area. Each line is centered at the distance corresponding to the distance modulus of the best-fitting isochrone template. The length of each line corresponds to the median width of the feature in apparent magnitude. The color of each line corresponds to the asymmetry excess defined in Equation 4.4 below. A positive excess of stars are red, and are plotted above the plane. The opposite applies to the negative, blue features. The colorbar is on a logarithmic scale. The maps only include features with NCC > 0.5 in order to exclude spurious features caused by noise or extinction.

The asymmetries span a large range of Galactic heights, and therefore a large range of stellar number densities. In order to better compare the asymmetries, we compute the asymmetry excess A as

$$A = \frac{N_N - N_S}{N_N + N_S} \tag{4.4}$$

where N_N and N_S are the number of stars in pixels of the northern and southern CMDs that define the feature. Values of A near zero indicate a small overdensity asymmetry, while values of A near ±1 indicate a large overdensity asymmetry.

We can only map asymmetries over the range of longitudes with overlapping PS1 survey coverage (see § 4.2.3). The sharp termination of asymmetries at $l \approx 240$ is due to the cutoff of the PS1 survey footprint. In contrast, the termination of the asymmetries at lower longitudes is not due to the PS1 survey footprint, which extends out to $l \approx 0$. We discuss this termination further in §4.7.1.

4.5.1 Four Asymmetries MW Disk

We first draw attention to the three arc-like asymmetries that extend from roughly 0 to 10 kpc in heliocentric distance. In order of increasing Galactocentric distance, the three asymmetries are the north near asymmetry, the south MRi, and the north MRi. These asymmetries were introduced in §4.3 and are visible in the CMDs in Figure 4.5. The south and north MRi overlap significantly in the $X - Y$ plane. The north MRi appears to spur outwards between $Y = 0 - 8$ kpc. As discussed below, this spur is actually the northern portion of the Sagittarius Stream. The projection effect of the map makes them appear to overlap.

A fourth asymmetry is visible in Figure 4.7, centered at (X, Y, Z) = (0.5, 2.0, 0.4) kpc. We refer to this as the south near asymmetry. The asymmetry is not visible in the CMDs of the SEGUE fields (§4.3) because it is outside of the SEGUE longitude range. Figure 4.8 shows representative CMDs for a north-south sightline pair containing the south near asymmetry. In contrast to the other asymmetries, the south near feature does not appear as a well defined main sequence in the southern CMD. However, there is a clear difference between the northern and southern CMDs. There are more bright stars in the south, and more faint stars in the north, which correspond to the north near asymmetry. This demonstrates an advantage of the residual CMD technique. A low overdensity feature such as the south near feature could go unnoticed in the original CMDs.

Table 4.2 summarizes the properties of the four asymmetries discussed above. The bottom set of values were determined from the mock catalog discussed in §4.6. For each asymmetry,

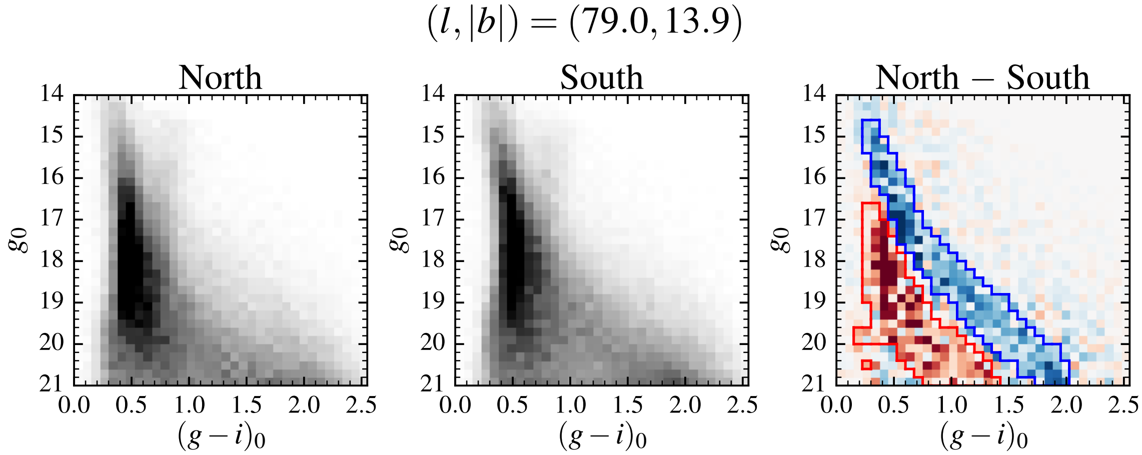

Figure 4.8: Representative CMDs for a north-south sight line pair containing the south near asymmetry discussed in $4.5.1. There is a small but clear difference in the magnitude distribution of the two CMDs. The feature outlined in blue in the right panel is caused by the south near asymmetry, and the feature outlined in red is caused by the north near asymmetry.

the table contains the median asymmetry excess, the range of heliocentric radius, galactocentric radius, galactic height, galactic longitude, and galactocentric azimuth ϕ, as well as the assigned metallicity for distance determination. Here $\phi = 180°$ points towards the Sun. These asymmetries suggest the presence of a bending mode oscillation in the MW disk, which we discuss in §4.7.1.

At the faintest magnitudes, the magnitude width of features is set by the photometric uncertainty of the PS1 survey, and so the distance range of the north MRi is an upper limit. At brighter magnitudes, the photometric uncertainty is smaller, and so the other asymmetries (south MRi, north near, and south near) are in fact extended over hundreds to thousands of pc. This was confirmed by inspection of globular and open cluster CMDs, which are only 1-2 pixels wide due to photometric uncertainty (all stars are effectively at the same distance), compared to the asymmetries, which are typically 5-10 pixels wide.

The asymmetries were assigned metallicities based on values and models in the literature. Using SDSS spectra, X15 measured [Fe/H] $= -0.5$ for the north near feature, and we used that value for our asymmetry mapping. X15 found that the metallicity of the south MRi varied with latitude, from approximately [Fe/H] $= -0.4$ at $b = -10^\circ$ to [Fe/H] $= -0.9$ at $b = -30^\circ$. We used [Fe/H] $= -0.6$ as an approximate mean value for the south MRi. For the north MRi, we used [Fe/H] $= -0.96$ (Li et al., 2012). The south near feature does not have a published metallicity, so we assumed [Fe/H] $= -0.5$ as typical for that height above the Galactic plane. We stress that the choice of metallicities determines the absolute distances to the asymmetries, but not their relative distance order, the latter of which is indicative of a bending mode perturbation.

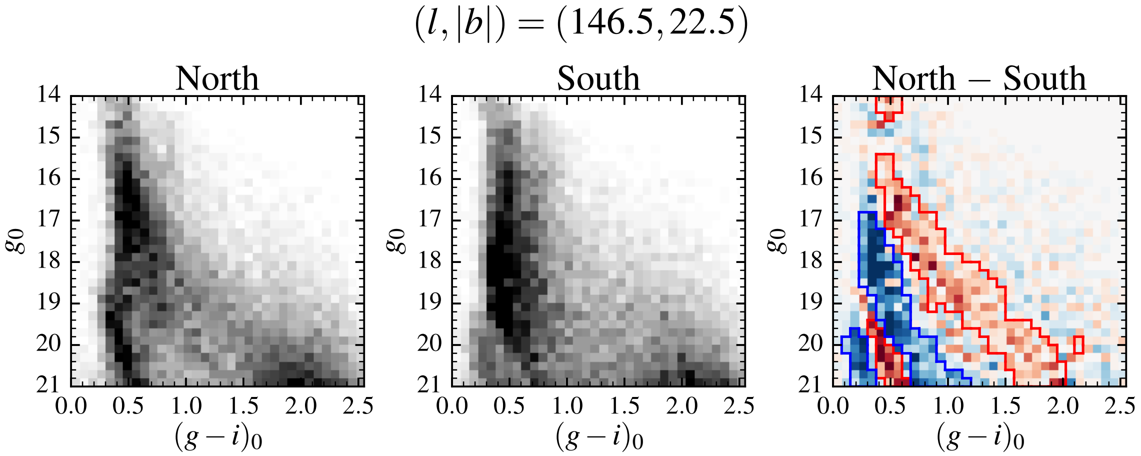

Figure 4.9: Representative CMDs for a north-south sight line pair containing the asymmetry discussed in §4.5.2 that is potentially associated with the TriAnd. The feature associated with the TriAnd is outlined in blue in the bottom left corner of the right panel. The asymmetry is near the PS1 flux limit, and is difficult to characterize.

4.5.2 Additional Asymmetries

Several other asymmetries are visible in Figure 4.7 that warrant some discussion. Further from the Galactic center than the MRi, an asymmetry is located at (X,Y,Z) = (16,−4,−10). This asymmetry appears to be related to what X15 associated with the TriAnd. Figure 4.9 shows representative CMDs for one of the sight line pairs where this feature is the strongest. There are two issues that limit our ability to detect and characterize this asymmetry. First, the feature has a very faint apparent magnitude, near the flux limit of the PS1 survey. Second, as was discussed in §4.3, this southern asymmetry overlaps with the north MRi in color-magnitude space in some sight lines. The north MRi has greater star counts, so we do not detect the southern asymmetry. The second issue could be resolved by fitting isochrones directly to the southern CMDs, rather than the residuals. We are interested in the inner disk asymmetries, and do not attempt such an analysis in this work.

Both the northern and southern portions of the Sagittarius Stream are present in Figure 4.7. The northern portion of the stream is visible above the MRi at $Z \approx 10$ kpc. The southern portion of the stream is outlined by the gray box in Figure 4.7. We excluded the southern portion from the $X - Y$ plot to better focus on the disk asymmetries. It is encouraging that we detect the Stream using our technique. However, we only detect the main sequence turnoff stars near the PS1 flux limit, so the spatial structure of the stream is not well constrained. An in-depth analysis of halo substructure using PS1 photometry is presented by Bernard et al. (2016).

There are some features in Figure 4.7 that are not associated with any of the asymmetries discussed above. In a handful of cases, the feature identification algorithm locates globular clusters. Although globular clusters are not the focus of this work, it is encouraging that the algorithm can identify them. In a sense, globular clusters are what the algorithm is designed to find: asymmetric features in residual CMDs that resemble main sequences. In two other cases, the algorithm identifies asymmetries that are caused by extinction, located at (X,Y,Z) = (−6, −2, -2) and (−14, −4, 4), We discuss how extinction affects our asymmetry analysis in

§4.7.4, but stress that the other asymmetries discussed previously are not due to extinction.

4.6 A Toy Model For Bending Modes

In the previous section, we presented maps of four asymmetries in the MW disk. Now we present a toy model galaxy with bending mode oscillations in the midplane. We generated a mock photometric catalogs for the galaxy, as well as a control galaxy with a standard double exponential density profile. The catalogs are analogous to what would be observed by a survey within the given galaxy. By running our automated asymmetry analysis on the mock catalogs, we can determine whether the toy model is qualitatively consistent with our observations.

4.6.1 Mock Catalogs

The *galfast* program (Jurić et al., 2008; Juric et al., 2010) generates mock photometric catalogs for galaxies with user defined models for the stellar density distribution, luminosity function, metallicity distribution, color-luminosity relationship, as well as photometric uncertainties. Although *galfast* can also include a 3D extinction model, we did not include it in order to avoid the added complication in interpreting our results. We generated mock catalogs over an area analogous to the PS1 sample area discussed in §4.2.3. In that way, we can better understand how the PS1 survey footprint affects our asymmetry analysis.

As a control, we generated mock catalogs for a standard MW-like galaxy without bending mode oscillations. The galaxy contained two components: a thin disk and thick disk. We did not include a halo or bulge because we are only interested in the disk. The thin and thick disk number density profiles were given as a double exponential:

$$n(R, Z, M) = fLF(M)\exp\left(-R/h_R - Z/h_Z\right) \tag{4.5}$$

where R and Z are the cylindrical Galactocentric radius and height above the Galactic plane, M is the absolute magnitude, h_R and h_Z are the scale length and scale height, f is a scaling factor between the thin and thick disk, and $LF(M)$ is the luminosity function. The observer

(Sun) is located at $(R, Z) = (8000, 25)$ pc. As discussed in §4.7.3, the location of Sun has a small but detectable effect on the asymmetry analysis.

The mock galaxy with bending mode oscillations also had a thin and thick disk component, but with a modified density profile. The profile was adapted from Xu et al. (2015), and are given as

$$n(R, Z, M) = fLF(M)\exp\left(-R/h_R - |Z - Z_w|/h_Z\right) \tag{4.6}$$

where Z_w is the height of the sinusoidally perturbed midplane given as a piecewise function.

$$Z_w(R) = \begin{cases} A_1\left(\frac{R}{8\text{ kpc}}\right)^{\alpha}\sin\left(2\pi(R - \phi_w)/\lambda_w\right), & R \leq \phi_w + \lambda_w \\ A_2\sin\left(2\pi(R - \phi_w)/\lambda_w\right), & R > \phi_w + \lambda_w \end{cases} \tag{4.7}$$

where A_1 is the amplitude of the inner wave at 8 kpc, A_2 is the amplitude of the outer wave, λ_w is the wavelength, ϕ_w is a phase offset from the Galactic center, and α is the power to which the amplitude of the inner wave increases with R.

The parameters for the density profiles are listed in Table 4.3. Values for f, h_R, and h_Z are taken from Jurić et al. (2008). Values for A_1, A_2, α λ_w, and ϕ_w were chosen to match the observed asymmetries in §4.5.1. Figure 4.10 shows the perturbed midplane Z_w as a function of galactocentric radius R. The midplane of both the thin and thick disks oscillate with a constant wavelength and an amplitude that increases with Galactocentric distance up to $R = \phi_w + \lambda_w$, 15 kpc in this case. At this radius a second wave begins with a larger, constant amplitude. We found this second wave was necessary to reproduce the north MRi.

Given a density profile and luminosity function, *galfast* randomly draws stars for a given position on the sky to create an initial catalog of stars with positions and absolute magnitudes. The luminosity function is based on the Jurić et al. (2008) analysis of SDSS data. From their positions, stars are assigned metallicities from the model of of Ivezić et al. (2008, Eq. 18 - 20), using the best-fit parameters in that paper. Given absolute magnitudes and metallicities, *galfast* then determines the stars' colors in the specified photometric system. From the positions, absolute magnitudes, and colors, it is then trivial to calculate the apparent magnitude in each filter. Finally, noise is added in the form of photometric errors.

Table 4.3. Mock Catalog Galaxy Parameters

Parameter	Value	Units
Thin Disk		
f	0.88	
h_R	2150	pc
h_Z	245	pc
Thick Disk		
f	0.12	
h_R	3261	pc
h_Z	794	pc
Bending Mode		
A_1	50	pc
A_2	1.5	kpc
λ_w	7	kpc
ϕ_w	8	kpc
α	3.5	

Note. — The bending mode model has the same thin and thick disk parameters, with the addition of a sinusoidally perturbed midplane described in Equation 4.7.

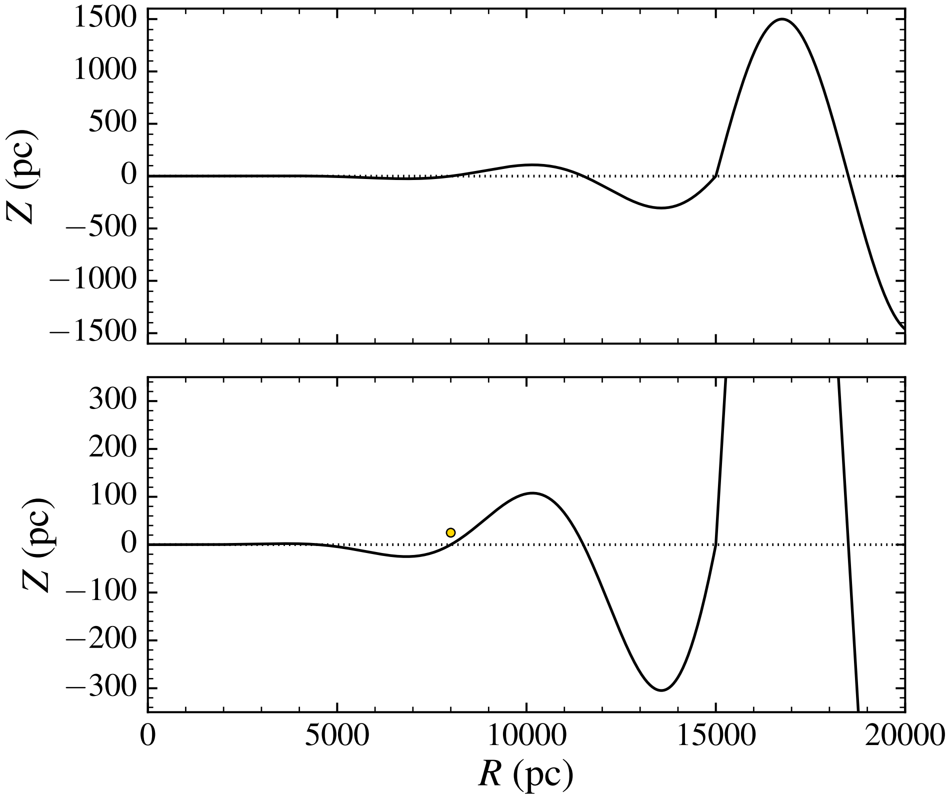

Figure 4.10: Top panel: The midplane radial wave model in Equation 4.7, with the parameters in Table 4.3. Bottom panel: A zoom-in of the top panel. The location of the Sun is indicated by the yellow circle.

Like the luminosity function, the color-metallicity-magnitude relation and photometric uncertainties were determined from the SDSS-based results of Jurić et al. (2008). Therefore, we used isochrones in the SDSS photometric system when fitting template CMD features in the mock catalogs. The SDSS and PS1 photometric systems are very similar, and the mock catalogs are suitable qualitative comparison to the PS1 observations. Furthermore, the relevant element of the mock catalogs are the density profiles, which are independent of the photometric system.

4.6.2 Asymmetries in the Mock Catalogs

The bottom set of panels of Figure 4.7 show the asymmetries identified in the bending mode mock galaxy. Four asymmetries are visible, extending from roughly 5 to 19 kpc in galactocentric radius. For convenience, we label these features as S1, N1, S2, and N2 in order of increasing galactocentric radius. Table 4.2 lists the properties of these asymmetries. The asymmetries in the mock catalog were assigned the same metallicities as their observed counterparts for the purposes of comparison. Unlike for the PS1 data, no halo substructure is visible because we did not include a halo component in our model.

The control mock galaxy without a midplane wave lacks the alternating north-south asymmetries, as is expected. However, there are two asymmetries in the mock catalog caused by the offset of the Sun from the Galactic plane. In §4.7.3, we argue that the observed south near asymmetry is not due to the vertical offset of the Sun.

4.7 Discussion

4.7.1 Evidence for Bending Modes in the MW Disk

The the observed and mock asymmetries share many key properties, including their locations, spatial extent, and asymmetry factors. While there are some some exceptions we discuss below, the two datasets agree quite well. The asymmetries alternate below and above the midplane, with heights that increase with galactocentric radius. To first order, the observed asymmetries are consistent with a bending mode oscillation in the MW midplane.

The simulated and observed asymmetries span similar ranges in longitude. As was noted in §4.5.1, the PS1 survey footprint lacks overlapping north-south coverage beyond $l \approx 240°$, causing the sharp termination of the features. This termination was also replicated in the mock data. More interestingly, both the observed and mock asymmetries appear to terminate towards lower longitudes, even though the bending mode toy model extends around the entire galaxy. We visually inspected the observed and mock CMDs, and confirmed that the asymmetric features are not visible at lower longitudes. This is likely a geometric effect. As we look roughly tangent to the circular asymmetries, the stars become more spread out in apparent magnitude, and are not visible as asymmetries in the residual CMDs.

On a finer level, there are some differences between the observed and mock asymmetries. The observed asymmetries have more irregular edges, which may be due in part to uncertainties caused by extinction. Unlike the toy model, the observed asymmetries are not axisymmetric, as was also noted by X15. Our toy model is phenomenological, and was not intended to include more complex underlying physics. Three independent radial velocity surveys have shown evidence for breathing mode oscillations (compression-rarefaction) in the MW, in addition to bending mode perturbations (Widrow et al., 2012; Carlin et al., 2013; Williams et al., 2013). These breathing modes may account for some of the differences between the observed and mock asymmetries. However, the overall qualitative agreement is good, providing additional evidence for bending mode perturbations in the MW over a much larger area than previous studies.

4.7.2 The Monoceros Ring

The differences between the north MRi and corresponding mock N2 asymmetries may offer some insight as to the nature of the north MRi. While both asymmetries have similar radial extents, the north MRi has a mean height of roughly 4.4 kpc, compared to roughly 3.0 kpc for the N2 asymmetry. Meanwhile, the median asymmetry factor of the north MRi is 0.25, less than half that of N2. Increasing the amplitude of N2 would further increase its asymmetry factor, as more of the disk goes above $Z = 0$. Given its height, the north MRi has too small an asymmetry factor to be fully consistent with our toy midplane wave model.

This issue could potentially be resolved by including additional elements in our midplane wave model, such as a disk flare or breathing mode oscillations in addition to bending modes. On the other hand, the north MRi may not be related to asymmetries at smaller radii. While it is tempting to tie the south and north MRi together, Morganson et al. (2016) remark that the south MRi is contiguous with the disk, while the north MRi could be a separate structure. Although our results do not allow us to make a definitive statement on this issue, it is intriguing that our toy model reproduces the properties of the other asymmetries, but not the north MRi.

4.7.3 The South Near Asymmetry

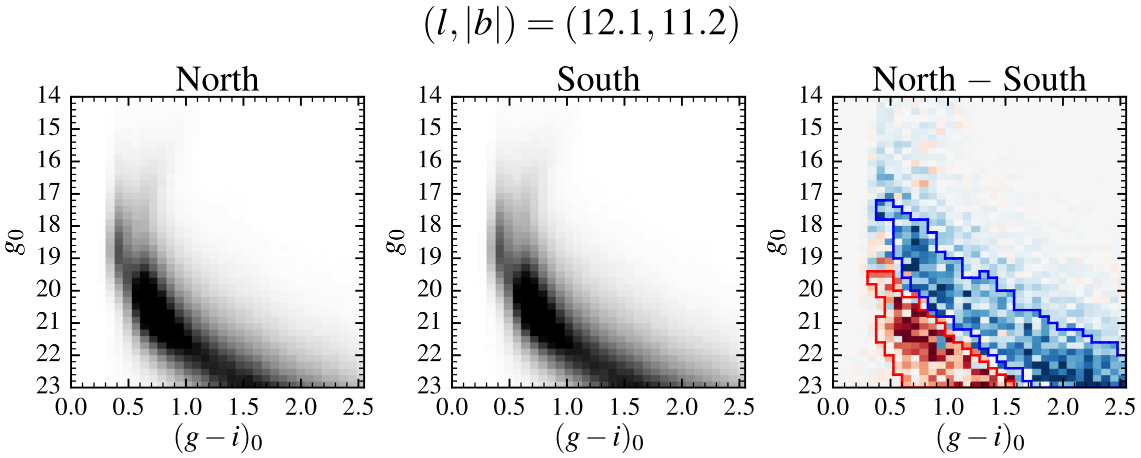

Figure 4.11: Representative CMDs for a north-south sight line pair containing the Sun vertical offset-related asymmetry discussed in §4.7.3. Unlike the observed south near asymmetry (Figure 4.8), the northern and southern CMDs are nearly identical, but are offset slightly in apparent magnitude due to the vertical offset of the Sun from the Galactic plane.

There is an asymmetry in the mock catalog for the control galaxy without bending modes, but it is different than the south near asymmetry, and it is unlikely that the south near asymmetry is due to the vertical offset of the Sun from the Galactic plane. In the CMDs for the observed south near asymmetry (Figure 4.8), there is a clear north-south difference in the apparent magnitude distribution. There are more bright stars in the south, corresponding to the south near asymmetry. There are more faint stars in the north, corresponding to the north near asymmetry, which is further from the Sun. In contrast, the north and south mock CMDs (Figure 4.11) are nearly identical. They are offset slightly in apparent magnitude due to the vertical offset of the Sun, which causes a north-south asymmetry in the residual CMD.

Previous observational studies also support the presence of a nearby southern asymmetry. Widrow et al. (2012) first reported an asymmetry in stellar number counts from ∼0.3 - 0.5 kpc below the Galactic plane, using SDSS photometry. This height range agrees well with our values for the south near asymmetry. Yanny & Gardner (2013) confirmed the asymmetry with an extended analysis that ruled out systematic sources of the uncertainty, including the vertical offset of the Sun. We conclude that the south near asymmetry is not due to the Sun offset based on the results from our mock catalogs and previous studies.

4.7.4 Extinction Effects

Extinction presents two issues with our analysis, although neither change the significance of the asymmetries we observe, or our fundamental conclusions. The first issue is that extinction could cause us to falsely infer the presence of an asymmetry even though the underlying stellar density distribution is symmetric. Second, extinction is a source of uncertainty when characterizing a genuine asymmetry.

The four observed disk asymmetries cannot be caused by extinction, due to the way extinction moves stars in color-magnitude space. Figure 4.12 shows CMDs for four north-south sight line pairs, as well as their difference. The yellow arrows indicate the direction that stars move in the CMD due to extinction. As X15 argue, extinction moves stars nearly along the main sequence, and cannot concentrate stars in apparent magnitude to produce the observed overdensities. In other words, the stars in the south MRi (below plane) are consistently fainter than the north near structure (above plane). This is the case in all four sight lines in Figure 4.12, even though two sight lines have more extinction in the north, one has more in the south, and in one they are equal. An analysis of line-of-sight stellar densities by Morganson et al. (2016) also confirmed that the south MRi is closer to the Sun than the north MRi. It is therefore highly unlikely that the underlying stellar density distribution is north-south symmetric, and that errors in the SFD extinction corrections could conspire in such as way as to create multiple asymmetries over $\sim 180°$ of Galactic longitude. As discussed below, extinction does cause problems when determining the properties of the asymmetries

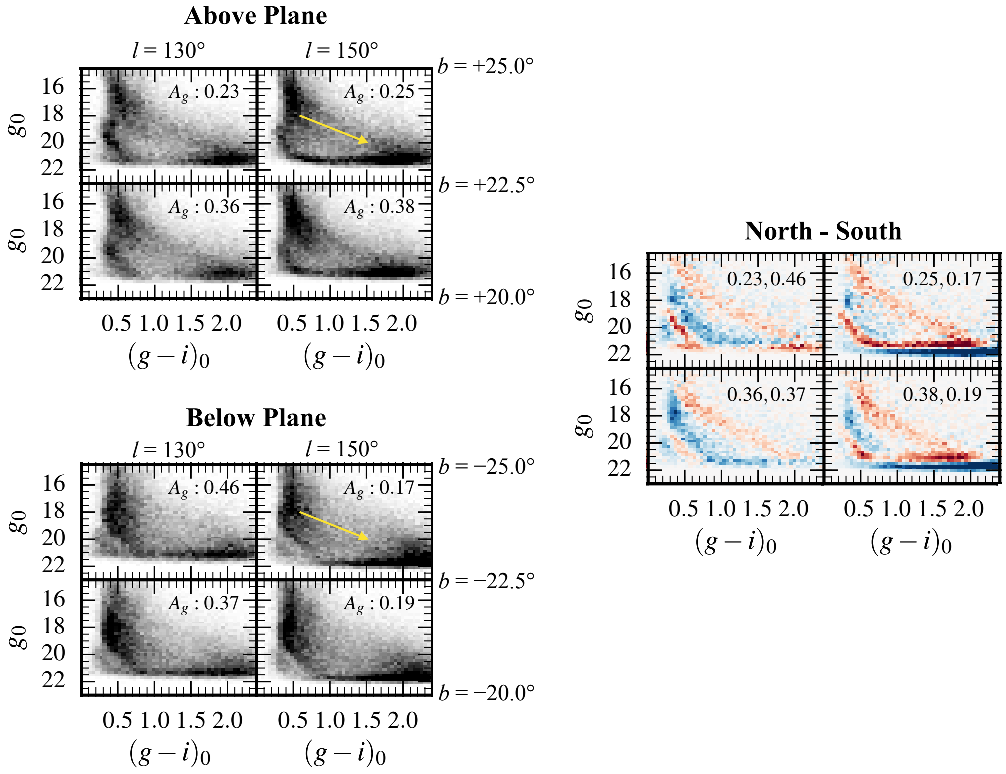

Figure 4.12: CMDs for four sight lines above the plane (top left panels), below the plane (bottom left panels) and the difference (right panels). The reddening vector is indicated by the yellow arrows.

(i.e. the MSTO color). Finally, the uncertainty about the the possible influence of extinction will be eliminated by direct parallax measurements soon to be provided by Gaia.

In other parts of the sky, extinction introduces spurious asymmetries, but they can be easily rejected based on their appearance in the CMDs. In §4.5.2, we noted two spurious extinction-related asymmetries located at (X,Y,Z) = (−6, −2, −2) and (−14, −4, 4) in Figure 4.7. A representative residual CMD for these spurious asymmetries is shown in Figure 4.13. The features do not appear like main sequences, and are caused by the combined effects of inaccurate extinction corrections and the faintness limit issue described below. These extinction-related features only span a few pixels in color-space. Therefore the identification

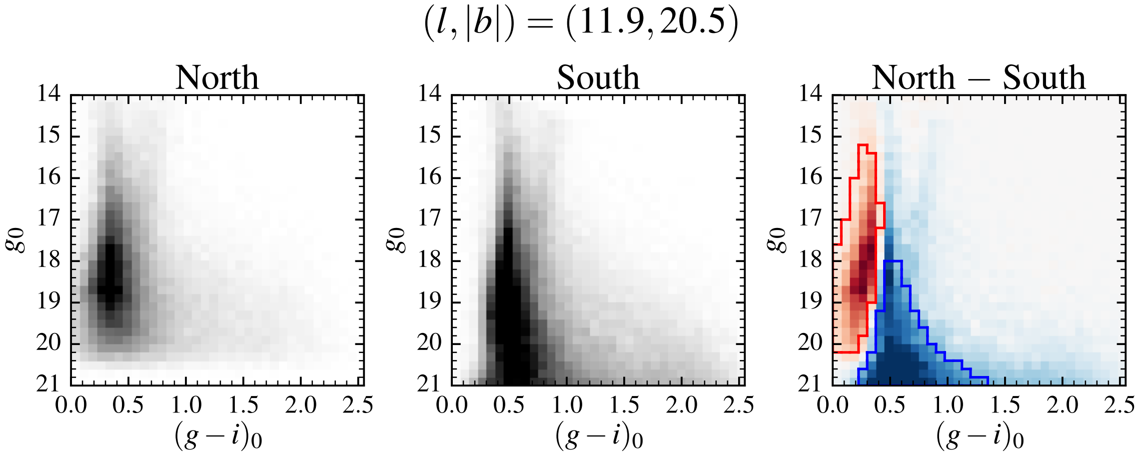

Figure 4.13: Representative CMDs for a north-south sight line pair containing the extinction-related asymmetry discussed in §4.7.4. The asymmetry is caused by the different amounts of extinction in the two sight lines, and a miscorrection for extinction. Such asymmetries do not resemble the genuine main sequence-like asymmetries, and can be rejected from our analysis.

algorithm has a limited ability to distinguish these extinction related features from true asymmetric features (e.g. the north MRi and Sagittarius Stream) that also span a narrow number of color bins. Fortunately, we can disregard these extiction-related asymmetries based on a by-eye inspection of the residual CMDs.

In highly extincted sight lines, extinction is a source of uncertainty in our characterization of the asymmetries. This effect can be seen by following the residual CMDs in Figure 4.5 at $l = 130°$ from high to low latitudes. At higher latitudes, the extinction is relatively small, both in terms of the absolute amount and the north-south difference. In the higher latitude CMDs, the features are well defined and resemble main sequences. Below $l = 15°$, there is much more extinction in the north than in the south, and the features do not resemble main sequences. The mapping algorithm could determine the incorrect distance if the extinction correction is wrong. The algorithm could also infer the incorrect asymmetry excess, because the CMD distributions are misaligned. We have largely avoided these issues by excluding sight lines below $|b| < 10°$, but the properties of asymmetric features in highly extincted sight lines should be regarded as more uncertain. Fortunately, the properties of all four disk asymmetries in this work are well constrained by a large number of low extinction sight lines.

As a final issue, extinction limits the faintest asymmetries we can detect. As an example, for the sight lines in Figure 4.12, the median g_{P1} extinction is 0.18 mag in the north, and 0.81 mag in the south. We incorrectly infer an excess of stars in the north, because we did not detect the corresponding stars in the south. This effect is also visible in the SEGUE CMDs in Figure 4.5 where there are large north-south differences in extinction, as indicated in the upper right corner of the panels. To avoid this issue, we truncated our CMDs at $g_0 = 21$ mag. This work is concerned with asymmetries in the inner MW disk, for which $g_0 = 21$ mag is a more than sufficient flux limit.

4.8 Summary

We have analyzed PS1 photometry over half of the sky for the presence of asymmetries in the MW disk. Prior to our analysis, we prepared the PS1 catalog to account for systematic effects that could bias our asymmetry analysis. We then produced CMDs for the SDSS SEGUE fields, demonstrating that a radial wave-like asymmetry is present over a large range of longitudes. Next, we developed a novel technique to automatically identify and characterize asymmetric features in residual north-south CMDs. We presented a toy model galaxy with bending mode perturbations, and generated a mock photometric catalog as if the galaxy were being observed from within.

Our key findings are:

1. At least four asymmetries exist in the MW disk from 7.7 to 18.5 kpc in galactocentric radius. 0.2 - 5.4 kpc in height from the Galactic plane, and 56.0 to 239.0 degrees in Galactic longitude. In order of increasing galactocentric distance, these are asymmetries are the south near, north near, south MRi, and north MRi. Thus a large portion

of the outer Milky Way disk is asymmetric at the 10 to 30% level in terms of the overdensity of star counts relative to the mean.

2. The mock catalog generally reproduce the locations and spatial extent of the observed asymmetries. A bending mode oscillation appears qualitatively consistent with the south near, north near, and south MRi asymmetries.

3. The Galactic height and star count overdensity of the north MRi do not appear to be consistent with a purely bending mode oscillation, supporting previous suggestions that it may be a separate structure from the south MRi.

Chapter 5

CONCLUSION

5.1 Summary

Low mass main sequence stars are by far the most abundant type of star in the Milky Way. They provide the longevity and stability required for complex life to develop, but can also threaten habitability through rotation-driven magnetic activity. This activity also influences the evolution of the star, by slowing its rotation rate. Complicating matters, roughly half of low mass stars have at least one bound companion, and of those about 20% are close enough to influence the star at some point in its evolution. Thus, understanding low mass stars requires studying their rotation, activity, and binary interaction.

Chapters 2 and 3 of this thesis focused on the behavior of stars using photometry from the *Kepler* space telescope. *Kepler* has opened a new window into stellar astrophysics though its unprecedented photometric precision, high cadence, and long time baseline.

Chapter 2 studied a system containing two fully convective M dwarfs, GJ 1245 A and B. Because there is no interface with a radiative core, fully convective M dwarfs are expected to have a different magnetic dynamo mechanism than stars like the Sun. GJ 1245 A and B have nearly the same mass, and by virtue of being in a binary, have the same age. However, star A rotates nearly three times faster than star B. The system is a crucial benchmark for the dependence of activity on rotation in the fully convective regime.

The challenge of the project was that the angular separation of the stars was just at the limit of *Kepler's* spatial resolution. The solution was to generate separate light curves for each star, and to ensure that there was minimal cross contamination between the stars. This allowed the subsequent analysis of starspot modulations and flares.

The stars emit nearly equal fractions of their total luminosities in flares, despite one star rotating nearly three times faster than the other. This suggests that the stars are rotating faster than some threshold rate, above which activity no longer depends on rotation. It was also found that the slower rotating star has a higher amount of differential rotation, which is consistent with previous observations and models.

Chapter 3 analyzed over 2000 eclipsing binary (EB) light curves in order to measure rotation periods. Close binaries interact via tides so that the orbit becomes circular, and the rotation of the stars becomes coplanar and synchronized to the orbital period. This project is important because there were very few existing measurements of the synchronization of stars with convective envelopes.

The challenge was identifying which EBs have starspot modulations, because there are other types of out-of-eclipse variability. Based on visual classification of the light curves, 816 out of the 2278 EBs in the sample had unambiguous starspot modulations, for which rotation periods were measured.

At orbital periods below 10 days, over 90% of the EBs are synchronized, as was expected because of the strong tidal effects at close separations. An unexpected result was that 15% of EBs with orbital periods between two and ten days have rotation periods that are about 13% slower than the synchronous value. After ruling out instrumental or numerical sources, a scenario was presented in which stars in the subsynchronous cluster are in fact synchronized to the rotation period at the equator, but the starspot modulation originates from higher, more slowly rotating latitudes. This provides a novel test case for models of differential rotation in rapidly rotating, tidally interacting systems.

Another important result was the identification of a transition period at roughly ten days from predominantly circular, synchronized EBs to eccentric, pseudosynchronized EBs. The transition occurs because binaries below ten days circularize during the pre-main-sequence phase, with only minimal circularization at longer periods on the main sequence.

In Chapter 4, the focus shifted from the behavior and interaction of low mass stars to their overall distribution in the Galaxy, using photometry from the recently completed PanSTARRS survey. PanSTARRS is important because it covered the entire Galactic disk, which no deep, wide-area optical survey had done before.

Across 180 degrees of galactic longitude and 11 kpc of galactic radius, there are four ring-like asymmetries at the 10-30% level relative to the mean stellar number counts. This view of the disk is dramatically different than the traditional, simplified model of a smooth, vertically symmetric stellar distribution. The observed asymmetries are qualitatively similar to a mock galaxy model with a perturbed midplane, suggesting that interactions with satellite galaxies may have induced oscillations in the disk.

As a whole, this thesis brings together two different approaches to observing low mass stars. On one hand, stars are distinct astrophysical objects whose magnetic activity, rotation, and binary interaction can be studied with time domain photometry. On the other hand, stars are tracers of Galactic structure that can be mapped with wide field surveys. In both cases, advances in detector and computing technology have enabled low mass stars to be studied in larger numbers and with greater precision than ever before.

5.2 Future Prospects

In this section, I describe several important ongoing or upcoming surveys and how those surveys will improve our understanding of low mass stars and the Galaxy as a whole.

5.2.1 Ongoing and Upcoming Surveys

Gaia

It is difficult to overstate the impact that the Gaia mission will have on stellar and Milky Way astrophysics. Launched in December 2013, the mission is scheduled to have its second data release in April of 2018. This data release will have broadband photometry, positions, and preliminary proper motions and parallaxes for a billion stars. It will also include radial velocities for millions of brighter stars. The Gaia dataset will be used to study the stellar number density distribution, kinematics, and chemical compositions.

K2

In 2013, the second of *Kepler's* four reaction wheels failed, and the spacecraft could no longer maintain the accurate pointing required for high photometric precision. The spacecraft was repurposed as the K2 mission. By keeping its focal axis parallel to the Sun's rays, K2 minimized the amount of torque from radiation pressure, and could maintain sufficiently accurate pointing to provide high quality light curves. This required pointing at fields along the ecliptic, and limited the length of a campaign to about 80 days. The change in observing strategy was beneficial in that it enabled *Kepler* to look at a more diverse population of stars at different galactic latitudes, as well as clusters. Creating new target lists also provided the opportunity to observe more M dwarfs than the original *Kepler* mission.

TESS

The Transiting Exoplanet Survey Satellite (TESS) is scheduled to launch in the first half of 2018. The primary goal of the mission is to discover transiting exoplanets around bright stars that will be suitable for spectroscopic characterization by the James Webb Space Telescope. As with *Kepler*, the photometry will also have many applications to stellar astrophysics. Looking at bright stars will also mean that followup of interesting stars will be easier than with fainter *Kepler* targets. The spacecraft will collect data for 200,000 "postage stamps" every two minutes, but will also download full frame images taken every thirty minutes. This is an improvement over *Kepler*, because it will enable long cadence observations for any bright object, not just preselected targets. In practice, this will be limited by confusion, because the camera has a very large pixel scale of $20''$/pixel. Another major difference from *Kepler* is that TESS will cover the entire sky, but will change pointing every 27 days. Most of the sky will only have 27 days of coverage, but continuous viewing zones near the ecliptic poles will have a full year of coverage.

ZTF

The Zwicky Transient Facility (ZTF) is a time domain survey based on a 1.2 m telescope at Palomar Observatory in southern California, and will begin regular survey operations in early 2018. The 600 megapixel camera covers 47 square degrees, allowing ZTF to average

300 visits per year across the entire northern sky in three optical and near IR filters. ZTF will image the Galactic plane on a nightly basis to an unprecedented depth, revealing the variability of previously uncharacterized disk stars. As a complement to LSST (see below), ZTF will identify brighter targets for which spectroscopic followup can be obtained on the large fleet of moderate sized northern telescopes.

LSST

Currently under construction at Cerro Pachón in Chile, the Large Synoptic Survey Telescope (LSST) is scheduled to start collecting data in the early 2020s. The 8 meter telescope will see fainter objects than any previous wide area survey, while a large field of view and rapid slewing means it can cover the entire sky (visible at a given time of year) every three days in six photometric filters from the near ultraviolet to the near infrared. With LSST, it will be possible to study stellar variability across more of the Galaxy than ever before.

Although these new surveys will provide enormous quantities of rich data, followup observations will be required to characterize interesting objects. In particular, photometry cannot replace spectroscopy for precise stellar abundances and binary orbital solutions. Even as we look ahead to an exciting future of large surveys, it is important for the astronomical community to dedicate resources for followup.

5.2.2 Combining Light Curves and Gaia Stellar Parameters

One of the most exciting avenues of stellar astrophysics research in the next decade will be the combination of precise light curves from *Kepler*, K2, and TESS with precise stellar luminosities and space motions from Gaia. This synergy will be important for both the age-activity-rotation relation of single stars and non-interacting binaries, as well as the tidal interaction of close binaries. Currently, most stars with precise light curves do not have accurate astrometry, and therefore have poorly constrained stellar parameters. Meanwhile, most stars with accurate astrometry (such as the Hipparcos sample) do not have *Kepler*-like light curves.

The Gaia data can be used to better characterize the subsynchronous binary population in

Chapter 3. There was no obvious distinction between the subsynchronous population and the main synchronized population based on the available stellar parameters. This supports the conclusion that the stars in the populations are physically similar, and the different rotation periods are due to different starspot distributions, perhaps related to activity cycles. However the stellar parameters used in Chapter 3 had large uncertainties and lacked astrometric data. Using the upcoming Gaia data, it can be tested whether the subsynchronous population is kinematically distinct from the rest of the sample, or is comprised of evolved stars.

The new surveys will also expand the existing parameter space of stellar mass and age. *Kepler* observed few fully convective stars due in large part to their intrinsic faintness, but also due to the mission's focus on Sun-like stars. In comparison to *Kepler*, TESS will have a redder bandpass and will target a larger number of fully convective stars. These new light curves can be used to test what effects the transition to full convection has on surface activity, magnetic braking, and tidal interaction.

As they have for decades, young clusters will continue to be vital age benchmarks. Unfortunately, open clusters have many fewer members than the field, so statistics may be biased by stochastic variations. This may be a fundamental limitation in gyrochronology (Barnes, 2003). Furthermore, the number of close binaries will necessarily be small. Fortunately, the accuracy and synoptic nature of Gaia should ensure that effectively all cluster members are identified, and the precision of *Kepler*, K2, and TESS will mean that any star for which the rotation period can be measured photometrically will be identified. Thus, these new surveys will make maximum use of what are one of the few natural astrophysical laboratories.

In parallel with these efforts, LSST will produce sparsely sampled light curves for billions of low mass stars. An LSST-based rotation period catalog will have greater uncertainties and biases than the space-based missions (Hawley et al., 2016), but this will be compensated to some extent by a much larger sample probing a greater volume of the Galaxy. However, it is in flare statistics that LSST offers the most promise, with tens to thousands of flare detections expected per square degree over the ten year survey, depending on galactic latitude (Hawley et al., 2016). Beyond their intrinsic value for stellar and Galactic astrophysics, it will be important to understand flares as contaminants in extragalactic transient surveys.

5.2.3 Disentangling the Disk with Gaia and LSST

In principle, if a stellar system is left to evolve independently for a long period of time, it will be become "relaxed" such that it is in equilibrium and has no memory of its formation (Chandrasekhar, 1942). The disk of the Milky Way is far from relaxed. About half of stars form with at least one stellar companion, and while the widest binaries have been disrupted over the lifetime of the galaxy, close binaries containing low mass stars will remain bound for trillions of years. Star formation is ongoing in clusters, and those clusters are being disrupted the Galactic tide and encounters with molecular clouds to join the field population. There are also a large variety of overdensities and asymmetries in the disk, which may arise from self-interaction, perturbations by satellite galaxies, or the tidal debris (gas and stars) of the satellites themselves.

The stellar distribution of the Milky Way (or any galaxy) can be described by a seven dimensional phase space that includes the three spatial dimensions, the three components of velocity, and the bulk metallicity (Ivezić et al., 2012). Binary stars, star forming clusters, and substructure all have unique signatures in this phase space. Gaia will produce by far the largest, most precise, and unbiased sample of this phase space.

At separations of a few AU or less, binaries can be identified by the presence of periodic eclipses, radial velocity variations, or astrometric perturbations. At larger separations, which includes the vast majority of binaries, the orbital periods are much longer than the current baseline of observations, and so wide binaries must be identified as having common proper motions and parallaxes. Ground based astrometric surveys have either have large uncertainties or small sample sizes, so the semi-major axis distribution of wide binaries is poorly constrained (Jiang & Tremaine, 2010). The large and precise Gaia sample will greatly improve this situation, enabling better models of wide binary disruption.

Star clusters are fundamental to our understanding of stellar structure and evolution. For dozens of nearby open clusters, Gala will provide individual stellar distances accurate to within 1% (Bailer-Jones, 2009). Combined with proper motions, it will be possible to map the structure and kinematics of open clusters, and therefore better understand how cluster dissipation populates the disk. The extremely precise HR diagrams for open clusters will reveal new details about how stellar rotation, activity, and multiplicity create intrinsic scatter in the main sequence.

On the largest scales, Gaia will be able to identify tidal debris that is spatially mixed with disk stars because the debris remains coherent in angular momentum and energy-space over gigayears, (Helmi & de Zeeuw, 2000; Bailer-Jones, 2009). Gala data promises to answer many of the unresolved questions about disk substructure discussed in Chapter 4. With accurate parallaxes, it will no longer be necessary to use color-magnitude diagrams to infer distances, so that 3D maps of the stellar density distribution and extinction can be produced simultaneously. In addition to distances, proper motions and radial velocities can be used to study the compression-rarefaction (breathing mode) components of disk-satellite interactions, in addition to the bending modes in Chapter 4.

As a complement to Gaia, which is limited to 20th magnitude, the final LSST catalog will be complete to magnitude 27.5, or 1000 times fainter. Applications of the LSST catalog will include tracing substructure in the distant halo, as well as a greatly expanded census of intrinsically faint, very low mass stars and substellar brown dwarfs. Current catalogs of such objects only reach a few tens of parsecs from the Sun, and so it is unknown if and how their mass distribution varies across the Galaxy.

5.3 Closing Thoughts

I will always remember the experience that led me to pursue an education in astronomy. When I began college, I registered for an introductory astronomy course to satisfy the science requirement for a degree in public policy. The course was interesting, but I would never have pursued astronomy further had the course not required me to visit the university's observatory outside of the city.

Stepping out of the car, I was struck by the sight of the Milky Way. Before visiting the observatory, I had only seen an unpolluted sky a handful of times on vacations with my family. The Milky Way had fallen into the same category as the Grand Canyon or Niagara Falls, a special sight that you had to travel to see, rather than something that was always there, even if obscured by city lights. Seeing the Milky Way this way was just a teaser for what was inside the observatory.

As I waited in line, the astronomer operating the telescope told me that it was pointed at a globular cluster. I had some idea of what this was from the introductory course, but I wasn't expecting what I saw through the eyepiece. There were an uncountable number of golden-white stars overfilling the eyepiece. It was almost impossible to imagine that these stars formed together billions of years ago, and remained bound together by their mutual gravitation, yet here it was in front of my eyes. Shortly after visiting the observatory I changed my academic major to astronomy, which ultimately led to this thesis.

The globular cluster story shows how direct contact with nature is a vitally important part of my approach to science. The stars are so far away that I'll never get to visit them, but at least I can have some of their photons hit my retinas. Modern astronomical research doesn't involve looking through an eyepiece, because our eyes (although marvelous feats of evolution) are not optimal detectors. As described in the Introduction, cutting edge astronomical surveys employ large arrays of digital detectors to collect massive quantities of data.

This thesis has used data from two of those surveys, but my "hands-on" approach is reflected in the analysis. Chapter 2 analyzed *Kepler* pixel-level data of GJ 1245 A and B, which was necessary to extract separate light curves of the stars. Chapter 3 involved the visual inspection and classification of nearly 3000 eclipsing binary light curves. Chapter 4 used an automated program to identify asymmetric features, but was designed to quantify what I had previously identified by eye. In all three investigations, I would not have been able to reach the conclusions that I did without first visualizing and inspecting the data.

As the size and complexity of survey datasets continues to increase, automated techniques such as machine learning are taking the place of human inspection. Automated techniques can analyze a larger volume of data faster and in more dimensions than is possible for a human. These techniques may be the only way to answer many of the questions raised earlier in this chapter, and will likely reveal unexpected patterns and phenomena as well. However, I worry that the sky may become less of a direct human experience and more of a statistical abstraction. Even as we increasingly rely on technology, I hope that this thesis demonstrates the benefits of looking more directly at the data.

5.4 Additional Acknowledgments

The research in this thesis was supported by funding from the Washington Research Foundation, the University of Washington Provost's Initiative in Data-Intensive Discovery, the University of Washington College of Arts and Sciences, NSF grants AST08-07205, AST13-12453, and AST13-11678, Kepler Cycle 2 GO grant NNX11AB71G, Cycle 3 GO grant NNX12AC79G, and NASA ADP grant NNX09AC77G.

Chapters 2, 3, and 4 made use of NASA's Astrophysics Data System Bibliographic Services, and the following Python software packages:

- Astropy (Astropy Collaboration et al., 2013)
- gatspy (VanderPlas & Ivezić, 2015; VanderPlas, 2016)
- h5py (Andrew Collette and contributors, 2008, `http://h5py.alfven.org`)
- IPython (Prez & Granger, 2007)
- kplr (Daniel Foreman-Mackey, `http://dan.iel.fm/kplr`)
- Large Survey Database (Juric, 2012)
- Matplotlib (Hunter, 2007)
- NumPy and SciPy (van der Walt et al., 2011)

- padova (Sick, 2015)
- Pandas (McKinney, 2010)
- scikit-image (van der Walt et al., 2014)
- SciPy (Jones et al., 2001–)

Chapter 2 used data from the Mikulski Archive for Space Telescopes (MAST) at the Space Telescope Science Institute. STScI is operated by the Association of Universities for Research in Astronomy, Inc., under NASA contract NAS5-26555. Support for MAST for non-HST data is provided by the NASA Office of Space Science via grant NNX13AC07G and by other grants and contracts. Chapter 2 used spectra obtained with the Apache Point Observatory 3.5-meter telescope, which is owned and operated by the Astrophysical Research Consortium. Data were reduced with PyKE (Still & Barclay, 2012), a software package for the reduction and analysis of Kepler data. This open source software project is developed and distributed by the NASA Kepler Guest Observer Office. Todd Henry and Fritz Benedict shared the orbital parameters for GJ 1245AC prior to publication. The NOAO archived 2011 observation of GJ 1245 was made on the WIYN 0.9m was made under the observing proposal of Steve Howell.

Chapters 2 and 3 used data collected by the Kepler mission. Funding for the Kepler mission is provided by the NASA Science Mission directorate.

Chapter 3 was improved by helpful suggestions from Brett Morris, Leslie Hebb, and Rory Barnes.

Chapter 4 used data from Pan-STARRS. The Pan-STARRS Surveys have been made possible through contributions of the Institute for Astronomy, the University of Hawaii, the Pan-STARRS Project Office, the Max-Planck Society, and its participating institutes, the Max Planck Institute for Astronomy, Heidelberg, and the Max Planck Institute for Extraterrestrial Physics, Garching, The Johns Hopkins University, Durham University, the

University of Edinburgh, Queen's University Belfast, the Harvard-Smithsonian Center for Astrophysics, and the Las Cumbres Observatory Global Telescope Network, Incorporated, the National Central University of Taiwan, the National Aeronautics and Space Administration under Grant No. NNX08AR22G issued through the planetary Science Division of the NASA Science Mission Directorate, the National Science Foundation under Grant No. AST-1238877, the University of Maryland, and Eotvos Lorand University F(ELTE).

Chapter 4 also used data from SDSS-III. Funding for SDSS-III has been provided by the Alfred P. Sloan Foundation, the Participating Institutions, the National Science Foundation, and the U.S. Department of Energy Office of Science. The SDSS-III web site is http://www.sdss3.org/. SDSS-III is managed by the Astrophysical Research Consortium for the Participating Institutions of the SDSS-III Collaboration including the University of Arizona, the Brazilian Participation Group, Brookhaven National Laboratory, Carnegie Mellon University, University of Florida, the French Participation Group, the German Participation Group, Harvard University, the Instituto de Astrofisica de Canarias, the Michigan State/Notre Dame/JINA Participation Group, Johns Hopkins University, Lawrence Berkeley National Laboratory, Max Planck Institute for Astrophysics, Max Planck Institute for Extraterrestrial Physics, New Mexico State University, New York University, Ohio State University, Pennsylvania State University, University of Portsmouth, Princeton University, the Spanish Participation Group, University of Tokyo, University of Utah, Vanderbilt University, University of Virginia, University of Washington, and Yale University.

5.5 Appendix to Chapter 3: Asynchronous EBs with $P_{orb} < 10$ Days

Table 5.1. Asynchronous Short Period Systems

Kepler ID
KEBC Orbital Period Corrected
1161345 ($P_{orb} = 2P_{KEBC}$)
2558370 ($P_{orb} = 2P_{KEBC}$)
4454219 ($P_{orb} = 2P_{KEBC}$)
4912991 ($P_{orb} = 0.5P_{KEBC}$)
8409588 ($P_{orb} = 2P_{KEBC}$)
9084778 ($P_{orb} = 2P_{KEBC}$)
9592575 ($P_{orb} = 2P_{KEBC}$)
9597411 ($P_{orb} = 2P_{KEBC}$)
10614158 ($P_{orb} = 2P_{KEBC}$)
10848459 ($P_{orb} = 2P_{KEBC}$)
11303811 ($P_{orb} = 0.5P_{KEBC}$)
Possible false positives
4929299
5642620
6370120
7051984
8176653
9478836
9642018
10338279 (SB2 in Kolbl et al. 2015)
10407221
10857519 (SB2 in Kolbl et al. 2015)

Table 5.1 (cont'd)

Kepler ID
12170648
12255382
Possible planets or brown dwarfs
3970233
5369827
7269493
7376983
7763269 (SB2 in Kolbl et al. 2015)
9752973 (SB2 in Kolbl et al. 2015)
9880467
9895004
10395543
10925104
Asynchronous short period EBs
2445975
3443790
3459199
3848972
4367544
4456622
4946584
5372966
5648449

Table 5.1 (cont'd)

Kepler ID
6956014
7684873
7838906
8906676
8938628
9266285
9579499
10613718
11147460
11231334
11548140
11560037
Pseudosynchronized EBs
5024292
5025294
7376500
9971475
10287248
10923260
12470530

BIBLIOGRAPHY

Abadi, M. G., Navarro, J. F., Steinmetz, M., & Eke, V. R. 2003, ApJ, 591, 499

Abt, H. A., & Boonyarak, C. 2004, ApJ, 616, 562

Aihara, H., Allende Prieto, C., An, D., et al. 2011, ApJS, 193, 29

Angus, R., Aigrain, S., Foreman-Mackey, D., & McQuillan, A. 2015, MNRAS, 450, 1787

Arnett, D. 1996, Supernovae and Nucleosynthesis: An Investigation of the History of Matter from the Big Bang to the Present (Princeton University Press)

Astropy Collaboration, Robitaille, T. P., Tollerud, E. J., et al. 2013, A&A, 558, A33

Babcock, H. W. 1961, ApJ, 133, 572

Bahcall, J. N., Hut, P., & Tremaine, S. 1985, ApJ, 290, 15

Bailer-Jones, C. A. L. 2009, in IAU Symposium, Vol. 254, The Galaxy Disk in Cosmological Context, ed. J. Andersen, Nordströara, B. m, & J. Bland-Hawthorn, 475–482

Barnes, J. W. 2007a, PASP, 119, 986

Barnes, R., Meadows, V. S., & Evans, N. 2015, ApJ, 814, 91

Barnes, S. A. 2003, ApJ, 586, 464

—. 2007b, ApJ, 669, 1167

Beck, J. G. 2000, Sol. Phys., 191, 47

Belokurov, V., Zucker, D. B., Evans, N. W., et al. 2006, ApJ, 642, L137

Bernard, E. J., Ferguson, A. M. N., Schlafly, E. F., et al. 2016, ArXiv e-prints, arXiv:1607.06088

Binney, J. 1978, MNRAS, 183, 779

Binney, J., & Merrifield, M. 1998, Galactic Astronomy

Borucki, W. J., & Summers, A. L. 1984, Icarus, 58, 121

Bovy, J., Rix, H.-W., & Hogg, D. W. 2012, ApJ, 751, 131

Bressan, A., Marigo, P., Girardi, L., et al. 2012, MNRAS, 427, 127

Briechle, K., & Hanebeck, U. D. 2001, Proc. SPIE, 4387, 95

Brook, C. B., Kawata, D., Gibson, B. K., & Freeman, K. C. 2004, ApJ, 612, 894

Brown, T. M., Latham, D. W., Everett, M. E., & Esquerdo, G. A. 2011, AJ, 142, 112

Browning, M. K. 2008, ApJ, 676, 1262

Browning, M. K., Basri, G., Marcy, G. W., West, A. A., & Zhang, J. 2010, AJ, 139, 504

Bryson, S. T., Tenenbaum, P., Jenkins, J. M., et al. 2010, ApJ, 713, L97

Bryson, S. T., Abdul-Masih, M., Batalha, N., et al. 2015, KSCI-19093-002

Burkart, J., Quataert, E., & Arras, P. 2014, MNRAS, 443, 2957

Burke, B. F. 1957, AJ, 62, 90

Carlin, J. L., DeLaunay, J., Newberg, H. J., et al. 2013, ApJ, 777, L5

Chabrier, G. 2003, PASP, 115, 763

Chabrier, G., & Baraffe, I. 1997, A&A, 327, 1039

Chambers, K. C., Magnier, E. A., Metcalfe, N., et al. 2016, ArXiv e-prints, arXiv:1612.05560

Chandrasekhar, S. 1942, Principles of stellar dynamics

Chen, X., de Grijs, R., & Deng, L. 2016, ApJ, 832, 138

Christiansen, J. L., Jenkins, J. M., Caldwell, D. A., et al. 2013, Kepler Data Characteristics Handbook (KSCI-19040-004)

Claret, A., Gimenez, A., & Cunha, N. C. S. 1995, A&A, 299, 724

Collier Cameron, A. 2007, Astronomische Nachrichten, 328, 1030

Contadakis, M. E. 1995, A&A, 300, 819

Covey, K. R., Ivezić, Ž., Schlegel, D., et al. 2007, AJ, 134, 2398

Cutri, R. M., Skrutskie, M. F., van Dyk, S., et al. 2003, VizieR Online Data Catalog, 2246, 0

Dahn, C. C., Harrington, R. S., Riepe, B. Y., et al. 1976, Publications of the U.S. Naval Observatory Second Series, 24, 1

Darwin, G. H. 1879, Philosophical Transactions of the Royal Society of London Series I, 170, 447

Davenport, J. R. A. 2016, ApJ, 829, 23

Davenport, J. R. A., Hebb, L., & Hawley, S. L. 2015, ApJ, 806, 212

Davenport, J. R. A., Hawley, S. L., Hebb, L., et al. 2014, ApJ, 797, 122

Delfosse, X., Forveille, T., Perrier, C., & Mayor, M. 1998, A&A, 331, 581

Dieterich, S. B., Henry, T. J., Golimowski, D. A., Krist, J. E., & Tanner, A. M. 2012, AJ, 144, 64

Djorgovski, S., & Sosin, C. 1989, ApJ, 341, L13

Dobler, W., Stix, M., & Brandenburg, A. 2006, ApJ, 638, 336

Donahue, R. A. 1998, in Astronomical Society of the Pacific Conference Series, Vol. 154, Cool Stars, Stellar Systems, and the Sun, ed. R. A. Donahue & J. A. Bookbinder, 1235

Duchêne, G., & Kraus, A. 2013, ARA&A, 51, 269

Duquennoy, A., & Mayor, M. 1991, A&A, 248, 485

Eggen, O. J. 1967, MmRAS, 70, 111

Eggen, O. J., Lynden-Bell, D., & Sandage, A. R. 1962, ApJ, 136, 748

Eggleton, P. 2006, Evolutionary Processes in Binary and Multiple Stars (Cambridge University Press)

Fanelli, M. N., Jenkins, J. M., Bryson, S. T., et al. 2011, Kepler Data Processing Handbook (KSCI-19081-001)

Fouchard, M., Froeschlé, C., Valsecchi, G., & Rickman, H. 2006, Celestial Mechanics and Dynamical Astronomy, 95, 299

Gies, D. R., & Helsel, J. W. 2005, ApJ, 626, 844

Gilliland, R. L., Chaplin, W. J., Jenkins, J. M., Ramsey, L. W., & Smith, J. C. 2015, AJ, 150, 133

Gilmore, G., & Reid, N. 1983, MNRAS, 202, 1025

Giovanelli, R. G. 1946, Nature, 158, 81

Giuricin, G., Mardirossian, F., & Mezzetti, M. 1984a, A&A, 135, 393

—. 1984b, A&A, 141, 227

Gizis, J. E., Burgasser, A. J., Berger, E., et al. 2013, ApJ, 779, 172

Gómez, F. A., White, S. D. M., Marinacci, F., et al. 2015, ArXiv e-prints, arXiv:1509.08459

Goswami, J. N., McGuire, R. E., Reedy, R. C., Lal, D., & Jha, R. 1988, J. Geophys. Res., 93, 7195

Güdel, M. 2004, A&A Rev., 12, 71

Harrington, R. S. 1990, AJ, 100, 559

Harrison, T. E., Coughlin, J. L., Ule, N. M., & López-Morales, M. 2012, AJ, 143, 4

Hawley, S. L., Angus, R., Buzasi, D., et al. 2016, ArXiv e-prints, arXiv:1607.04302

Hawley, S. L., Davenport, J. R. A., Kowalski, A. F., et al. 2014, ApJ, 797, 121

Hawley, S. L., Gizis, J. E., & Reid, I. N. 1996, AJ, 112, 2799

Hawley, S. L., & Pettersen, B. R. 1991, ApJ, 378, 725

Helmi, A., & de Zeeuw, P. T. 2000, MNRAS, 319, 657

Henry, T. J., Franz, O. G., Wasserman, L. H., et al. 1999, ApJ, 512, 864

Hilditch, R. W. 2001, An Introduction to Close Binary Stars (Cambridge University Press)

Hilton, E. J. 2011, PhD thesis, University of Washington

Hosey, A. D., Henry, T. J., Jao, W.-C., et al. 2015, AJ, 150, 6

Hunt-Walker, N. M., Hilton, E. J., Kowalski, A. F., Hawley, S. L., & Matthews, J. M. 2012, PASP, 124, 545

Hunter, J. D. 2007, Computing In Science & Engineering, 9, 90

Hut, P. 1980, A&A, 92, 167

—. 1981, A&A, 99, 126

Ibata, R. A., Gilmore, G., & Irwin, M. J. 1994, Nature, 370, 194

Ivezić, Ž., Beers, T. C., & Jurić, M. 2012, ARA&A, 50, 251

Ivezić, Ž., Sesar, B., Jurić, M., et al. 2008, ApJ, 684, 287

Jiang, Y.-F., & Tremaine, S. 2010, MNRAS, 401, 977

Jones, E., Oliphant, T., Peterson, P., et al. 2001–, SciPy: Open source scientific tools for Python, [Online; accessed ¡today¿]

Juric, M. 2012, LSD: Large Survey Database framework, Astrophysics Source Code Library, ascl:1209.003

Juric, M., Cosic, K., Vinkovic, D., & Ivezic, Z. 2010, in Bulletin of the American Astronomical Society, Vol. 42, American Astronomical Society Meeting Abstracts #215, 222

Jurić, M., Ivezić, Ž., Brooks, A., et al. 2008, ApJ, 673, 864

Kazantzidis, S., Bullock, J. S., Zentner, A. R., Kravtsov, A. V., & Moustakas, L. A. 2008, ApJ, 688, 254

Kelly, B. C. 2007, ApJ, 665, 1489

Kerr, F. J., Hindman, J. V., & Carpenter, M. S. 1957, Nature, 180, 677

Khaliullin, K. F., & Khaliullina, A. I. 2010, MNRAS, 401, 257

Kippenhahn, R., & Weigert, A. 1967, ZAp, 65, 251

Kirk, B., Conroy, K., Prša, A., et al. 2016, AJ, 151, 68

Kjurkchieva, D., & Vasileva, D. 2018, New A, 58, 10

Kjurkchieva, D., Vasileva, D., & Dimitrov, D. 2016, AJ, 152, 189

Koch, R. H., & Hrivnak, B. J. 1981, AJ, 86, 438

Kolbl, R., Marcy, G. W., Isaacson, H., & Howard, A. W. 2015, AJ, 149, 18

Kopal, Z. 1955, Annales d'Astrophysique, 18, 379

Kroupa, P. 2001, MNRAS, 322, 231

Küker, M., & Rüdiger, G. 2011, Astronomische Nachrichten, 332, 933

Kumar, P., Ao, C. O., & Quataert, E. J. 1995, ApJ, 449, 294

Lacy, C. H., Moffett, T. J., & Evans, D. S. 1976, ApJS, 30, 85

Langer, N. 2012, ARA&A, 50, 107

Latham, D. W., Stefanik, R. P., Torres, G., et al. 2002, AJ, 124, 1144

Lee, Y. S., Beers, T. C., An, D., et al. 2011, ApJ, 738, 187

Leighton, R. B. 1969, ApJ, 156, 1

Levato, H. 1974, A&A, 35, 259

Li, C., & Lee, C. 1993, Pattern Recognition, 26, 617

Li, C., & Tam, P. 1998, Pattern Recognition Letters, 19, 771

Li, J., Newberg, H. J., Carlin, J. L., et al. 2012, ApJ, 757, 151

Lomb, N. R. 1976, Ap&SS, 39, 447

Maehara, H., Shibayama, T., Notsu, S., et al. 2012, Nature, 485, 478

Magnier, E. 2006, in The Advanced Maui Optical and Space Surveillance Technologies Conference, E50

Magnier, E. A., Schlafly, E., Finkbeiner, D., et al. 2013, ApJS, 205, 20

Majewski, S. R., Ostheimer, J. C., Rocha-Pinto, H. J., et al. 2004, ApJ, 615, 738

Majewski, S. R., Skrutskie, M. F., Weinberg, M. D., & Ostheimer, J. C. 2003, ApJ, 599, 1082

Marilli, E., Frasca, A., Covino, E., et al. 2007, A&A, 463, 1081

Martin, N. F., Ibata, R. A., Bellazzini, M., et al. 2004, MNRAS, 348, 12

Mason, J., Hughes, D. W., & Tobias, S. M. 2002, ApJ, 580, L89

Mazeh, T. 2008, in EAS Publications Series, Vol. 29, EAS Publications Series, ed. M.-J. Goupil & J.-P. Zahn, 1–65

McKinney, W. 2010, in Proceedings of the 9th Python in Science Conference, ed. S. van der Walt & J. Millman, 51 – 56

McQuillan, A., Aigrain, S., & Mazeh, T. 2013, MNRAS, 432, 1203

McQuillan, A., Mazeh, T., & Aigrain, S. 2014, ApJS, 211, 24

Meibom, S., & Mathieu, R. D. 2005, ApJ, 620, 970

Meibom, S., Mathieu, R. D., & Stassun, K. G. 2006, ApJ, 653, 621

Meibom, S., Barnes, S. A., Latham, D. W., et al. 2011, ApJ, 733, L9

Mohanty, S., & Basri, G. 2003, ApJ, 583, 451

Momany, Y., Zaggia, S. R., Bonifacio, P., et al. 2004, A&A, 421, L29

Morbidelli, A. 2005, ArXiv Astrophysics e-prints, astro-ph/0512256

Morganson, E., Conn, B., Rix, H.-W., et al. 2016, ArXiv e-prints, arXiv:1604.07501

Morin, J., Donati, J.-F., Petit, P., et al. 2010, MNRAS, 407, 2269

Morris, B. M., Hebb, L., Davenport, J. R. A., Rohn, G., & Hawley, S. L. 2017, ApJ, 846, 99

Newberg, H. J., Yanny, B., Rockosi, C., et al. 2002, ApJ, 569, 245

Nielsen, M. B., Gizon, L., Schunker, H., & Karoff, C. 2013, A&A, 557, L10

Norris, J. 1987, ApJ, 314, L39

Ogilvie, G. I. 2014, ARA&A, 52, 171

Osaki, Y. 1996, PASP, 108, 39

Padmanabhan, N., Schlegel, D. J., Finkbeiner, D. P., et al. 2008, ApJ, 674, 1217

Parks, J. R., White, R. J., Baron, F., et al. 2015, ArXiv e-prints, arXiv:1508.04755

Peñarrubia, J., Martínez-Delgado, D., Rix, H. W., et al. 2005, ApJ, 626, 128

Penzias, A. A., & Wilson, R. W. 1965, ApJ, 142, 419

Postnov, K. A., & Yungelson, L. R. 2014, Living Reviews in Relativity, 17, 3

Prialnik, D. 2000, An Introduction to the Theory of Stellar Structure and Evolution (Cambridge University Press)

Prša, A., Batalha, N., Slawson, R. W., et al. 2011, AJ, 141, 83

Prez, F., & Granger, B. E. 2007, Computing in Science & Engineering, 9, 21

Quinn, P. J., Hernquist, L., & Fullagar, D. P. 1993, ApJ, 403, 74

Raghavan, D., McAlister, H. A., Henry, T. J., et al. 2010, ApJS, 190, 1

Rappaport, S., Swift, J., Levine, A., et al. 2014, ApJ, 788, 114

Reid, I. N., Cruz, K. L., Allen, P., et al. 2004, AJ, 128, 463

Reinhold, T., & Gizon, L. 2015, A&A, 583, A65

Reinhold, T., Reiners, A., & Basri, G. 2013, A&A, 560, A4

Rocha-Pinto, H. J., Majewski, S. R., Skrutskie, M. F., Crane, J. D., & Patterson, R. J. 2004, ApJ, 615, 732

Rubenstein, E. P. 2001, AJ, 121, 3219

Rubin, V. C., & Ford, Jr., W. K. 1970, ApJ, 159, 379

Rucinski, S. M. 1994, PASP, 106, 462

Salpeter, E. E. 1955, ApJ, 121, 161

Scargle, J. D. 1982, ApJ, 263, 835

Schaefer, B. E., King, J. R., & Deliyannis, C. P. 2000, ApJ, 529, 1026

Schatzman, E. 1962, Annales d'Astrophysique, 25, 18

Schlafly, E. F., & Finkbeiner, D. P. 2011, ApJ, 737, 103

Schlafly, E. F., Finkbeiner, D. P., Jurić, M., et al. 2012, ApJ, 756, 158

Schlegel, D. J., Finkbeiner, D. P., & Davis, M. 1998, ApJ, 500, 525

Schönrich, R., & Binney, J. 2009, MNRAS, 396, 203

Schrijver, C. J., Beer, J., Baltensperger, U., et al. 2012, Journal of Geophysical Research (Space Physics), 117, 8103

Searle, L., & Zinn, R. 1978, ApJ, 225, 357

Segura, A., Walkowicz, L. M., Meadows, V., Kasting, J., & Hawley, S. 2010, Astrobiology, 10, 751

Sellwood, J. A., Nelson, R. W., & Tremaine, S. 1998, ApJ, 506, 590

Sezgin, M., & Sankur, B. 2004, Journal of Electronic Imaging, 13, 146

Sick, J. 2015, padova: Version 0.1.2, doi:10.5281/zenodo.16869

Silva, A. V. R. 2003, ApJ, 585, L147

Skumanich, A. 1972, ApJ, 171, 565

Skumanich, A., Smythe, C., & Frazier, E. N. 1975, ApJ, 200, 747

Slater, C. T., Bell, E. F., Schlafly, E. F., et al. 2014, ApJ, 791, 9

Slawson, R. W., Prša, A., Welsh, W. F., et al. 2011, AJ, 142, 160

Smith, J. C., Stumpe, M. C., Van Cleve, J. E., et al. 2012, PASP, 124, 1000

Spiegel, E. A., & Zahn, J.-P. 1992, A&A, 265, 106

Steigman, G. 2007, Annual Review of Nuclear and Particle Science, 57, 463

Still, M., & Barclay, T. 2012, PyKE: Reduction and analysis of Kepler Simple Aperture Photometry data, astrophysics Source Code Library, ascl:1208.004

Strassmeier, K. G. 2002, Astronomische Nachrichten, 323, 309

Tassoul, J.-L. 2000, Stellar Rotation (Cambridge University Press)

Thompson, S. E., Fraquelli, D., van Cleve, J., & Caldwell, D. 2016, Kepler Archive Manual KDMC-10008-006

Thompson, S. E., & Fraquelli, D. A. 2014, Kepler Archive Manual (KDMC-10008-005)

Thompson, S. E., Everett, M., Mullally, F., et al. 2012, ApJ, 753, 86

Tilley, M. A., Segura, A., Meadows, V. S., Hawley, S., & Davenport, J. 2017, ArXiv e-prints, arXiv:1711.08484

Tobias, S. M. 2002, Philosophical Transactions of the Royal Society of London Series A, 360, 2741

Tonry, J. L., Stubbs, C. W., Lykke, K. R., et al. 2012, ApJ, 750, 99

Toth, G., & Ostriker, J. P. 1992, ApJ, 389, 5

van Altena, W. F., Lee, J. T., & Hoffleit, D. 1995, VizieR Online Data Catalog, 1174, 0

Van Cleve, J., Caldwell, D., Thompson, R., et al. 2009, Kepler Instrument Handbook (KSCI-19033-001)

van der Walt, S., Colbert, S. C., & Varoquaux, G. 2011, Computing in Science & Engineering, 13, 22

van der Walt, S., Schnberger, J. L., Nunez-Iglesias, J., et al. 2014, PeerJ, 453, doi:https://doi.org/10.7717/peerj.453

Van Eylen, V., Winn, J. N., & Albrecht, S. 2016, ArXiv e-prints, arXiv:1603.08224

van Saders, J. L., Ceillier, T., Metcalfe, T. S., et al. 2016, Nature, 529, 181

VanderPlas, J. 2016, gatspy: General tools for Astronomical Time Series in Python, Astrophysics Source Code Library, ascl:1610.007

VanderPlas, J. T., & Ivezić, Ž. 2015, ApJ, 812, 18

Vogt, S. S., & Penrod, G. D. 1983, PASP, 95, 565

Walkowicz, L. M., & Basri, G. S. 2013, MNRAS, 436, 1883

Walkowicz, L. M., Hawley, S. L., & West, A. A. 2004, PASP, 116, 1105

Warner, B. 2003, Cataclysmic Variable Stars (Cambridge University Press), 592, doi:10.1017/CBO9780511586491

West, A. A., Morgan, D. P., Bochanski, J. J., et al. 2011, AJ, 141, 97

Westerhout, G. 1957, Bull. Astron. Inst. Netherlands, 13, 201

White, S. D. M., & Rees, M. J. 1978, MNRAS, 183, 341

Widrow, L. M., Barber, J., Chequers, M. H., & Cheng, E. 2014, MNRAS, 440, 1971

Widrow, L. M., Gardner, S., Yanny, B., Dodelson, S., & Chen, H.-Y. 2012, ApJ, 750, L41

Williams, M. E. K., Steinmetz, M., Binney, J., et al. 2013, MNRAS, 436, 101

Wilson, O. C. 1963, ApJ, 138, 832

Witte, M. G., & Savonije, G. J. 2002, A&A, 386, 222

Wyse, R. F. G., Gilmore, G., Norris, J. E., et al. 2006, ApJ, 639, L13

Xu, Y., Newberg, H. J., Carlin, J. L., et al. 2015, ArXiv e-prints, arXiv:1503.00257

Yamada, M., Kulsrud, R., & Ji, H. 2010, Reviews of Modern Physics, 82, 603

Yanny, B., & Gardner, S. 2013, ApJ, 777, 91

Yanny, B., Newberg, H. J., Grebel, E. K., et al. 2003, ApJ, 588, 824

Yanny, B., Rockosi, C., Newberg, H. J., et al. 2009, AJ, 137, 4377

Yoachim, P., & Dalcanton, J. J. 2006, AJ, 131, 226

York, D. G., Adelman, J., Anderson, Jr., J. E., et al. 2000, AJ, 120, 1579

Zahn, J.-P. 1977, A&A, 57, 383

Zahn, J.-P. 2013, in Lecture Notes in Physics, Berlin Springer Verlag, Vol. 861, Lecture Notes in Physics, Berlin Springer Verlag, ed. J. Souchay, S. Mathis, & T. Tokieda, 301

Zahn, J.-P., & Bouchet, L. 1989, A&A, 223, 112